Density Dependence of the $\nu = 5/2$ Fractional Quantum Hall Effect

—

Compressibility of a Two-dimensional Electron System under Microwave Irradiation

Dissertation
der Mathematisch-Naturwissenschaftlichen Fakultät
der Eberhard Karls Universität Tübingen
zur Erlangung des Grades eines
Doktors der Naturwissenschaften
(Dr. rer. nat.)

vorgelegt von
Johannes Nübler
aus Freiburg im Breisgau

Tübingen
2011

Tag der mündlichen Qualifikation	28.10.2011
Dekan	Prof. Dr. Wolfgang Rosenstiel
1. Berichterstatter	Prof. Dr. David Wharam
2. Berichterstatter	Prof. Dr. Klaus von Klitzing
3. Berichterstatter	Prof. Dr. Amir Yacoby

Abstract

The electronic properties of solids are a rich field of research. It has proven especially interesting to restrict the motion of electrons to only two dimensions and to investigate their properties at low temperatures in perpendicular magnetic fields. Here, we consider two effects that are both characterized by vanishingly small longitudinal resistance, namely the fractional quantum Hall effect and microwave induced resistance oscillations.

The **fractional quantum Hall effect at filling factor 5/2** came as a surprise at its discovery in 1987, because quantization had only been observed at filling factors with odd denominators. These can be understood as the integer quantum Hall effect of a new kind of particles, the so called composite fermions. The 5/2 state, however, did not fit into this scheme. Several explanations were proposed, among them a mechanism where composite fermions pair up in a Cooper-pair like way, which results in the formation of an energy gap. This implied that the elementary excitations of the 5/2 state might obey non-Abelian statistics. Hence, the state of the system could be altered by taking one particle in a loop around another one, thereby enabling topological quantum computation. Experimental proof of this property, however, remains elusive.

The 5/2 state is only observed in today's cleanest heterostructures. Here we use such a structure with the additional possibility to change the electron density during measurement in a wide range. We investigate the density dependence of the energy gap of the 5/2 state and compare the results with theoretical predictions. In order to gain insight into the mechanisms that limit the pronouncedness of the 5/2 state in current state-of-the-art samples we discuss the influence of different kinds of disorder. Also the surprisingly large size of the quasiparticles plays a role in this context.

The second part of the thesis is devoted to the **properties of two-dimensional electron systems under microwave irradiation**. Here, the longitudinal resistance shows oscillations that are periodic in the inverse magnetic field. In very clean samples these can drop all the way down to zero. Yet, in contrast to the quantum Hall effect, the Hall resistance is not affected by the microwave irradiation and does not show plateaus. Furthermore, the magnetic field values where the microwave induced resistance oscillations occur are independent of the electron density. Rather, the quantity of relevance is the ratio of the microwave and cyclotron frequencies. The underlying mechanism is not fully understood.

Here, we investigate the compressibility under microwave irradiation. This

quantity describes how the chemical potential responds to changes in the electron denstiy. As a thermodynamic quantity it complements electric transport measurements. It can be measured locally with the help of a single electron transistor deposited on the sample surface. In order to use this technique for our purpose the heterostructure that hosts the two-dimensional electron system must meet certain requirements: it has to be possible to change the electron density in a controlled way, the single electron transistor must be operable, and finally transport measurements should show pronounced microwave induced resistance oscillations - a combination that turned out to be challenging. We could successfully show that compressibility measurements are possible also in the presence of microwave irradiation. The compressibility shows, as was predicted theoretically, oscillations that resemble those of the longitudinal resistance. The results can help to clarify the mechanism behind microwave induced resistance oscillations.

Kurzbeschreibung

Die Untersuchung der elektronischen Eigenschaften von Festkörpern ist ein reichhaltiges Forschungsgebiet. Als besonders interessant hat es sich herausgestellt, die Bewegung der Elektronen auf eine zweidimensionale Ebene einzuschränken, und ihre Eigenschaften bei tiefen Temperaturen und in einem senkrecht angelegten Magnetfeld zu untersuchen. Wir befassen uns hier mit zwei Effekten, deren Charakteristikum ein verschwindend kleiner Längswiderstand ist. Es handelt sich um den gebrochenzahligen Quanten-Hall-Effekt sowie um mikrowelleninduzierte Widerstandsoszillationen.

Der **gebrochenzahlige Quanten-Hall-Effekt bei Füllfaktor 5/2** war bei seiner Entdeckung 1987 eine Überraschung, da zuvor Quantisierung nur bei Füllfaktoren mit ungeradzahligem Nenner beobachtet worden war. Diese können als der gewöhnliche Quanten-Hall-Effekt von neuen Teilchen, den composite fermions (zusammengesetzte Fermionen), erklärt werden. Der 5/2-Zustand passte jedoch nicht in dieses Muster. Daraufhin wurden verschiedene Erklärungen vorgeschlagen, insbesondere ein Mechanismus, bei dem sich zwei composite fermions ähnlich wie bei Cooper-Paarbildung zusammentun, was zur Bildung einer Energielücke führt. Dies implizierte eine weitere neuartige Vorhersage: Die elementaren Anregungen des 5/2-Zustandes könnten nichtabelscher Statistik gehorchen. Hierbei kann der Zustand des Systems verändert werden, indem z. B. ein Teilchen um ein anderes herumgeführt wird. Diese nichtabelsche Statistik könnte einen sogenannten topologischen Quantencomputer möglich machen. Experimentell ist die Vorhersage jedoch noch nicht bestätigt.

Der 5/2-Zustand wird nur in den reinsten heute verfügbaren Proben beobachtet. In der vorliegenden Arbeit benutzen wir eine solche Probe, bei der die Elektronendichte während der Messung über einen weiten Bereich verändert werden kann. Wir untersuchen die Dichteabhängigkeit der Energielücke des 5/2-Zustandes und vergleichen diese mit theoretischen Vorhersagen. Um zu beleuchten, welche Prozesse die Qualität des 5/2-Zustandes begrenzen, diskutieren wir den Einfluss verschiedener Arten von Unordnung. Auch die überraschend große Ausdehnung der Quasiteilchen spielt hier eine Rolle.

Der zweite Teil der Dissertation befasst sich mit den **Eigenschaften von zweidimensionalen Elektronensystemen unter Mikrowellenstrahlung**. Die Magnetfeldabhängigkeit des Längswiderstandes zeigt hier 1/B-periodische mikrowelleninduzierte Oszillationen. In extrem reinen Proben können diese bis auf Null abfallen. Im Vergleich zum Quanten-Hall-Effekt wird jedoch der Hall-Widerstand von der Mikrowellenstrahlung nicht beeinflusst und zeigt keine Plateaus. Außerdem treten die mikrowelleninduzierten Widerstandsoszillationen

bei Magnetfeldwerten auf, die unabhängig von der Elektronendichte sind. Die charakteristische Größe ist vielmehr das Verhältnis von Mikrowellenfrequenz und Zyklotronfrequenz. Der zugrundeliegende Mechanismus ist noch nicht abschließend geklärt.

In dieser Arbeit untersuchen wir die Kompressibilität unter Mikrowelleneinstrahlung. Diese Größe beschreibt, wie das chemische Potential auf Änderungen der Elektronendichte reagiert. Als eine thermodynamische Größe ergänzt sie elektrische Transportmessungen. Sie kann lokal mit einem auf die Probenoberfläche aufgebrachten Einzelelektronentransistor gemessen werden. Um diese Technik für unsere Zwecke zu verwenden, muss die Heterostruktur, in die das zweidimensionale Elektronensystem eingebettet ist, verschiedene Anforderungen erfüllen: die Elektronendichte muss kontrolliert verändert werden können, die Einzelelektronentransistoren müssen verwendbar sein, und schließlich sollten Transportmessungen ausgeprägte mikrowelleninduzierte Oszillationen zeigen, - eine Kombination, die nicht einfach zu erfüllen war. Wir konnten erfolgreich zeigen, dass Kompressibilitätsmessungen unter Mikrowelleneinstrahlung möglich sind. Die Kompressibilität zeigt, wie theoretisch vorhergesagt, Oszillationen, die denen des Längswiderstandes ähnlich sind. Die Ergebnisse können bei der Identifikation des zugrundeliegenden Mechanismus hilfreich sein.

Contents

Nomenclature

$\mathbf{j}$, j_x, j_y	electrical current density, its components
Δ_ν	energy gap at filling factor ν
Γ	(Landau) level broadening
μ	electron mobility
μ^{ch}	chemical potential
ν	filling factor
$\omega = 2\pi f$	angular frequency
$\omega_c = \frac{eB}{m^*}$	cyclotron frequency
$\omega_p = 2\pi f_p$	plasmon frequency
$\omega_{mp} = 2\pi f_{mp}$	magnetoplasmon frequency
ϕ	phase angle
ρ	electrical resistivity (tensor)
σ	electrical conductivity (tensor)
τ	transport, or momentum relaxation scattering time
τ_q	quantum, or single particle lifetime
φ	electrostatic potential
e	elementary charge

$E_c = \hbar\omega_c$	cyclotron energy
E_F	Fermi energy
E_q	Coulomb energy
E_z	Zeemann energy
g^*	Lande factor, including all material and interaction effects
$h = 2\pi\hbar$	Planck constant
j	Landau level index
$l_B = \sqrt{\hbar/eB}$	magnetic length
L_x, L_y	size of a 2D sample
m	Landau level degenerate quantum number
m^*	effective electron mass
n	2D-electron density
R_{xx}	longitudinal resistance
R_{xy}	transverse, or Hall resistance
2D	two-dimensional
2DES	two-dimensional electron system
AlGaAs	aluminium gallium arsenide
BG	backgate
BWO	backward wave oscillator
CBO	Coulomb blockade oscillations
DOS	density of states
FQHE	fractional quantum Hall effect
GaAs	gallium arsenide
IQHE	integer quantum Hall effect
LL	Landau level

MBE	molecular beam epitaxy
MICRO	microwave induced compressibility oscillations
MIRO	microwave induced resistance oscillations
QP, QH	quasiparticle, quasihole
QW	quantum well
SdH	Shubnikov-de-Haas (oscillations)
SET	single electron transistor

Chapter 1

Introduction

The idea of confining electrons to a two-dimensional plane was extremely fruitful. Two Nobel prizes have been issued in this field: One in 1985 to Klaus von Klitzing "for the discovery of the quantized Hall effect" which is today referred to as the integer quantum Hall effect (IQHE). It was first observed in 1980 when von Klitzing investigated the behavior of electrons confined to a plane and subjected to a magnetic field at low temperatures [1]. Surprisingly, the Hall resistance, which in the classical case is proportional to the magnetic field, showed plateaus. The resistance values in these plateaus were independent of the details of the measurement conditions and can be expressed by fundamental constants of nature:

$$R_{xy} = \frac{h}{i\ e^2} \tag{1.1}$$

with $i = 1, 2, 3, \ldots$ an integer value, h the Planck constant and e the elementary charge. The plateaus are accompanied by vanishing longitudinal resistance R_{xx}. The IQHE is governed by the filling factor ν which is the ratio of the sample's electron density and the density of magnetic flux quanta piercing through it.

The second Nobel prize was awarded in 1998 to Robert B. Laughlin, Horst L. Stormer and Daniel C. Tsui "for their discovery of a new form of quantum fluid with fractionally charged excitations". In 1982 they had observed the hallmarks of the quantum Hall effect, namely vanishing R_{xx} and plateaus in R_{xy}, at a fractional value $\nu = 1/3$ of the filling factor [2]. A theoretical explanation of this fractional quantum Hall effect (FQHE) was proposed in 1983 [3].

The only experimental difference between the discovery of the IQHE and the FQHE was the higher purity of the crystals hosting the two-dimensional electron systems and the lower measurement temperatures. Improving the experimental conditions and the material quality thus enabled *new physical effects* to occur − a trend that continues up to today.

In this thesis we investigate two effects that are observed only in today's

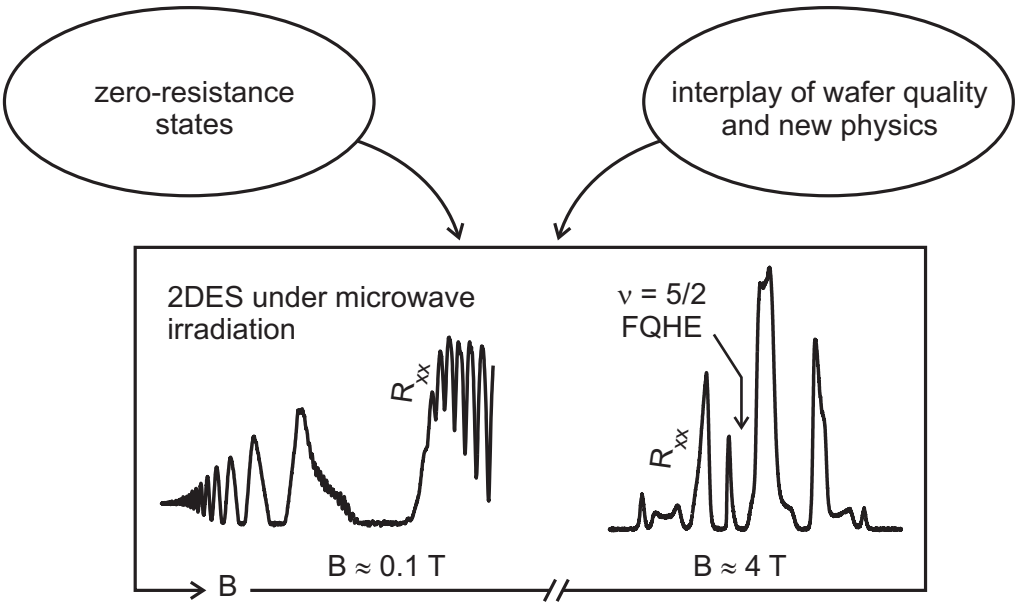

cleanest two-dimensional electron systems (2DES). Both exhibit vanishing longitudinal resistance, yet in very different magnetic field ranges and due to different physical reasons. The first effect is the FQHE at filling factor 5/2, the second is the behavior of the longitudinal resistance under microwave irradiation.

The **FQHE at filling factor 5/2** came as a surprise in 1987 [4, 5]. This is because all previously observed fractional quantum Hall states had filling factors with *odd* denominators. These can be understood as the integer quantum Hall effect of a new kind of particles named composite fermions [6]. The 5/2 state falls out of this scheme. Several explanations were proposed in the following, most importantly a pairing mechanism where two composite fermions join up in a Cooper pair like fashion. Together with this idea came the prediction that the elementary excitations of the 5/2 state may obey non-Abelian statistics: Taking one particle around another changes the state of the system by a unitary transformation. This could enable fault tolerant, so-called topological quantum computation. At present, however, this possibility is not yet experimentally verified.

The 5/2 FQHE state is extremely fragile and is observed only in today's cleanest samples. In this thesis we make use of a state-of-the-art sample with the additional ability to change the electron density over a large range during measurement. We investigate the density dependence of the energy gap associated with the 5/2 state and compare it to theoretical predictions. Concerning the interplay of wafer quality and physical effects we discuss the importance of different types of disorder for the 5/2 state. The, surprisingly large, size of the 5/2 quasiparticles plays an important role in this context.

The main part of this thesis is devoted to the **properties of 2D electron systems under microwave irradiation** at low temperatures and in weak magnetic fields. Under these conditions the longitudinal magnetoresistance shows microwave induced resistance oscillations (MIRO) periodic in the inverse magnetic field [7]. When a 2DES of extremely high purity is used, the minima of the oscillations drop all the way down to zero in finite magnetic field intervals [8,9]. In that respect MIRO is reminiscent of the QHE, yet the physics is very different: The Hall resistance is unaffected by the microwave irradiation and does not show plateaus. Also, the magnetic field position of the oscillations is, in contrast to the QHE, independent of the electron density. Rather, the effect is governed by the ratio of the microwave frequency ω and the cyclotron frequency $\omega_c = eB/m^*$ where e is the electron charge and m^* the effective mass of the host crystal. Resistance minima are observed when

$$\omega = (i + \phi_i)\omega_c, \tag{1.2}$$

with an integer value $i = 1, 2, 3, \ldots$ and a phase shift ϕ_i. The mechanism behind this effect is still under debate.

In this thesis we measure for the first time the compressibility of a 2DES under microwave irradiation. As a thermodynamic quantity it complements electrical transport measurements. The inverse compressibility $1/\chi$ is the change in chemical potential μ^{ch} induced by a change in the electron density n:

$$1/\chi = \frac{\partial \mu^{ch}}{\partial n}. \tag{1.3}$$

We measure $1/\chi$ locally with the help of a single electron transistor (SET) which is extremely sensitive to electrostatic potentials. Our measurement principle is to induce small changes in the 2DES's electron density that result in a change in its chemical potential according to equation 8.3. In order to adapt this known technique for our purposes several requirements for the used material hosting the 2DES have to be fulfilled: pronounced MIRO should be observed, changing the electron density must be possible and finally the SETs need to be operable. This turned out to be very challenging to fulfill.

To investigate the influence of microwave irradiation on the 2DES compressibility we necessarily also expose the SETs to this radiation, which strongly affects their properties. This makes a careful calibration necessary, but also gives access to local properties of the radiation field. We found it to be surprisingly inhomogeneous and strongly dependent on frequency, which needs to be taken into account for a proper interpretation of the compressibility measurements.

We find that the inverse compressibility shows microwave induced oscillations qualitatively similar to those observed in the longitudinal resistance. Even though their sign is reversed to what is expected from a first theoretical prediction [10], we could demonstrate the feasibility of compressibility measurements under microwave irradiation. The results may likely help in clarifying the physical mechanism of MIRO.

This thesis is organized in two parts: In **part I** we give theoretical foundations, in **part II** the experimental work is exposed and discussed. Each part is divided into three chapters. The first chapter of each part treats two-dimensional electron systems with a focus on material properties. The second chapter of each part is about the FQHE at filling factor 5/2 and the third chapter about the properties of 2DES under microwave irradiation. In more detail:

Chapter 2 introduces the 2DES, reviews conduction in a magnetic field and addresses several aspects of the heterostructure design important for highest purity wafers.

Chapter 3 gives the fundamentals of the integer and the fractional quantized Hall effect with special emphasis on the filling factor 5/2 state.

Chapter 4 is about the properties of the 2DES under microwave irradiation. Relevant experiments and current theoretical ideas are reviewed.

Chapter 5 opens the experimental part of this thesis. As material quality is an important issue for our experiments we critically review some of the common wisdom about what makes a sample a good sample. Especially the electron mobility, the most widely used quality indicator, turns out largely unrelated to the pronouncedness of the effects investigated here. We identify suitable wafers for our experiments and present their properties.

Chapter 6 is about the FQHE at filling factor 5/2. We use an excellent, density tunable heterostructure to measure the density dependence of the 5/2 energy gap. We give a detailed comparison to theory taking explicitly into account the wave function geometry in our specific sample and Landau level mixing effects. The size of the 5/2 quasiparticles turns out surprisingly large and may explain the discrepancy between theory and experiment.

Chapter 7 treats our compressibility measurements of a 2DES under MIRO conditions. Methods and necessary characterization measurements are

explained and illustrated. Two complications are encountered: The microwave radiation in the vicinity of the sample depends strongly on position and frequency. Furthermore, the compressibility in the absence of microwaves shows a somewhat unexpected, irregular behavior. Under these restrictions we then present successful measurements of the microwave influence on compressibility. We observe microwave induced compressibility oscillations that are periodic in the inverse magnetic field. The data are analyzed and compared to theory. Possible future experiments are discussed.

At various occasions we will introduce physical quantities in a double way. For example the cyclotron energy is:

$$\begin{aligned} E_c &= \hbar\omega_c \\ E_c^{\mathrm{GaAs}}[\mathrm{meV}] &= 1.73 \times B[\mathrm{T}] \end{aligned}$$

The second line is evaluated for our specific material (GaAs) and introduces units convenient for our measurements. We find this very useful to quickly estimate and compare energy scales, length scales and other relevant parameters.

Parts of the results presented in this thesis are already published:

- J. Nuebler, V. Umansky, R. Morf, M. Heiblum, K. von Klitzing and J. Smet: *Density dependence of the $\nu = 5/2$ energy gap: Experiment and theory*, PRB **81**, 035316 (2010).

Part I

Fundamentals

Chapter 2

Two-dimensional electron systems

The physical effects that are investigated in this thesis are observed when electrons are confined to a two-dimensional (2D) plane. These two-dimensional electron systems (2DES) need to be of exceptional quality, which means that scattering events must be rare. Furthermore, a magnetic field must be applied perpendicular to the plane. In this chapter we first review some basic facts about electrical conduction in magnetic fields. Then we turn to the relevant design parameters for excellent quality 2DES, and their experimental characteristics.

2.1 Introduction to 2D electron systems

As mentioned in the introduction, a key ingredient for the physical effects studied in this thesis is high purity of the crystal hosting the 2DES. Such crystals are today grown by molecular beam epitaxy (MBE) that has developed into a very sophisticated technology. Best qualities are obtained by trapping electrons in a thin layer of GaAs sandwiched in an AlGaAs crystal. The conduction band energy in GaAs is lower and thus a "quantum well" (QW) is formed (see Fig 2.1). The doping atoms are *not* located in the well itself in order to keep the region where electrons reside free of defects. Instead they are put in the AlGaAs at a spatial distance, an idea termed "modulation doping" [11, 12].

For the direction *perpendicular* to the 2D plane basic quantum mechanics predicts discrete energy levels in the QW. A well of width w with infinitely high walls selects wave vectors $k_i = \pi i/w$, with $i = 1, 2, 3, \ldots$. With $p_i = \hbar k_i$ the

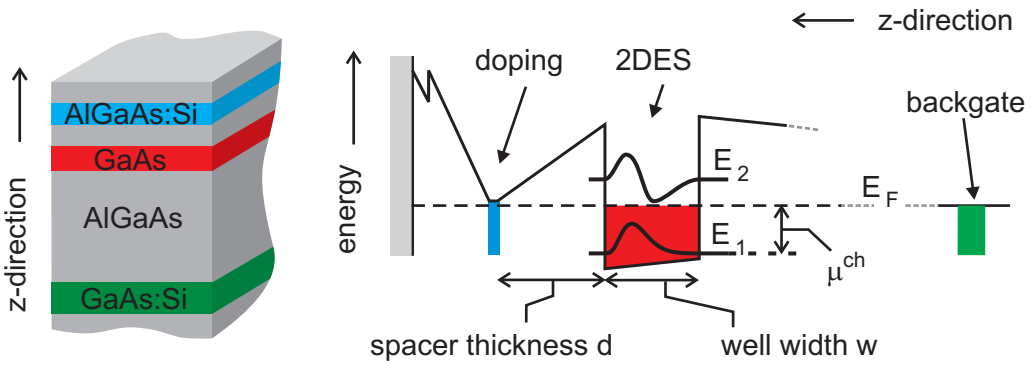

FIGURE 2.1: Left: side view on a typical single-side doped (blue) heterostructure hosting a 2DES (red) with a backgate (green). Right: Conduction band energy along the z-direction. Wavefunctions of the lowest two subbands in the quantum well are sketched. Here, only the lowest subband is occupied.

ith level has the energy $E_i = \frac{p_i^2}{2m^*} = \frac{(\hbar\pi i)^2}{2m^* w^2}$, which evaluates for GaAs to

$$E_i[\mathrm{eV}] = 5.16 \frac{i^2}{w[\mathrm{nm}]^2}. \tag{2.1}$$

If the Fermi energy is below the second level there is no freedom associated with the direction perpendicular to the 2D plane. The system is in that sense truly two-dimensional even though the wavefunction does have a finite width.

For the direction *within* the plane the k-vectors are quasi-continuous (unless the sample is further reduced in dimensionality, e.g. to a 1D quantum wire or a 0D quantum dot). In a single particle approximation and with the Pauli exclusion principle the Fermi energy for a 2DES with electron density n is (numbers are for GaAs, sp means single particle)

$$E_{\mathrm{F,sp}}^{\mathrm{2D}} = \frac{\pi\hbar^2}{m^*} n = \mu^{\mathrm{ch}} \tag{2.2}$$

$$E_{\mathrm{F,sp}}^{\mathrm{2D}}[\mathrm{meV}] = 3.58 \times n[10^{11}/\mathrm{cm}^2]. \tag{2.3}$$

We introduced also the chemical potential which at $T \approx 0$ is the same as the Fermi energy measured from the bottom of the conduction band (see Fig. 2.1).[1]

The number of states per area per unit energy, the density of states (DOS),

[1] We neglect all complications due to finite temperature. This is a valid assumption for typical electron densities in a QW at low temperatures: For $n = 2 \times 10^{11}/\mathrm{cm}^2$ one finds $E_\mathrm{F} \approx 7.2$ meV. This is approximately three orders of magnitude larger than $k_B T$ at 100 mK.

is independent of energy (numbers are for GaAs, sp means single particle):

$$\mathrm{DOS}^{\mathrm{2D,sp}} = \frac{m^*}{\pi\hbar^2} = 2.80 \times 10^{13}/\mathrm{eVcm}^2. \tag{2.4}$$

Again in the single particle approximation the DOS is equal to the compressibility χ which is defined from

$$1/\chi = \frac{\partial \mu^{\mathrm{ch}}}{\partial n}. \tag{2.5}$$

$1/\chi$ measures the change in chemical potential μ^{ch} induced by a change in electron density. Electron interaction effects can modify this result substantially: For certain electron densities the compressibility can become negative, which means that adding electrons will lower the Fermi energy. A large part of this thesis deals with measuring the local compressibility.

2.2 Electrical conduction in a magnetic field

Here we treat electrical properties in a purely classical manner. Quantum mechanical aspects leading to Landau level formation that make the classical Hall effect quantized will be treated in section 3.1. We neglect complications that arise when electrons as well as holes take part in conduction.

2.2.1 Conductivity and resistivity

The terms conductivity σ and resistivity ρ describe the same physical properties of a material, but correspond to two different measurement setups:

apply electric field,	measure current:	$\mathbf{j} = \sigma\mathbf{E}$
drive a current,	measure voltage drop:	$\mathbf{E} = \rho\mathbf{j}$

In most quantum Hall measurements we force a current through the sample (with the help of a known large resistor in series) and detect the voltage drop. σ and ρ are inverse to each other. If magnetic fields are applied, we have tensor quantities, making the inversion less obvious (see below).

2.2.2 Conductivity at B = 0

The classical Drude model of electrical conduction makes the following assumptions:

- an electric field **E** accelerates the electrons
- scattering randomizes the electron momentum $m\mathbf{v}$ at a rate τ
- all electrons take equally part in conduction.

This results in a drifting motion of average velocity

$$\mathbf{v} = \underbrace{\frac{e\tau}{m^*}}_{\mu} \mathbf{E}, \tag{2.6}$$

where we identified the electron mobility μ as being proportional to the scattering time τ. Mobility is the most frequently cited quality number of 2DES. In today's best wafers it can reach values of more than 20×10^6 cm^2/Vs [13], which corresponds to mean free path lengths of the order of 0.1 mm. Yet, let us mention already at this point, that we find μ to be a poor figure of merit to predict the quality of both effects investigated in this thesis, namely the fractional quantum Hall effect at filling factor 5/2 and microwave induced resistance oscillations. We discuss these issues in chapter 5.

Inserting equation 2.6 in the current density $\mathbf{j} = ne\mathbf{v}$ we get

$$\mathbf{j} = \underbrace{\frac{ne^2\tau}{m^*}}_{\sigma} \mathbf{E}, \tag{2.7}$$

with $\sigma_0^D := \sigma^D(B = 0)$ the Drude conductivity at zero magnetic field

$$\sigma_0^D = \frac{ne^2\tau}{m^*} = ne\mu. \tag{2.8}$$

2.2.3 Conductivity at B ≠ 0

In a magnetic field electrons feel the Lorentz force $\mathbf{F} = -e(\mathbf{v} \times \mathbf{B})$ and current and electric field are not parallel any more, which makes σ and ρ tensor quantities: $\sigma \rightsquigarrow \begin{pmatrix} \sigma_{xx} & \sigma_{xy} \\ \sigma_{yx} & \sigma_{yy} \end{pmatrix} = \begin{pmatrix} \sigma_L & -\sigma_H \\ \sigma_H & \sigma_L \end{pmatrix}$ and $\rho \rightsquigarrow \begin{pmatrix} \rho_L & \rho_H \\ -\rho_H & \rho_L \end{pmatrix}$ where we have used Onsager reciprocity. We also assumed isotropy and introduced the longitudinal and Hall quantities. As σ and ρ are still inverse to each other we find

$$\rho_L = \frac{\sigma_L}{\sigma_L^2 + \sigma_H^2} \tag{2.9}$$

$$\rho_H = \frac{\sigma_H}{\sigma_L^2 + \sigma_H^2} \tag{2.10}$$

These are just mutual relations, now let us find the actual quantities. It is easiest to calculate the resistivity components. A current is driven in $x-$direction. Because boundary conditions impose $j_y = 0$, the Lorentz force is balanced by a Hall field E_y. Classically, the motion in the direction of the current is not affected by B and $\rho_L = E_x/j_x$ is the Drude resistivity introduced above. To find the Hall resistivity $\rho_H = E_y/j_x$ we insert the definition of the current density $j_x = nev_x$ and the Hall field $E_H = v_x B_z$ created by the Lorentz force. We obtain

$$\rho_L = \frac{1}{ne\mu} \tag{2.11}$$

$$\rho_H = \frac{B}{ne} = \rho_L \omega_c \tau. \tag{2.12}$$

The last equality relates the Hall resistivity to the electron mobility (via ρ_L) and the product of the scattering time and the cyclotron frequency

$$\omega_c = \frac{eB}{m^*}. \tag{2.13}$$

The product $\omega_c\tau$ measures how many cyclotron orbits an electron can perform before its momentum is randomized. ρ_H is smaller than ρ_L when no full orbit can be completed. It gets larger when many orbits can be completed and

$$\omega_c\tau > 1 \quad \Longleftrightarrow \quad B[\mathrm{mT}] > 1/\mu[10^7\ \mathrm{cm}^2/\mathrm{Vs}] \tag{2.14}$$

This case is sometimes referred to as "classically strong magnetic field". The scattering time τ is here the momentum relaxation time. We will later introduce the quantum lifetime τ_q as another scattering time (see section 2.5).

We summarize the conductivity and resistivity as

$$\sigma^D = \frac{\sigma_0^D}{1+(\omega_c\tau)^2} \begin{pmatrix} 1 & -\omega_c\tau \\ \omega_c\tau & 1 \end{pmatrix} \tag{2.15}$$

$$\rho^D = \rho_0^D \begin{pmatrix} 1 & \omega_c\tau \\ -\omega_c\tau & 1 \end{pmatrix} \tag{2.16}$$

where the Drude index D reminds us that these are purely classical quantities. For a 2DES in a magnetic field quantum mechanical effects become essential: The longitudinal resistance deviates from the classical result in an oscillatory, $1/B-$periodic way. These oscillations are referred to as Shubnikov-de-Haas oscillations (SdH). This is due to a quantum mechanical modification of the DOS which is no longer constant even in the single particle picture. Rather, the

DOS is a ladder of levels with a broadening Γ and a $B-$proportional spacing $\hbar\omega_c$. For large magnetic fields the SdH oscillations develop into the integer quantum Hall effect with vanishing longitudinal resistance and quantized Hall resistance. We discuss these quantum mechanical effects in section 3.1.

2.3 GaAs/AlGaAs heterostructure design

To observe the effects discussed in this thesis the used heterostructures have to be of exceptional quality. Furthermore they have to be specially designed for the specific effect one wants to see and therefore require an iterative cooperation with epitaxial growers. A very fruitful cooperation exists with Vladimir Umansky in the group of Prof. M. Heiblum at the Weizmann Institute of Science (Israel) who kindly provided all the wafers. A nontrivial part of this PhD work was the identification of suitable wafers. Here we review the basic parameters of interest for GaAs/AlGaAs heterostructures.

2.3.1 Overview of design parameters

Crucial for the design of heterostructures is the relative band alignment of GaAs and $Al_xGa_{1-x}As$ where x measures the Al content. Figure 2.2 shows that the conduction band offset between GaAs and $Al_xGa_{1-x}As$ increases up to roughly 45% aluminium. The doping to provide electrons in the well is done in $Al_xGa_{1-x}As$ at a certain distance from the well, named setback distance or spacer thickness (see Fig. 2.1). Besides the purity of the used materials, various design parameters influence the properties of the 2DES:

- doping method
- spacer thickness
- Al content next to the well and in doping region
- quantum well width
- others, e.g. incorporation of a backgate

2.3.2 Details on doping method

DX-centers

A doping atom in an otherwise neutral crystal can often be described by the Bohr atomic model using the effective mass and dielectric constant of the host

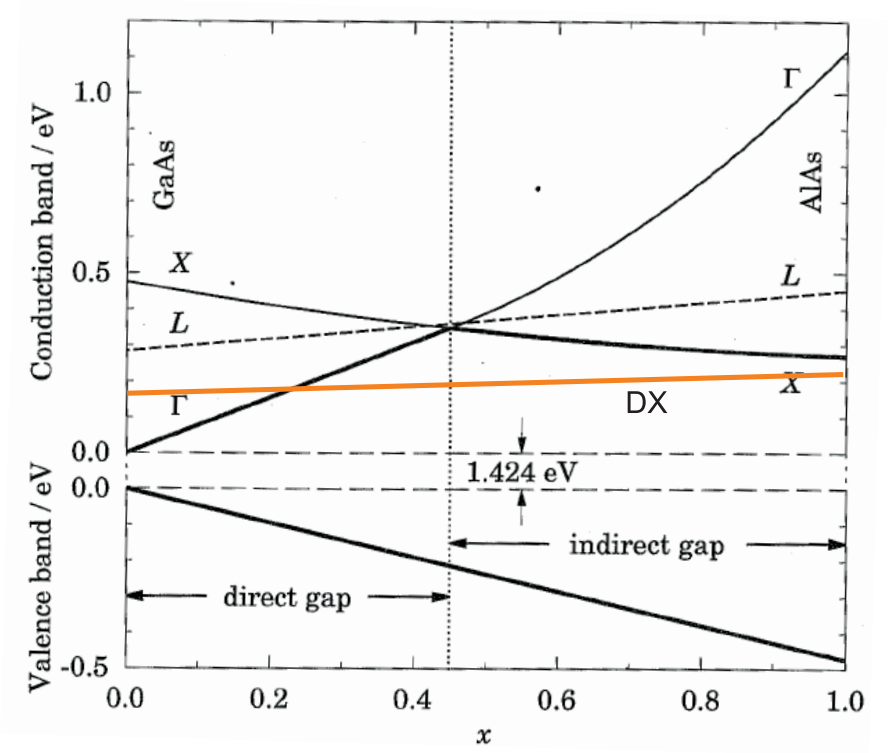

FIGURE 2.2: (adapted from [14]) Conduction bands and valance band energies in $Al_xGa_{1-x}As$ as a function of the aluminum concentration x. In red the energy of DX centers. DX centers form only for x > 20%

crystal. For GaAs this predicts a binding energy of $\approx$ 5 meV. However, if AlGaAs is doped with silicon the donor atom can distort the crystal to form a so called DX center [14, 15], which has two interesting properties. First, the binding energy depends strongly on the aluminum content of the surrounding AlGaAs. It is shown in Fig. 2.2 and can be as high as 160 meV. The spatial extension of the wavefunction of the bound donor electron depends on the binding energy and therefore on the aluminum content. Second, an energy barrier needs to be overcome also for the *trapping* of the electron as sketched in Fig. 2.3. This leads to the phenomenon of persistent photoconductivity: At low temperatures the thermal energy is not sufficient for retrapping the electron in the DX state. Once released, for example by illumination with an LED, it remains free and contributes to conduction. Illumination at low temperatures can thus be used to permanently increase the electron density.

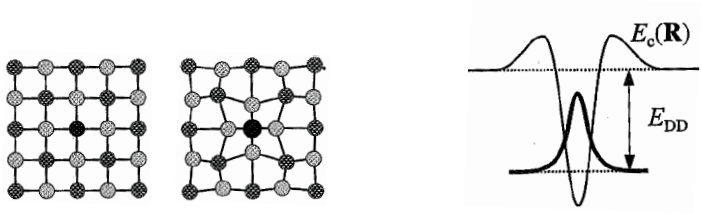

FIGURE 2.3: (adapted from [14]) Left: Crystal distortion forming a DX center. Right: Sketch of energies in a DX center. An energy barrier is present for release *and* trapping of the electron.

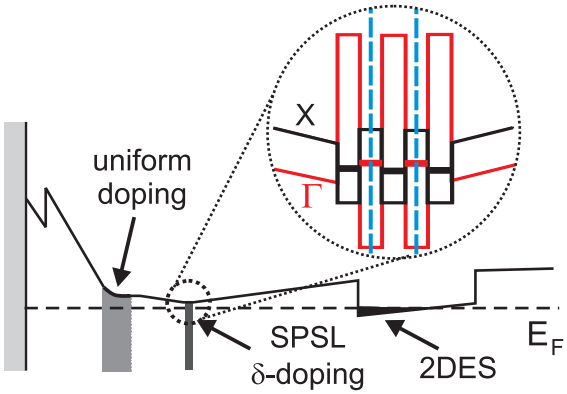

FIGURE 2.4: (adapted from [13]) Conduction band of a typical single-side doped sample. Magnification of the SPSL doping region with the actual doping marked in blue. A uniform doping compensates surface states.

Overdoping and parallel conduction

When the amount of doping atoms is increased, the electron density in the QW increases only up to a certain point and then saturates. This happens when the amount of doping is enough to bring the donor energy level down to the Fermi energy. Electrons then accumulate also in the donor layer and the 2DEG density in the QW remains fixed (see section 2.4). Overdoping can increase the quality of the 2DES because the disorder potential from the ionized donor atoms can partly be screened by the electrons in the donor layer itself. The beneficial effect of this screening on the FQHE and especially the 5/2 state was investigated [13,16]. However, overdoping also leads to parallel conduction, which is an undesired effect. This problem can partly be solved as described in the next paragraph.

Short period superlattice doping (SPSL)

The goal of this special doping method, proposed already in 1983 [17] and later refined [18], is to have overdoping for screening without much parallel conduction. The idea is the following: The X-band in AlAs has a very high effective mass and consequently low mobility (see equation 2.6). Electrons remaining in such a donor layer might be mobile enough to partly screen the disorder potential of the ionized donor atoms, yet contribute poorly to parallel conduction. The doping itself is not done in AlAs to avoid DX centers. Instead, a short period superlattice is grown of alternating GaAs and AlAs layers. Doping atoms are put in single sheets (δ-doping) in the middle of the GaAs miniwells. If the GaAs wells are sufficiently narrow the quantization energy of the Γ band is high (see equation 2.1) and exceeds the AlAs X band (see Fig. 2.4). The doping electrons remaining in the SPSL then have the X character of the AlAs with the benefit of high effective mass. We emphasize that the single particle picture can *not* be quantitatively applied for neither the quantization energy nor the effective mass in the SPSL, but it helps in understanding the idea.

The SPSL overdoping method has proven very successful for highest quality 2DES and the beneficial effect of *over*doping has explicitly been assessed (see Ref. [13] and, for DX doping, Ref. [16]). In fact, most of the FQHE data in this thesis have been measured on such samples. These samples have, in addition to the SPSL, a second, uniform doping region above the SPSL to provide charges for compensation of surface states. This has proven useful, even though the exact effect of separating the dopings is hard to quantify experimentally.

Unfortunately, the SPSL overdoping also has a drawback: Surface gates have a higher chance of being leaky and especially the surface single electron transistors that we use to investigate microwave irradiation effects can not be operated on such samples. This posed strong restrictions on the choice of wafers for such experiments as we will describe in chapter 5.

2.3.3 Details on spacer thickness

The spatial distance between the QW and the doping atoms (the spacer thickness) is a crucial parameter. On the one hand, it should be as small as possible as this increases the maximum electron density (see below equation 2.17). On the other hand, the ionized donor atoms produce a random potential that acts as (smooth) disorder for the 2DES and thus should be kept as far away as possible.

The role of spacer thickness for electron mobility is well understood [19]. In typical high quality samples with a spacer thickness of $\geq$ 70 nm the disorder

from remote ionized donors contributes only about 10 % to the mobility. The rest comes mainly from residual impurities in the QW itself. However high mobility does not guarantee pronounced FQHE states (see section 5.3.1). In fact, we have found reason to believe that the disorder from doping plays a substantial role for the FQHE (see chapter 6).

2.4 Design influence on 2DES parameters

Here we mention some very straightforward consequences of the heterostructure design on the 2DES. The maximum density, the occupation of higher subbands and the shape of the wavefunction are all well understood. They can be predicted accurately from simple theoretical models using Poisson and Schrödinger equations. Less well predictable properties that have to be assessed experimentally are deferred to the next section.

Maximum density

The maximum electron density n in a QW is obtained from the parallel plate capacitor model where the doping layer and the QW act as plates:

$$n = \varepsilon\varepsilon_0 \frac{\Delta E_c}{ed} \tag{2.17}$$

Here $\varepsilon = 12.8$ is the dielectric constant of GaAs, d the spacer thickness and ΔE_c the conduction band offset between the QW and the donor energy level. ΔE_c depends on the aluminum content of the material that hosts the doping, the nature of the doping (DX center) and in the case of SPSL doping on the thickness of the miniwells.

For typical high-mobility GaAs/AlGaAs wafers typical electron densities are $1 - 3 \times 10^{11}/\mathrm{cm}^2$. High densities are desirable for two reasons:

1. Screening of disorder gets better with increasing density.

2. The Coulomb interaction energy E_q scales with the inverse of the average electron separation and thus $E_q \sim \sqrt{n}$.

The FQHE exists solely by virtue of the electronic Coulomb interaction and is therefore strengthened with increasing electron density. We will come back to this in section 3.2.

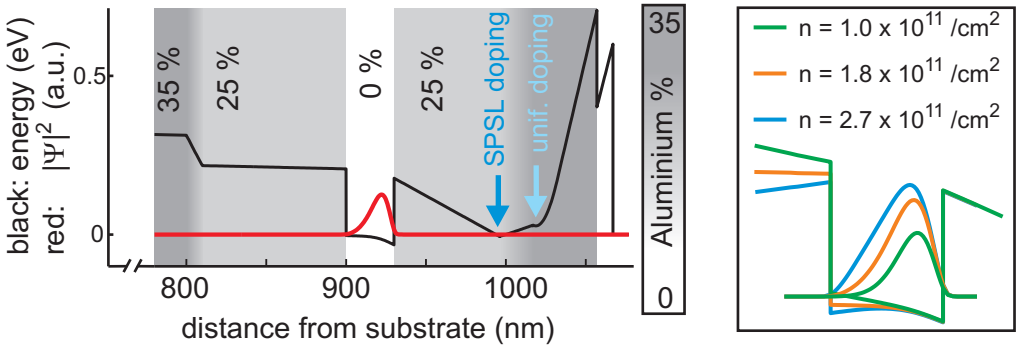

FIGURE 2.5: Left: Conduction band energy (black) and electron wavefunction (red) for our wafer 8-332. The aluminum content is given in greyscale. Near the substrate there is a highly doped region acting as backgate (not shown) to tune the electron density. Right: Wavefunction shape in the well for three backgate voltages resulting in different densities.

Occupation of subbands

We calculated the Fermi energy and the energy levels of different subbands in a QW in section 2.1 in a single particle approximation. Comparing equations 2.1 and 2.3 we can estimate how many subbands will be occupied for a given density. Even though we used the single particle picture the estimate is usually quite good. Occupation of multiple subbands should be avoided because the additional inter-subband scattering reduces mobility and substantially modifies the FQHE (for example [20] and our own observations). Occupation of the second subband is seen in low-B transport measurements as a beating pattern in the SdH-oscillations. From a Fourier analysis the densities occupying each subband can be extracted.

Shape of the wavefunction

The shape of the wavefunction in the quantum well is in a first approximation not relevant for the QHE. At a closer look, however, if the electrons have more space in the direction perpendicular to the 2D plane, the Coulomb interaction is effectively weakened. This affects the pronouncedness of the FQHE (see chapter 6). Furthermore, the well is bent upwards in the middle. For very wide wells the electron density can develop a minimum in the middle of the well and bilayer effects become important [20].

The shape of the wavefunction can be obtained from the self consistent solution of the Poisson and the Schrödinger equations. We used the freely available software nextnano3 (Nanodevice simulator, spinoff from WSI, TU Munich, Germany, www.nextnano.de). Figure 2.5 gives exemplary results for wafer 8-332,

a single-side SPSL doped sample with an in-situ grown backgate that we used for most FQHE measurements in this thesis.

2.5 Electron mobility and quantum lifetime

We introduce two scattering times [14, 21]:

$$\frac{1}{\tau} = \int f(\theta)(1 - cos\theta)d\theta \tag{2.18}$$

$$\frac{1}{\tau_q} = \int f(\theta)d\theta \tag{2.19}$$

where θ is the angle of electron scattering and $f(\theta)$ measures the probability of scattering. The first one emphasizes large angle scattering and is the momentum relaxation time introduced with the electron mobility in equation 2.6. The second one is called quantum lifetime or single particle lifetime. It counts all scattering events, also small angle scattering which hardly affects momentum. Therefore τ_q is not reflected in the electrical resistance at $B = 0$. Both scattering times are - or can be - due to *elastic* scattering. Here we review some properties of these two quantities.

The ratio τ/τ_q can be used to identify the dominant scattering mechanism: Mostly background impurity scattering (sharp potentials) will result in predominant large angle scattering. If scattering is mostly from remote impurities (smooth potential) then τ_q will be much smaller than τ. A recent paper gives $\tau/\tau_q \gtrless 10$ as a rule of thumb to distinguish between the two cases [22]. A typical value for modulation doped high-quality GaAs/AlGaAs heterostructures is $\tau/\tau_q = 100$ which indicates that small angle scattering is of little relevance for mobility in these samples.

2.5.1 Electron mobility

The electron mobility is measured in standard four terminal transport measurements at zero magnetic field as $\mu = 1/en\rho$ (see section 2.2.3). The density is determined from the slope of the Hall curve or the $1/B$ period of SdH oscillations. The resistivity ρ can be obtained from measuring the resistance and dividing by the aspect ratio (length/width) of the sample.

The mobility is, in todays best GaAs/AlGaAs heterostructures, largely limited by scattering from background impurities in the QW. This is found both from experiments [19] and from a theoretical analysis [23] evaluating various scattering mechanisms, namely background impurities, remote ionized donors

and phonon scattering mechanisms (which play no role at temperatures below 1K). The authors of Ref. [23] propose that without changes in wafer design mobilities up to $100 \times 10^6 \mathrm{cm}^2/\mathrm{Vs}$ can be reached if the background impurity concentration can be lowered to $10^{12}/\mathrm{cm}^3$.

The mobility-limiting mechanism can also be identified from the density dependence of the mobility, as theories propose

$\mu \sim n$ for background impurity scattering
$\mu \sim n^{1.5}$ for remote impurity scattering.

Both relations are not exact and predictions vary a bit for different references [23–26] (an exponent of 0.6 has been measured on low-density samples [27]). Furthermore, in the older references parameters are chosen such that typical mobilities of that time are reproduced. Now mobilities are about two orders of magnitude larger. For these reasons, conclusions from the density dependence of μ should be taken with care (see section 5.4.1).

2.5.2 Quantum lifetime

Small angle scattering does not translate into an electrical resistance and has no relevance for classical effects, especially electron mobility. Taking quantum mechanics into account, however, also small angle scattering is important. It can destroy phase coherence and also contributes to level broadening. The latter will be discussed in section 3.1.1 after Landau quantization is introduced.

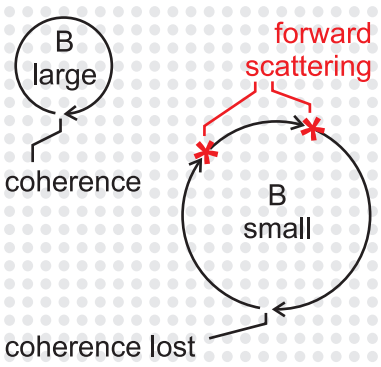

FIGURE 2.6: Forward scattering destroys phase coherence even though a full cyclotron orbit is completed.

Here we describe how the quantum lifetime can be measured from the amplitude of Shubnikov-de-Haas (SdH) oscillations. We first give an intuitive explanation of the physics. SdH oscillations are oscillations in the magnetic field dependence of the longitudinal resistance. They are a purely quantum mechanical effect and can be viewed as a result of self-interference of electrons after completing a cyclotron orbit of radius $R_c \sim 1/B$ (see table 3.2). Small angle scattering can destroy the phase coherence and suppress interference effects. The amplitude of the SdH oscillations therefore is sensitive to small angle scattering as the electron travels a cyclotron orbit. (It is of course also sensitive to large angle scattering, but this may be much rarer.) The quantum lifetime τ_q is a measure for this effect.

More quantitatively, low field magnetoresistance oscillations in a 2DES can be described by [28–31]

$$\Delta R = 4R_0 \frac{X}{\sinh(X)} \exp\left(\frac{-\pi}{\omega_c \tau_q}\right) \tag{2.20}$$

where R_0 is the resistance at $B = 0$ and $X/\sinh(X)$ is called the Dingle factor with $X = 2\pi^2 k_B T/\hbar\omega_c$. To obtain the quantum lifetime we do a standard transport measurement of R_{xx}, extract the amplitudes of the SdH oscillations and plot the logarithm of $(\Delta R \sinh X)/(4R_0 X)$ against 1/B.

Chapter 3

Quantum Hall effects

3.1 Integer quantum Hall effect

The quantum Hall effect [1] occurs when a 2DES is cooled to low temperature and is subjected to a perpendicular magnetic field. In certain B intervals the Hall resistance quantizes to

$$R_{xy} = \frac{h}{ie^2} \tag{3.1}$$

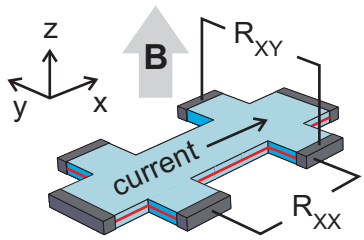

with $i = 1, 2, 3 \ldots$. As these values are independent of the sample geometry and immune to sample imperfections the effect can be used as a standard for electrical resistance. The discovery has been honored with the Nobel prize to Klaus von Klitzing in 1985.

The plateaus in R_{xy} are accompanied by vanishing R_{xx} (see Fig. 3.4), which points to the existence of an energy gap. This gap is, for the *integer* quantum Hall effect, the cyclotron energy $E_c = \hbar\omega_c$.

3.1.1 The IQHE in the single particle picture

Much of the *integer* QHE can be understood in a single particle picture. The kinetic energy term is sufficient to explain the existence of Landau levels, the cyclotron energy as the relevant energy scale and the magnetic length as the relevant length scale. The full Hamiltonian of a 2DES in a magnetic field is described by

$$\mathrm{H} = \underbrace{T^{2\mathrm{D}} + Zeeman + Disorder + Sample}_{\text{single particle}} + \underbrace{Coulomb}_{\text{many particle}} \tag{3.2}$$

where $T^{2D} = \frac{(\mathbf{p}+e\mathbf{A})^2}{2m^*}$ is the kinetic energy of an electron subjected to a magnetic field $\mathbf{B} = \nabla \times \mathbf{A}$, $Zeeman = g^*\mu_B B$ accounts for the electron spin, *Disorder* describes potential fluctuations leading to scattering, *Sample* describes the confining potentials in z and $x-y$ direction, and $Coulomb = \Sigma_{i<j} \frac{e^2}{4\pi\varepsilon\varepsilon_0} \frac{1}{|\mathbf{r}_i - \mathbf{r}_j|}$ the electron-electron interactions.

Kinetic energy term: explaining the essentials

The solution of the kinetic energy problem, that is the Schrödinger equation of an electron in a magnetic field, can be found in any quantum mechanics textbook (for example [14] or, more advanced, [32]). In table 3.1 we summarize the results. (We neglect some subtleties that are not important for illustration purposes. The textbooks provide more details.)

A word on gauge freedom for the vector potential is in order: The shape of single particle wavefunctions depends on the gauge that is used. Measurable quantities such as energies and density of states do not. In fact, any argument based on the shape of wavefunctions is suspicious and should not be used (like the "lines" in Landau gauge and their distance in y-direction depending on the sample size in x-direction)[1]. We now describe the physical, gauge-independent features obtained from the kinetic energy term:

Existence of Landau levels and energy scale. In a magnetic field the DOS is no longer constant (equation 2.4) but is a series of discrete Landau levels (LL), separated by the cyclotron energy

$$E_c = \hbar\omega_c \tag{3.3}$$

$$E_c^{\mathrm{GaAs}}[\mathrm{meV}] = 1.73 \times B[\mathrm{T}]. \tag{3.4}$$

Note that this energy gap is precisely the energy quantum corresponding to the cyclotron frequency (see equation 2.13) which has a classical origin.

Landau level degeneracy, flux quanta and filling factor. The solutions of the Schrödinger equation presented in table 3.1 allow an infinite number of states in each LL, provided that the 2D plane is infinitely large. The number of states per unit area is obtained by imposing that $y_m < L_y$ (in Landau gauge). We get the LL degeneracy

$$n_L = \frac{eB}{h} = \frac{B}{\Phi_0} \tag{3.5}$$

[1] What *can* be used are properties of the wavefunction that do not depend on gauge, like the increasing number of nodes for higher LL.

LANDAU GAUGE:
$\mathbf{A} = (-By, 0, 0)$

$\Psi_{j,m} = \mathrm{Osz}_j(\frac{y-y_m}{l_B})e^{ik_m x}$

$\mathrm{Osz}_j(y) = H_j(y)e^{-y^2/2}$
H_j = Hermite polynomial
$k_m = \frac{2\pi}{L_x}m, \quad m = 1, 2, 3, \ldots$
$y_m = l_B^2 k_m$
norm: $(\pi 2^{2n}(n!)^2)^{-1/4}$

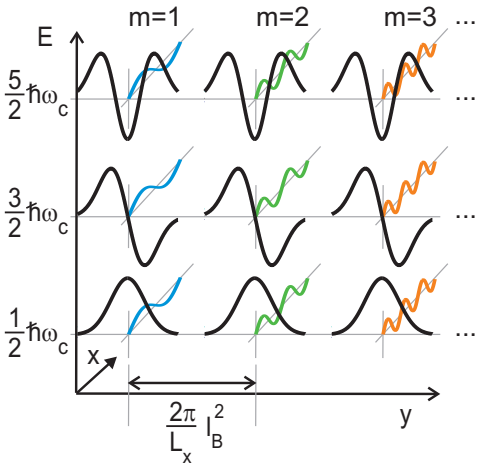

- different LL, different wavefunctions in y-direction
- all k_m degenerate in energy
- $\Sigma|\Psi|^2$ has stripes in x-direction

SYMMETRIC GAUGE:
$\mathbf{A} = B/2\,(-y, x, 0)$

$\Psi_{j,m} = (z/l_B)^m L_j^{|m|}(\frac{r^2}{2l_B^2})e^{-\frac{r^2}{4l_B^2}}$

$L_j^{|m|}$ = ass. Laguerre polynomial
$m = \ldots, -1, 0, 1, \ldots$
$z = re^{i\phi} = (x, y)$
$< r^2 >= l_B^2(2m+1)$
norm: $\sqrt{\frac{n!}{2\pi 2^m (m+1)!}}$

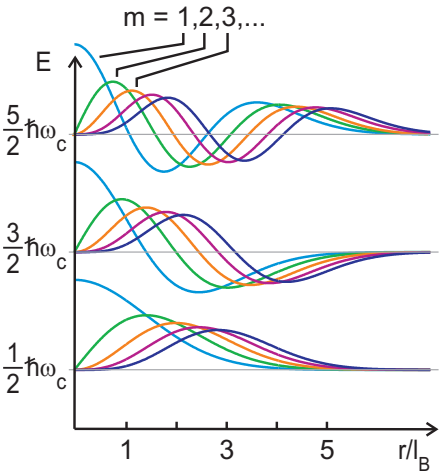

- different LL, different main Laguerre index
- all m degenerate in energy
- $\Sigma|\Psi|^2$ is homogeneous disk of radius $\approx l_B\sqrt{m}$

GAUGE INDEPENDENT:

- $E_j = \hbar\omega_c(j + \frac{1}{2})$, $j = 0, 1, \ldots$, degenerate in m, $\quad \omega_c = \frac{eB}{n}$, $\quad l_B = \sqrt{\frac{\hbar}{eB}}$
- higher LL have increasing number of nodes in wavefunction

TABLE 3.1: Wavefunctions of a charged particle in a B-field for different gauges. Note that in the graph's z-axes we mix wavefunction amplitude and energy.

with the magnetic flux quantum $\Phi_0 = h/e$. We find that *in each LL one electron occupies an area of one magnetic flux quantum* (if electrons were spinless).

In order to find the number of occupied LLs for a given electron density (neglecting spin) we divide the number of electrons by the number of states per LL. This ratio is referred to as the filling factor ν:

$$\nu = \frac{n}{n_l} = \frac{nh}{eB} \tag{3.6}$$

Magnetic length - the relevant length scale. The solutions of the Schrödinger equation have as a length scale the magnetic length

$$l_B = \sqrt{\frac{\hbar}{eB}} \tag{3.7}$$

$$l_B[\mathrm{nm}] = \frac{25.7}{\sqrt{B[\mathrm{T}]}}. \tag{3.8}$$

The area of one flux quantum, which is the area occupied by one electron in a LL, can be expressed in terms of the magnetic length as $A^{\mathrm{el}} = 2\pi l_B^2$.

As a reference table 3.2 lists some frequently used quantities related to the quantum Hall effect. We express them in two ways: First, in experimental parameters like B-field and electron density n, and second through scales like the magnetic length l_B and the Fermi wave vector $k_F^{\mathrm{2d}} = \sqrt{2\pi n}$.

Zeeman term: introducing spin

The Zeeman term does not introduce anything conceptually new except that Landau levels are spin-split by the Zeeman energy

$$E_Z = g^* \mu_B B \tag{3.9}$$

where $\mu_B = e\hbar/2m = 57.88\,\mu\mathrm{eV/T}$ the Bohr magneton. The value of the g^*-factor for bulk GaAs is $g^* = -0.44$, but in a 2DES it can be considerably enhanced due to exchange interactions [33]. The ratio of the cyclotron and Zeeman energies

$$\frac{\hbar\omega_c}{g^*\mu_B B} = 2\frac{m}{m^*}\frac{1}{g^*} \tag{3.10}$$

has a value of 67.8 assumging $g^* = -0.44$. Even for exchange enhanced g^* the Zeeman energy is usually much smaller than the cyclotron energy. Figure 3.1 shows the spin-split LLs evolving with magnetic field.

quantity	in experimental parameters	in scales
LEVEL DEGENERACY $n_L = \frac{number}{area}$	$= \frac{eB}{h}$	$= 1/2\pi l_B^2$
FILLING FACTOR $\nu = n/n_L$	$= \frac{hn}{eB} = \frac{n\Phi_0}{B}$	$= k_F^2 l_B^2$
CYCLOTRON FREQUENCY ω_c	$= \frac{eB}{m^*}$	$= \frac{\hbar}{l_B^2 m^*}$
CYCLOTRON RADIUS $R_c = \frac{mv_F}{eB} = \frac{\hbar k_F}{eB}$	$= \sqrt{2\pi n}\frac{\hbar}{eB}$	$= k_F l_B^2 = \nu/k_F$

TABLE 3.2: Frequently occurring quantum Hall quantities

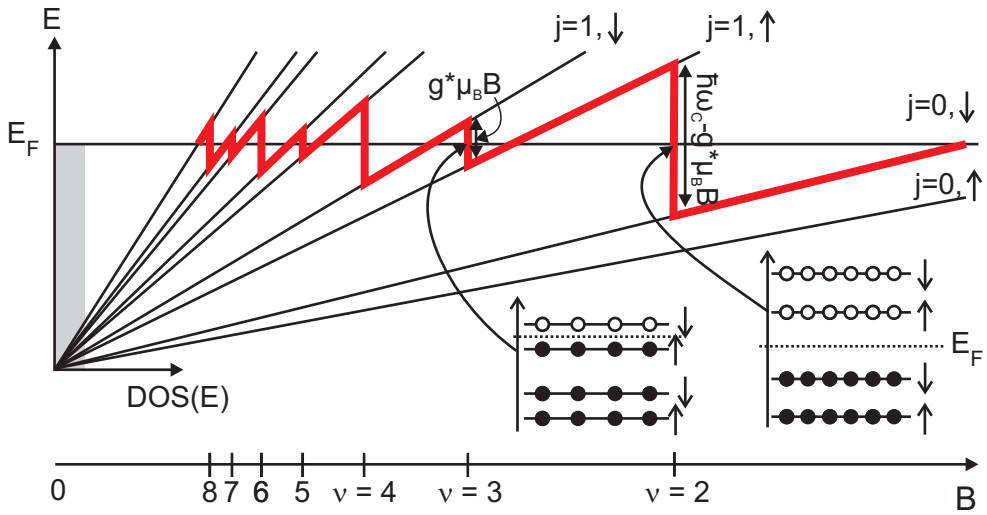

FIGURE 3.1: (Adapted from [34]) Spin-split Landau levels as a function of magnetic field. The interplay of increasing cyclotron and Zeeman energy and increasing LL degeneracy as a function of B yields a sawtooth like behavior of the chemical potential with an average value $\mu^{\mathrm{ch}}(B = 0)$.

Sample term: Confining the electrons

In a Hall bar electrons are confined in two different ways: In the direction perpendicular to the 2D plane, usually referred to as the z direction, electrons are confined in a narrow well (about 30 nm in our samples).

Electrons are also confined in the $x - y$ direction because a real Hall bar has edges (our typical Hall bars have $L_x = 1$ mm, $L_y = 400$ μm). In a simple picture this is described by an upward bent of the LLs at the edges. When a LL crosses the Fermi energy, an edge channel forms [35]. It is well established that edges play an important role in the physics of the QHE [36–38]. Yet, the simple edge channel picture is modified when electron-electron interactions are taken into account, as we describe in section 3.1.3.

Disorder term: level broadening and beyond

Disorder is inevitable in a real sample. In a very common picture disorder is described by a LL broadening Γ. The shape of broadened levels depends on the scattering potentials [39]. Two frequently used models yield a half-elliptic or a Gaussian broadening. The latter is illustrated in Fig. 3.2. In a simple approximation the Heisenberg uncertainty principle relates the level broadening to the average time between scattering events [14]. This yields $\Gamma = \hbar/\tau_q$. Note that we used the quantum lifetime 2.19 because all scattering events count equally. In the above approximation the level broadening does not change with magnetic field. Taking screening differences into account within the self-consistent Born approximation one finds for strong magnetic fields a B-dependent broadening $\Gamma = \hbar\sqrt{2\omega_c/\pi\tau_q}$ [39].

A more sophisticated way to treat disorder than a simple level broadening has been put forward: electrons move in a network of resistors formed by saddle points separating percolation clusters in the disorder potential landscape. The dissipative resistance originates from tunneling through these saddle points [40]. This has recently been adapted to the FQHE [41]. We will come back to both models in section 6.2 when we discuss the energy gap of the 5/2 state.

3.1.2 Density of states: B-field dependence

The combination of LL formation and LL broadening by disorder determines the magnetic field dependence of the density of states (DOS). Figure 3.2 shows how the DOS changes with increasing magnetic field from a continuum into a set of discrete levels. The transition is governed by the ratio of the cyclotron energy and the LL broadening. Using the approximation $\Gamma = \hbar/\tau_q$ from the

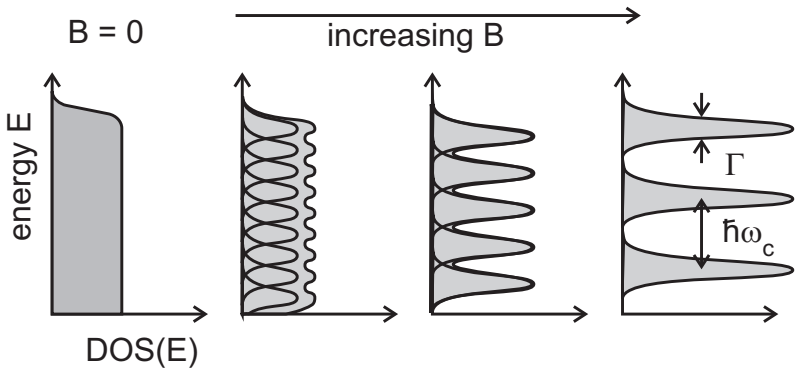

FIGURE 3.2: Magnetic field evolution of the density of states (DOS): Landau levels become separated when the cyclotron energy gets larger than the level broadening Γ. (Shown is actually the DOS multiplied by the Fermi occupation function for some finite temperature.) The level degeneracy increases with B such that the integrated DOS stays, on average, constant. Spin splitting is neglected.

last section we get

$$\Gamma > \hbar\omega_c \quad \Longleftrightarrow \quad \omega_c\tau_q > 1 \tag{3.11}$$

This criterion is different from equation 2.14 for a classically strong magnetic field: τ is replaced by τ_q, which can be much smaller (see section 2.5). To fulfill the criterion 3.11 (separated LLs) thus requires larger $B-$fields than 2.14 (Hall and longitudinal resistance comparable).

At low magnetic fields where the DOS has small oscillations the longitudinal resistance shows Shubnikov-de-Haas oscillations [31]. This is usually the regime where microwave induced resistance oscillations (MIRO) are observed. These are discussed in the next chapter.

At larger magnetic field when LLs become separated the QHE takes over and R_{xx} vanishes in finite $B-$intervals (see below).

An important aspect of level broadening in view of the measurements performed in this thesis is that it effectively reduces the energy gap between levels by an amount Γ.

3.1.3 Interactions in the IQHE

The interaction-free treatment of the IQHE yields the important concepts of LLs, filling factor and magnetic length. However, a more complete treatment taking electron-electron interactions into account is needed to understand localization physics and the importance of the sample edges.

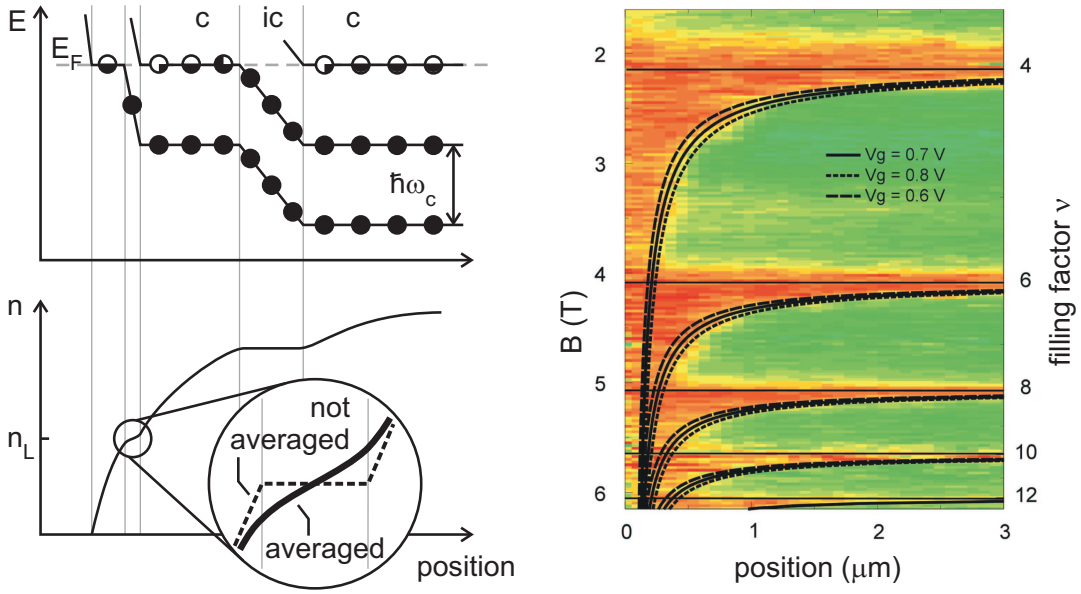

FIGURE 3.3: Left: Electron screening leads to compressible (c) and incompressible (ic) strips. Magnification: A too narrow strip is smeared out and looses its incompressible character. Right: (from [38, 43]) Hall potential (color) measured from the sample edge for various magnetic fields. Shown also (black lines) the theoretical prediction for the position of incompressible strips according to [44]. The potential drop occurs where the innermost incompressible strip is predicted.

Details on localization

The existence of localized states can be understood without interactions: In a disordered potential landscape electrons in a magnetic field will wind around potential hills or valleys (see for example [38]). Yet, the non-interacting picture can not explain some striking findings [42]: The number of localized states in a LL is *constant* over the entire magnetic field range (except at low fields where LL are not fully developed). This is in sharp contrast to the *increasing* LL degeneracy (see equation 3.5) and implies that localization physics in the QHE is dominated by Coulomb interactions.

Compressible and incompressible strips

We mentioned above that at the edge of the sample LLs are bent upwards and cross the Fermi energy leading to edge channels. This simple picture predicts an unphysical stepwise change in the electron density. Coulomb interaction clearly favors a smooth decrease towards the edge. As first described in [35] this leads to two different types of regions (see Fig. 3.3):

Compressible strips: the electron density varies smoothly, keeping the highest occupied LL pinned to the Fermi energy.

Incompressible strips: LLs bend upwards while the electron density stays constant. The local filling factor has an integer value. There are no free states at the Fermi energy due to the energy gap $\hbar\omega_c$.

Due to the energy gap and the integer value of the locall filling factor *current can flow without dissipation in incompressible strips*. A non-equilibrium current driven through the sample favors these regions.[2] The Hall potential is thus expected to drop in the incompressible strips (see equation 3.12 below). Their position changes with the overall filling factor as illustrated in the right panel of Fig. 3.3. The potential distribution across a Hall bar could be measured with a scanning force microscope [38, 45, 46] and later with a single electron transistor [47,48]. It was found to drop at the position where the innermost incompressible strip is expected. Those experiments continue to be pursued [34]. Detailed calculations [37] show that density variations are smeared out on the order of the magnetic length. Very narrow incompressible strips loose their incompressible character. This explains why the potential drop is observed only at the innermost incompressible strip. The excellent agreement between theory and experiment apparent in Fig. 3.3 supports the theory of compressible and incompressible strips. The relevance of incompressible strips for the quantization of the Hall resistance is discussed below.

3.1.4 Origin of quantized Hall resistance

We identified the relevant energy and length scales of the IQHE problem. Yet, the big question remains: Why is the Hall resistance quantized?

To answer this question we follow [36,37]. We assume that Ohm's law holds locally: $E_H(y) = \rho_H(y) j_x(y)$ where y is the direction transverse to the imposed current j_x. We write the filling factor (see equation 3.6) as $B = \frac{nh}{e\nu}$. Substituting this into the Hall resistance $\rho_H = B/ne$ we find locally

$$E_H(y) = \underbrace{\frac{h}{e^2}\frac{1}{\nu(y)}}_{\rho_H(y)} j_x(y) \tag{3.12}$$

[2]The reason for this is sometimes given as follows: Longitudinal current is driven by the Hall field, and because the compressible strips are compressible, they screen Hall fields. This is not true. A Hall field in a compressible region is not forbidden and indeed this is what happens when no incompressible strip exists. Rather, the energy gap in incompressible strips is important: It makes transport dissipationless and thus current favors these regions.

This relation is true even if no Hall plateaus exist (for example due to high temperature) and does not in itself explain the resistance quantization. Rather, the key ingredient is that current flows in incompressible strips with a filling factor that locally takes on an integer value, as described above. By integrating 3.12 over the width of the sample we get $U_H = \frac{h}{e^2}\frac{1}{\nu_{\mathrm{IS}}} I_x$ where ν_{IS} is the filling factor of the incompressible strip carrying the current. *The Hall resistance is quantized because the current is carried in regions with precisely integer filling factor.* The finite $B-$intervals over which quantized Hall resistance and vanishing longitudinal resistance are observed range from the onset of an incompressible strip in the middle of the sample down to the point when the strips become too narrow and loose their incompressible character [37]. We mention that disorder and localization also plays a role for the shape of quantum Hall plateaus and refer to [36].

3.2 Fractional quantum Hall effect (FQHE)

The first indication of a QHE at a non-integer filling factor was seen at $\nu = 1/3$ in 1982 [2]. As sample quality increased, more and more FQHE states were observed. The number is believed to increase further with sample quality and lower temperature. In Fig. 3.4 many fractional states can be identified. They occur most prominently at high magnetic fields when only the lowest LL is partially populated, but are also observed at lower fields where they mix with IQHE states. In this thesis we are particularly interested in filling factor $5/2 = 2 + 1/2$, which lies in the second excited LL.

3.2.1 Energy scale of the FQHE: Coulomb interactions

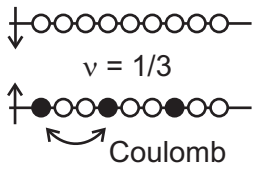

The FQHE arises *solely* from Coulomb interactions. To see this, we picture the situation of filling factor 1/3: The energy is quantized into LLs (see section 3.1.1) and at 1/3 only the lowest, spin-split Landau level is occupied. The kinetic energy is *not in the problem any more* as all electrons have the same kinetic energy $\hbar\omega_c/2$. Only the Coulomb interaction remains (except for disorder) and the problem is intrinsically a many-body problem. The Coulomb energy is proportional to the inverse (average) distance d between electrons, namely $E_q = e^2/4\pi\varepsilon\varepsilon_0 d$. In two dimensions we have $1/d = \sqrt{n}$ and therefore

$$E_q = \frac{e^2}{4\pi\varepsilon\varepsilon_0}\sqrt{n}. \tag{3.13}$$

All energies associated with the FQHE are therefore expected to scale with the square root of the electron density.

We rewrite 3.13 in a slightly different form for reasons given below. Using $n = \nu/2\pi l_B^2$ we find $E_q = e^2\sqrt{\nu/2\pi}/4\pi\varepsilon\varepsilon_0 l_B$. For a given filling factor the Coulomb energy is proportional to the inverse magnetic length. Theorists usually normalize all energies of the FQHE by (numbers are for GaAs)

$$E_q^0 = e^2/4\pi\varepsilon\varepsilon_0 l_B \tag{3.14}$$

$$E_q^0[\mathrm{meV}] = 4.35 \times \sqrt{B[\mathrm{T}]} \tag{3.15}$$

$$E_q^0[\mathrm{K}] = 50.5 \times \sqrt{B[\mathrm{T}]}. \tag{3.16}$$

Coulomb energy of higher LL states

We need to address some subtleties here. For FQHE states occurring in higher LLs only the electrons of the partially occupied LL are important. The completely filled LLs can be regarded as inert. We sketch the situation for $\nu = 5/2$ where only 1/5 of the electrons takes part in the correlated state. The density in 3.13 has to be replaced by $n/5$. This is conveniently done by introducing the fractional part $\widetilde{\nu}$ of the filling factor as $\nu = i + \widetilde{\nu}$ with an integer i. The relevant Coulomb energy then is $E_q = e^2\sqrt{\widetilde{\nu}/2\pi}/4\pi\varepsilon\varepsilon_0 l_B$.

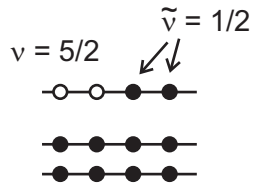

Coulomb energy of particle-hole conjugate states

For particle-hole conjugate states (like 2/3 is conjugate to 1/3 in the spin-polarized case) the relevant density for the Coulomb interaction is the density of holes, not electrons. For example, going from 1/3 to 2/3 by reducing the magnetic field, both states have the same electron density. Yet the hole density at 2/3 is only half the electron density. This factor is taken care of by the magnetic length. In normalized units 2/3 and 1/3 have the same energy scale.

We can thus summarize the Coulomb energy relevant for FQHE states as

$$E_q = \frac{e^2}{4\pi\varepsilon\varepsilon_0 l_B}\sqrt{\widetilde{\nu}/2\pi}, \tag{3.17}$$

with $\widetilde{\nu}$ as the fractional part of the filling factor of electrons or holes respectively in the partially populated LL.

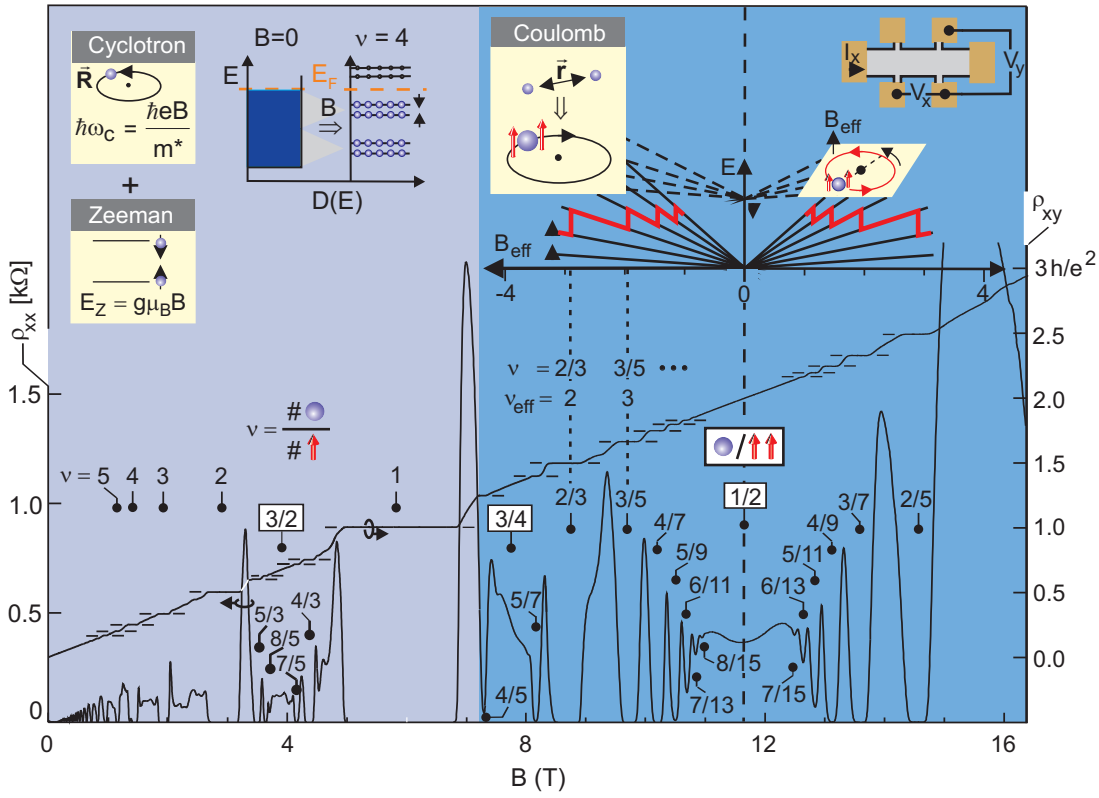

FIGURE 3.4: The integer (left part) and the fractional (right part) quantum Hall effect. (See text for details)

3.2.2 Composite fermions

The composite fermion model reveals the FQHE as the IQHE of a new kind of particles and therefore makes it accessible to intuitive reasoning. We limit ourselves to briefly describing this model in an intuitive way. A more advanced treatment can be found in Ref. [32].

Key observation: $\nu = 1/2$ has similarities with $B = 0$

Composite fermions (CF) were introduced by Jain in 1989 [6]. The idea comes from carefully observing the Hall curves shown in Fig. 3.4. In the vicinity of filling factor 1/2 they look strikingly like a large scale copy of the traces at zero magnetic field: The longitudinal resistance is finite and exhibits oscillations when going away from $\nu = 1/2$ like it does in the Shubnikov-de-Haas oscillations near $B = 0$. Farther away from $\nu = 1/2$ the minima develop into regions of

vanishing resistance. The Hall resistance develops the corresponding plateaus. The key idea of the composite fermion model is:

The fractional quantum Hall effect is the integer quantum Hall effect of a new kind of particles in an effective magnetic field.

The composite fermion model

The composite fermion model introduces new quasiparticles composed of one electron and two elementary magnetic flux quanta. The effective magnetic field is reduced by the electron density multiplied by the amount of flux attached to the electrons:

$$B^{\text{eff}} = B - 2pn\Phi_0 \tag{3.18}$$

where p is an integer that is one in our case (the composite fermion model can be extended to attach an even number $2p$ of flux quanta to each electron [32]). The effective magnetic field is zero at $\nu = 1/2$. Composite fermions behave in the effective field like electrons do in the real field. Especially, at $B^{\text{eff}} = 0$ the composite fermions form a compressible Fermi sea with a finite longitudinal resistance.

Much of the FQHE can be explained in terms of the composite fermion model. Filling factor 1/3 corresponds to effective filling factor one: The LL degeneracy of the lowest composite fermion LL is just enough to accommodate all composite fermions. Filling factor one is also effective filling factor one, but for negative B^{eff}. The relation between effective filling factor ν^* and electron filling factor ν is

$$\nu = \frac{\nu^*}{2p\nu^* \pm 1}. \tag{3.19}$$

Experimental evidence shows that composite fermions behave in certain ways like electrons. They can be magnetically focused [49] and their cyclotron orbiting motion can be detected from an increase of resistance in periodically modulated structures [50]. Also the cyclotron resonance has been measured [51].

3.3 Filling factor $\nu = 5/2$

3.3.1 Even-denominator state with an energy gap

In 1987 there was first evidence for a quantum Hall state at filling factor 5/2 [4]. Ten years later vanishing longitudinal resistance at $\nu = 5/2$ was reported [5]. This state came as a surprise because up to that time all FQHE states had odd denominators. In fact, the composite fermion picture predicts all half-filled LLs to be compressible, gapless states. Today the only other identified even

denominator state (except for 5/2's electron-hole conjugated 7/2 state) is at filling factor $2 + 3/8$. It was first observed in 2002 [52] and then confirmed in [53, 54] - even if still no vanishing R_{xx} is seen.

Greiter, Wen and Wilczek suggested [55] that the 5/2 state could be explained as a Pfaffian state, which was earlier introduced by Moore and Read [56]. They describe the 5/2 state as a p-wave paired state where the energy gap comes from a BCS-like pairing of two composite fermions, see Fig. 3.5.

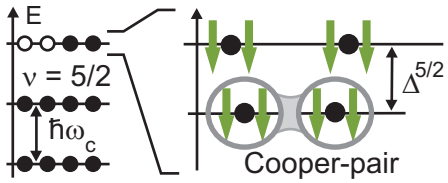

FIGURE 3.5: Cartoon of the BCS-like composite fermion pairing that leads to the energy gap of the 5/2 state.

The energy gap of the 5/2 state has been numerically calculated from exact diagonalization of few-electron systems and extrapolation to infinite systems as $1/N \to 0$ [57–62]. The maximum number of electrons numerically tractable in this way is today $N = 20$ electrons [62], which yields a gap of $\Delta_{5/2} = 0.036 \times e^2/4\pi\varepsilon\varepsilon_0 l_B$. A recent density-matrix renormalization group study [63] has found a similar value of $0.03 \times e^2/4\pi\varepsilon\varepsilon_0 l_B$.

The energy gap of the 5/2 state should, in an ideal 2D system, scale with the square root of the electron density (see section 3.2.1). In a real 2DES the gap is modified by the finite width of the wavefunction in the quantum well, LL mixing and disorder. In this thesis we measured the density dependence of the 5/2 energy gap. The results are described in chapter 6.

3.3.2 Topological quantum computation and 5/2

Particular interest is attributed to the 5/2 state because its excitations are suggested to be non-Abelian anyons and could be used for topological quantum computation.

Anyons

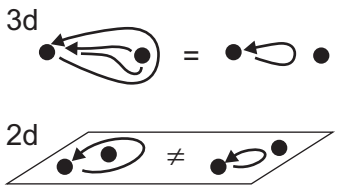

Ordinary particles are classified in bosons and fermions according to the behavior of the wavefunction under particle exchange. Microscopic particles are fundamentally indistinguishable. Exchanging two particles therefore can modify the joint wavefunction only by a phase factor, which has no experimental consequences. In three-dimensional space this phase is further restricted: As illus-

trated on the right a double exchange of the positions of two particles (which is the same as taking one particle in a loop around the other) is topologically equivalent to not exchanging them at all and thus no phase change is allowed. A single exchange therefore produces a phase of either zero or π. Particles belonging to the first group are called bosons, the second group is called fermions. A result from quantum field theory relates the exchange statistics to the spin of the particles: Bosons have integer spin, fermions have half-integer spin.

In two dimensions there is no reason for this phase restriction: A double exchange is not topologically equivalent to no exchange. Upon a single exchange the wavefunction can pick up any phase. Hence, the name anyons. The quantum Hall effect occurs in 2D systems and anyons can therefore be expected. The elementary excitations of the $\nu = 1/3$ state have an exchange phase of $\phi = \pi/3$ [64].

Non-Abelian particles

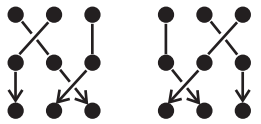

A group (in its mathematical sense, but here also an ordinary group of particles) is called *Abelian* or *commutative* if the order in which operations are performed is not important. The sketch shows two ways of braiding three indistinguishable particles. Suppose exchanging two of them multiplies the entire state with a certain phase factor. Successive interchanges will multiply the state by the sum of the phases. As $\phi_1 + \phi_2 = \phi_2 + \phi_1$ the order of exchanges does not matter for the final result. Phase factors are therefore an Abelian representation of the braid group.

If there is more than one wavefunction describing a certain number of particles at fixed positions and if this set of $g > 1$ states is degenerate in energy, then exchanging particle 1 particle 2 may do more than just introducing a phase [65]. Instead, it may take the system to another one of the degenerate states, as described by the multiplication $\Psi_a = M_{ab}^{12}\Psi_b$ with a unitary matrix. The same holds for exchanging particles 2 and 3 with a different matrix:

$$1 \leftrightarrow 2: \qquad \Psi_a = M_{ab}^{12}\Psi_b$$

$$2 \leftrightarrow 3: \qquad \widetilde{\Psi}_a = M_{ab}^{23}\Psi_b$$

If the matrices do not commute, $M_{ab}^{12}M_{ab}^{23} \neq M_{ab}^{23}M_{ab}^{12}$, then the final state depends on the order of the operations and the particles are said to obey non-Abelian statistics.

Topological quantum computation

Non-Abelian statistics of particles can be used to perform logical operations by winding particles around each other [64–67]. This type of quantum computation is called topological because the operations are immune to decoherence from the environment and just depend on robust quantities like the number (and order) of windings of certain particles around others. This is only true for absolute zero temperature, but corrections are exponentially small, namely of order $e^{-\Delta/T}$ where Δ is the energy gap protecting the degenerate ground state [64]. The larger this energy gap is, the better the error rate gets for a given temperature. Hence the interest in the energy gap of the 5/2 state investigated in this thesis.

The FQHE state at filling factor 5/2 is believed to support topological quantum computation. This is because the proposed Moore-Read wavefunction (the Pfaffian state) has non-Abelian excitations (see [68] for a pedagogical review). In fact, "the only such topological states thought to have been found in nature are fractional quantum Hall states, most prominently the $\nu = 5/2$ state" [66].

Assuming that the 5/2 state is indeed described by the Pfaffian and therefore in principle supports topological quantum computation, it is a difficult task how these ideas could be put into practice. Even though there might be other possibilities [69, 70], the most frequently cited proposal uses a transport experiment setup: A Hall bar with quantum points contacts where the tunneling probability of quasiparticles from one edge to the other can be controlled [65, 71–74]. Experiments are undertaken in this direction [75–77] but remain very challenging.

3.3.3 Is 5/2 realized as the Pfaffian state?

It is not yet experimentally clarified if the 5/2 state is a physical realization of the Pfaffian wavefunction and thus could enable topological quantum computation, but no disproof has yet been found. In fact it has passed a test: According to the Moore-Read theory the charge of the elementary excitations should be $e/4$. This is in fact what has been found [76, 78, 79], even though some details need clarification. This finding, however, does not disprove other proposed wavefunctions that predict the same quasiparticle charge but no non-Abelian statistics.

As next crucial test the Pfaffian predicts a fully spin-polarized state. Early tilted magnetic field experiments found a weakening of the 5/2 state with increasing tilt angle and were interpreted as indicating an unpolarized state with spin-flip excitations [80, 81]. An unpolarized singlet wavefunction was proposed [82]. The Pfaffian wavefunction seemed not to be consistent with interpreting the data as an unpolarized state. However, this interpretation was

challenged on the ground of numerical studies [60] which suggested that the tilt-induced weakening is due to the 5/2 states sensitivity to interactions, which are modified by the in-plane magnetic field. These numerical studies published in 1998 pointed towards a spin-polarized state even for vanishing Zeeman energy [61].

A recent analysis [83] of the experiments performed up to today interprets the data as suggesting an unpolarized state. The main reason for this conclusion is that the energy gap does not increase with electron density as expected for a polarized state. However, this is mainly based on data from two publications, one covering a wide density range but with a poorly developed 5/2 state [84], and a second publication using a sample with fixed density where the second subband was partially occupied [85]. We thus believe that the evidence is not unambiguous. Also an optical approach to detecting the spin polarization of 5/2 claims consistency with an unpolarized state [86]. Latest NMR experiments, unpublished at the time of writing, point towards full polarization.

Today, the issue of the spin-polarization is still unsolved. Experiments to identify the spin polarization of the 5/2 state are also ongoing in our research group.

Chapter 4

Microwave induced resistance oscillations (MIRO)

The phenomenon of microwave induced resistance oscillations (MIRO) is presented in Fig. 4.1. When a 2DES of high purity is cooled to low temperatures the longitudinal resistance shows Shubnikov-de-Haas oscillations in a weak magnetic field. Irradiating the sample with microwaves suppresses the SdH oscillations and gives rise to a new type of oscillations that can exhibit vanishing longitudinal resistance in finite $B-$intervals. In contrast to the QHE the Hall resistance (not shown) is essentially unaffected.

MIRO are governed by the ratio of two energies: The photon energy of the microwave radiation with frequency f

$$E_{\rm ph} = hf \tag{4.1}$$
$$E_{\rm ph}[\mu{\rm eV}] = 4.14 \times f[{\rm GHz}] \tag{4.2}$$

and the separation of LL which is the cyclotron energy $E_c = \hbar\omega_c$ (see equation 3.4). In the following the microwave frequency f will be expressed by the angular frequency ω. The ratio of the involved energy scales then is $E_{\rm ph}/E_c = \omega/\omega_c$.

Resistance minima are observed when the photon energy is a multiple of the LL separation:

$$\omega = (i + \phi_i)\omega_c, \quad i = 1, 2, 3, \ldots \tag{4.3}$$

with a phase shift ϕ_i (see below). A change at the cyclotron resonance $\omega = \omega_c$ is expected, but the multiples are surprising because for the optical transition matrix element between LLs j and j' one has (E is here the electric field):

$$< j|Ex|j' >= 0 \quad \text{for} \quad j' \neq j \pm 1. \tag{4.4}$$

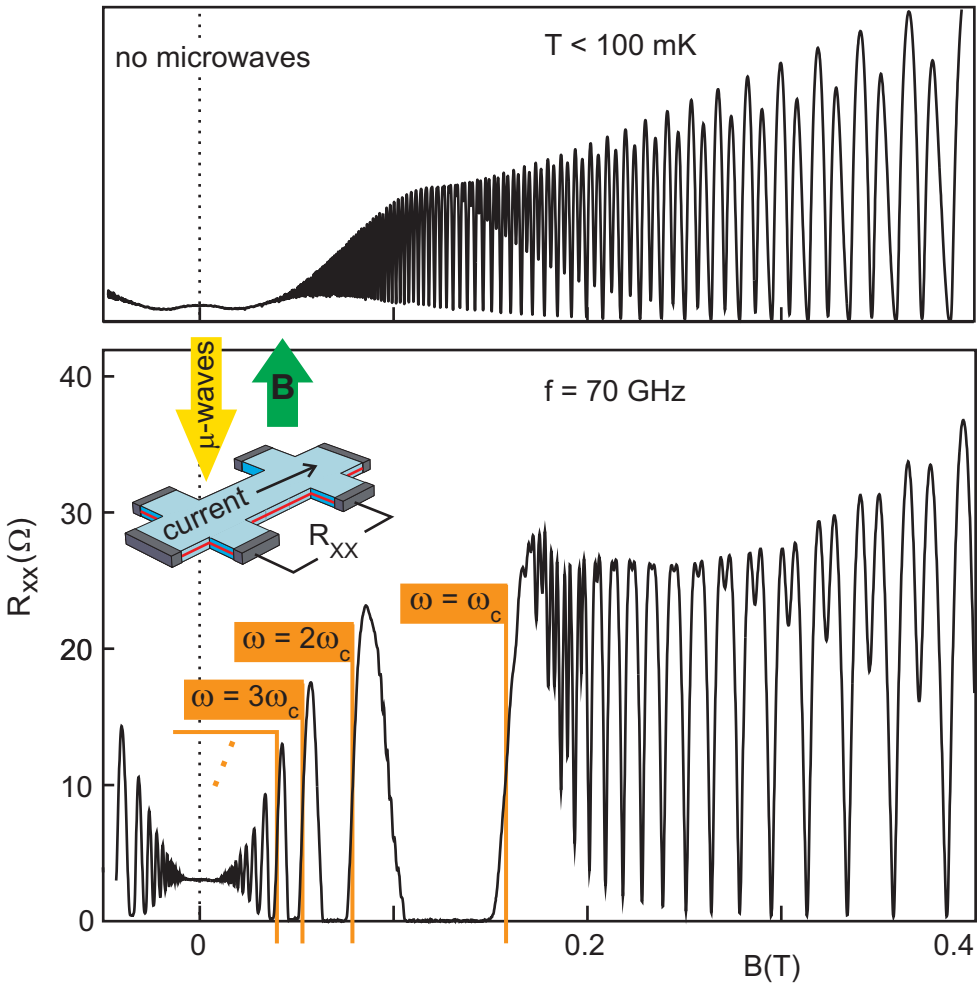

FIGURE 4.1: SdH oscillations (top) are replaced by a new type of oscillations when a 2DES is irradiated with microwaves (bottom). These are governed by the ratio of the microwave and cyclotron frequencies.

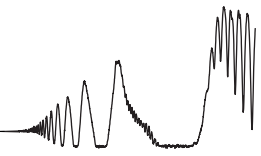

This was pointed out in the first publication reporting $1/B$ periodic microwave induced resistance oscillations in 2001 [7]. Soon after, in 2002/03, finite intervals of vanishing R_{xx} were observed by two groups [8, 9], which triggered much experimental and theoretical work. In this chapter we will first review relevant experiments and then address theoretical approaches (both without claiming completeness).

A prediction has been made for the compressibility of a 2DES under microwave irradiation [10]. Microwave induced compressibility oscillations (MICRO) are expected, similar to the oscillations observed in transport. The main part of this thesis deals with measuring the compressibility (see chapter 7).

4.1 MIRO related experiments

4.1.1 Transport experiments

In most cases pronounced MIRO are observed only in ultra clean samples with mobilities exceeding 10×10^6 cm^2/Vs. However, a large mobility is only a prerequisite and does not guarantee pronounced MIRO. We will discuss this issue in 5.3.2.

Most MIRO experiments are performed in Hall bar geometry. In a study using a Corbino device, which short circuits the Hall voltage and gives direct access to the conductivity instead of the resistivity, microwave induced conductance oscillations were observed as expected from inverting the resistivity tensor [87]. Unless otherwise stated studies here use the Hall bar geometry.

Frequency dependence

All publications agree that resistance maxima and minima shift on the magnetic field axis proportionally to the microwave frequency: Positions of extrema depend on the ratio ω/ω_c of the microwave frequency and the cyclotron frequency. The onset of oscillations does not scale with frequency. Rather, for a given sample, it happens at approximately the same $B-$field value for all frequencies. This can be seen from various publications [8, 88] and is apparent in our own data, see Fig 7.13.

The phenomenon of MIRO is observed only in a finite frequency range. To our knowledge, the lowest reported $R_{xx} = 0$ has been seen at 9 GHz [88]. At high frequencies oscillations become less pronounced. Frequency quenching has been observed to set in at 150 GHz [89], but also at 250 GHz decent MIRO have still been seen [90]. In the far-infrared regime only minor resistance changes are detected [91].

Temperature dependence

It has been reported in the first publications on MIRO that the resistance in the R_{xx} minima shows activated behavior. The extracted energy gaps are considerably larger than the microwave photon energy (and therefore also than the cyclotron energy). Values are between 10 K [8] and 20 K [9] in the typical frequency range of $50 - 100$ GHz (85 GHz for [8] and 57 GHz for [9]) and a bit lower for smaller frequencies (6 K at 20 GHz [88]).

The $B-$dependent shape of the resistance oscillations has been fitted [92] to a toy model (see section 4.2.1). In this model the oscillation amplitude is related to a level broadening, which was found to have the same temperature dependence as the mobility broadening.

A quantum lifetime τ_q^{MIRO} was extracted from the resistance oscillation amplitude in [92] and [93] as customarily done for SdH oscillations. The authors of [93] find for the quantum lifetime a strong temperature dependence $e^{-\alpha T^2}$ with a magnetic field dependent α.

Period and phase

For the phase ϕ_i in $\omega = (i + \phi_i)\omega_c$ a value of $\phi_i = 1/4$ has been reported in [8] and a value of $1/2$ in [9]. A detailed study [94] reports a phase shift of $1/4$ for $i > 4$ and a linear increase in the phase for the main oscillations with $i < 4$. The phase can not easily be determined for those minima with a finite region of vanishing longitudinal resistance.

In-plane magnetic fields

The dependence of MIRO on in-plane magnetic fields is controversial: In [95] no or little effect of in-plane fields is reported up to a tilt angle of 80°. In [96] a strong suppression with in-plane field is seen.

Power dependence

Power dependence is a difficult issue because it is hard to measure the exact microwave power that arrives at the sample position. Furthermore the radiation field in the space where the sample is located can be very inhomogeneous and vary with frequency. We have observed strong inhomogeneities with the help of a single electron transistor (see section 7.3.1). This problem has been mentioned in [96] in connection with in-plane fields.

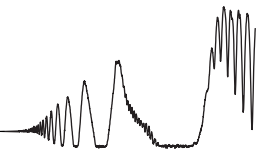

Fractional MIRO

Recently [97] fractional MIRO have been reported, i. e. microwave induced oscillations in longitudinal resistance in the regime $\omega < \omega_c$ where the photon energy is *less* than the cyclotron energy [98].

Plasmons

In Refs. [89,96] plasmons are observed together with MIRO. It is proposed that MIRO originate from plasmonic effects.

4.1.2 Absorption, reflection and polarization

Long before MIRO transport experiments, oscillations at microwave frequencies that are a multiple of the cyclotron frequency have been seen in absorption experiments [99]. This was done in a Si-inversion layer and at much higher frequencies ($\approx$ 900 GHz) than where MIRO is usually seen in transport. However, most later absorption and transmission experiments under MIRO conditions show a main peak at the cyclotron resonance and little or no additional oscillations at harmonics [89, 90, 92]. In a polarization dependent study [90] the transmitted power shows, as expected, a strong dip at the cyclotron resonance for one circular polarization direction while the dip is absent in the other. Linearly polarized radiation interpolates between the two.

Recently, also higher order oscillations in the absorption were measured [100]. Their polarization dependence is not yet investigated to our knowledge.

The polarization dependence of transport measurements was also investigated: MIRO are essentially insensitive to the polarization (linear or circular in different rotation directions) of the incident radiation [90]. This is surprising, because the polarization dependent Drude conductivity is an important ingredient in most theoretical approaches to MIRO.

4.1.3 Photovoltage and photocurrent

In usual transport measurements a fixed current is driven through the sample and the resistance is measured. In a different study, no current was applied [101]. Instead, the sample was illuminated with microwaves and spontaneously arising photocurrents and photovoltages were detected. For both, the same overall pattern was seen as in transport experiments. Furthermore, photovoltages between two contacts on the sample perimeter were found to be about two orders of magnitude smaller than between one external and one internal contact. The importance of built-in electric fields near contacts was stressed [102].

4.1.4 Hall induced resistance oscillations

Resistance oscillations are also observed in the absence of microwave radiation as a consequence of Hall-tilted LLs. These are governed by the commensurability of the cyclotron diameter $2R_c$ and the spatial separation of two tilted LLs crossing the same energy [103]. Here, the relevant parameter is ω_H/ω_c with $\hbar\omega_H \approx 2R_c eE$ the energy drop in a tilted LL across the cyclotron diameter. The Hall-tilt originates from a dc current driven through the sample. Under additional microwave irradiation MIRO minima develop into maxima with increasing current, i. e. increasing Hall tilt [104–106].

4.2 Theoretical approaches to MIRO

The general idea how microwave induced resistance oscillations and especially microwave induced vanishing resistance emerges is as follows:

$$\textit{negative conductivity mechanism} + \textit{instability} \;\rightsquigarrow\; R_{xx} = 0$$

Several microscopic mechanisms that produce an oscillatory contribution to the conductivity have been proposed:

- Photon assisted impurity scattering with spatial displacement [107–110]
- Non-equilibrium distribution function [10, 111–115]
- Photon assisted phonon scattering [116–118]
- Semiclassical mechanisms, including non-parabolicity effects [119], perturbative treatment of scattering [120], edge channels stabilization [121] and synchronization [122]

The first two mechanisms are the most cited and are reviewed in this section. Then we address the instability mechanism and emergence of vanishing resistance.

4.2.1 Photon assisted impurity scattering and toy model

When the absorption of a photon is accompanied by scattering from disorder the selection rule 4.4 can be violated. In [107] such a mechanism is introduced as spatial displacement upon scattering, see left panel in Fig. 4.2: An electron

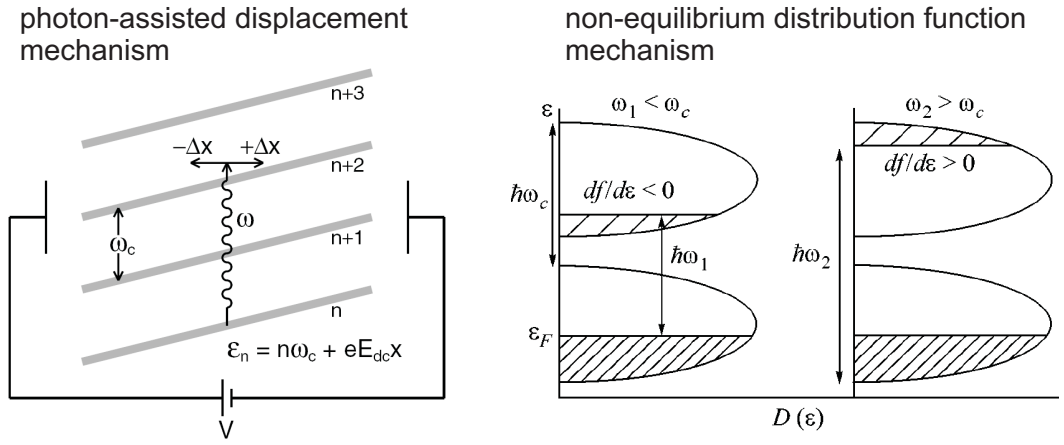

FIGURE 4.2: Left: (from [107]) Absorption of a photon accompanied by impurity assisted spacial displacement. Right: (from [112]) Photon absorption establishes a non-equilibrium distribution function (NEDF).

absorbs a microwave photon and is excited. It then scatters from an impurity and is spatially displaced. LLs are tilted by an electric field from the current driven through the sample. If the spatial shift is such that the final state is centered in a LL the transition probability is large. Depending on the ratio of ω and ω_c electrons are preferentially transferred uphill or downhill leading to a decrease or increase in resistance, respectively.

Before calculating the transition matrix elements the authors introduce a toy model that yields the shape of the waveform of the resistance change under microwave irradiation.[1] In the toy model (see [107] and also [89, 92] for examples) the change in resistance is

$$\Delta\rho_{xx} = A \int dE\ \mathrm{DOS}(E)\partial_E \mathrm{DOS}(E+\hbar\omega)[f(E) - f(E+\hbar\omega)] \tag{4.5}$$

where $\mathrm{DOS}(E) = \Sigma(eB/\pi^2\hbar\Gamma)/(1+(E-E_j)^2/\Gamma^2)$ is the density of states with the LL energies $E_j = (j+1/2)\hbar\omega_c$ and the LL broadening Γ, $f(E)$ is the Fermi distribution function and A an amplitude factor.

This toy model can be used to fit experimental data. The fitting parameters are the amplitude factor A and the LL width Γ. The former has no meaning as it is not specified in the model. The LL broadening, however, can be compared to estimates for the LL width from different effects. This was done in [92] and [89]. In the latter reference the extracted broadening was found to increase with microwave frequency. This is partly attributed to plasmon excitations and

[1] We note that the shape of the resistance change has also been fitted phenomenologically by $\Delta R_{xx} = -A\exp(-\lambda B)\sin(2\pi f/B)$ with a damping parameter λ and an amplitude A [123].

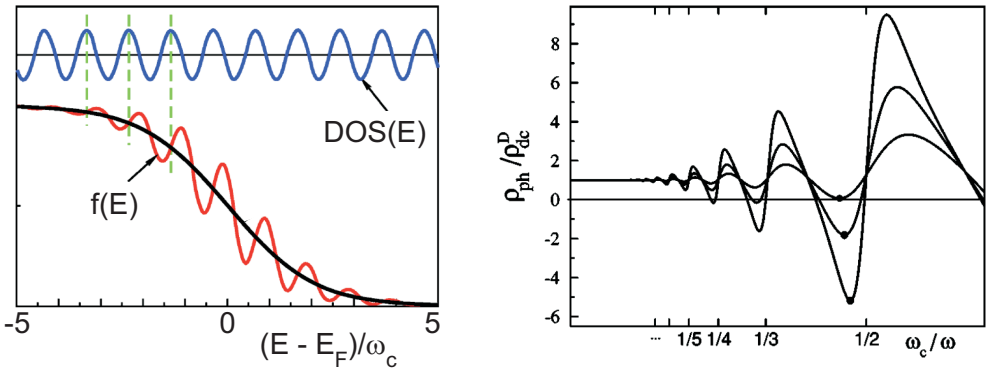

FIGURE 4.3: (from [113]) Left: Oscillatory DOS and oscillatory NEDF. Right: Photoresistivity under microwave irradiation for different microwave powers.

could explain the observed quenching of MIRO at high frequencies.

The idea of the photon assisted impurity scattering mechanism was further developed in subsequent publications [108–110].

4.2.2 Non-equilibrium distribution function and compressibility

The idea that microwave radiation could establish an electronic non-equilibrium distribution function (NEDF) was introduced in [112]. Depending on the ratio ω/ω_c the absorption of photons in combination with broadened LLs can lead to a distribution function with a positive or negative derivative with respect to energy at its upper end (see right panel in Fig. 4.2). This derivative appears in the conductivity that was calculated from a previously established expression in Ref. [39]. The magnetoresistance exhibits oscillations and can become negative. Even though the shape of the R_{xx} oscillations is not reproduced in this simple model the results agree qualitatively with experiments.

The model of the NEDF was further developed in [111, 113]. The distribution function is calculated as a stationary solution of a kinetic equation taking into account the effects of microwave photon absorption and emission, of impurity scattering leading to energy diffusion, and of inelastic relaxation. As a main source of inelastic relaxation the authors find electron-electron interactions. This type of scattering conserves the total energy of the electronic system but can nevertheless smear the oscillatory, non-equilibrium part of the distribution function.

The normalized DOS in a weak magnetic field when LL are not fully sepa-

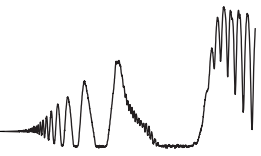

rated (see section 3.2) is approximated by an oscillatory function

$$\widetilde{\mathrm{DOS}}(E) = 1 - 2\delta \cos\frac{2\pi E}{\omega_c}, \quad \delta = \exp(-\frac{\pi}{\omega_c \tau_q}) \tag{4.6}$$

where δ measures the strength of the oscillations in the DOS. The oscillatory DOS leads to the establishment of a NEDF. Both are illustrated in the left panel of Fig 4.3.

The leading contribution to the photoconductivity comes from a product of the oscillatory DOS and the oscillatory NEDF that survives energy averaging. The resulting photoresistivity (see right panel of Fig. 4.3) shows oscillations and can become negative for sufficiently high microwave powers.

Under equilibrium conditions the Einstein relation between the conductivity and the diffusion states that currents arise from gradients in electrochemical potential, which is the sum of the chemical and electrostatic potential (see section 7.1.3). The nature of the perturbation (electrostatic or chemical potential) is irrelevant. Under microwave induced non-equilibrium conditions the Einstein relation does not hold any more and extra terms in the current arise [102]. This is important in inhomogeneous systems, for example near contacts [101, 102] and likely also in our compressibility measurements done with a local probe. We will come back to this in section 7.4.

Compressibility of a 2DES under microwave irradiation

In the above framework of the NEDF a prediction was made for the compressibility $\chi(q)$ (see equation 2.5) of a 2DES under microwave irradiation [10]: It shows microwave induced compressibility oscillations (that we name MICRO in this work) qualitatively similar to the oscillations in the longitudinal resistance. The exact result depends on the inelastic scattering length l_{in} and the wavevector q of a local perturbation. Figure 4.4 shows the result for $ql_{in} \gg 1$. For smaller q the result changes quantitatively but not qualitatively.

In this thesis we measure the compressibility of a 2DES under microwave irradiation. We will discuss the results in chapter 7. Oscillations are observed. However, we find that the sign of the microwave induced change of the compressibility is reversed compared to the above prediction.

4.2.3 Emergence of zero-resistance states

We mentioned above that microwave induced zero-resistance states are believed to emerge from a combination of a microscopic mechanism for negative conduc-

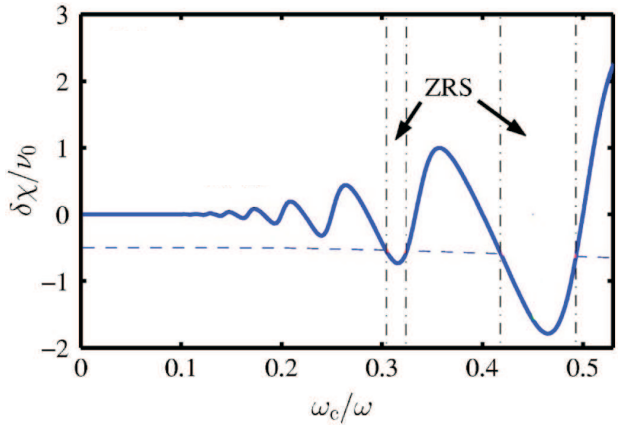

FIGURE 4.4: (from [10]) The compressibility of a 2DES under microwave irradiation shows $1/B$ periodic oscillations. Between vertical lines zero resistance states (ZRS) are expected in a transport measurement.

tivity and an instability which fixes the experimentally observed resistance to zero [124]. The instability mechanism is independent of the mechanism responsible for the negative conductivity.

According to [124] it can be readily understood why microwave induced negative conductivity is not stable. Negative conductivity means that a random current fluctuation leads to an electric field that enhances this current instead of damping it. When the current gets sufficiently large, however, the microwave radiation is only a small perturbation and the dark current situation has to be restored. The resistivity as a function of current density has to cross over to a positive value at some critical current density $|\mathbf{j}_0|$ as illustrated on the left of Fig. 4.5. A positive resistivity dampens a further current increase. Only the current density $|\mathbf{j}_0|$ is therefore a stable state.

As the stable current density corresponds to vanishing electric field the current flows dissipationless and no voltage drop occurs along the sample. Therefore a 4-point measurement detects vanishing longitudinal resistance.

To maintain the current that is imposed, the formation of domains is proposed. In each domain the current may flow in different directions but with the same critical current density $|\mathbf{j}_0|$. The influence of disorder on the domain formation [125] and time dependent phenomena have been studied theoretically [126] and experimentally [127].

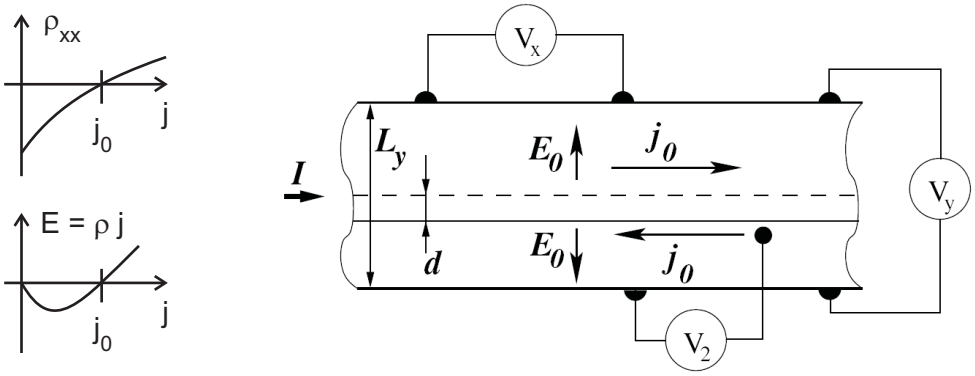

FIGURE 4.5: Left: The negative resistivity shows a crossover from negative to positive values at a critical current density. This density acts as a stable fixed point. Right: (from [124]) Domain formation with the critical current density in each domain.

Part II

Experiments and discussion

Chapter 5

Finding suitable heterostructures

In this thesis we investigate two different aspects of the physics of 2DES. First, the electron density dependence of the FQHE at filling factor 5/2. Second, on a 2DES that exhibits microwave induced resistance oscillations (MIRO) we look for microwave induced compressibility oscillations (MICRO). Heterostructures matching the specific requirements of these experiments are needed. In this chapter we investigate the correlation of characteristic 2DES parameters with the pronouncedness of the 5/2 state and MIRO. Then we give details on the wafers used for the experiments presented in the next two chapters.

5.1 Relevance of 2DES quality indicators

The 5/2 state and MIRO are observed only in todays "best" GaAs/AlGaAs heterostructures. Yet, what does "best" mean? More specifically, are there characteristic parameters for heterostructures that correlate with the pronouncedness of the 5/2 state or MIRO? This question is of double relevance: From a theoretical point of view, identifying the relevant parameters gives insight in the physics of the observed effects and the physics of disorder in 2DES. From a practical point of view, directly measuring the 5/2 state and MIRO is time consuming and not trivial: 5/2 is only observed at ultra low temperatures in a dilution refrigerator and MIRO requires a sample holder with an incorporated waveguide. Finding more easily accessible parameters that *indicate* a pronounced 5/2 state or MIRO would facilitate and speed up the identification of suitable wafers as well as the iterative improvement of wafers by epitaxial growers.

In this chapter we report on the quest for parameters correlated with the 5/2 state and MIRO. We could successfully identify excellent wafers for 5/2 and

reasonably good wafers for compressibility measurements under MIRO conditions. Both experiments could be successfully performed and the results are presented in the next two chapters. Yet, the search for indicating parameters was only partly successful for 5/2 and quite unsuccessful for MIRO. Here our results mainly indicate what claims can *not* be made. Especially for the electron mobility, the most widely used quality number of a 2DES, a large value is only a prerequisite, not an indicator for pronounced 5/2 and MIRO.

5.2 Sample requirements for our experiments

We here list the sample requirements for the two types of experiments in this work.

5/2 density dependence	MICRO
pronounced 5/2 state	pronounced MIRO
tunable density (large range)	tunable density (small range)
single side doping	single side doping
	no overdoping (for surface SETs)

Table 5.1: Sample requirements for this thesis' experiments.

Essential for both types of experiments is the ability to tune the electron density during measurements.[1] This is done by applying a voltage to a backgate (BG), namely a conducting layer parallel to the 2DES. This essentially limits doping to one side of the quantum well (QW) in order to prevent screening of the applied voltage.[2] The 5/2 state should be investigated in a density interval as large as possible ($1 \times 10^{11}/\mathrm{cm}^2$, as an order of magnitude). To achieve this with reasonable voltages requires an MBE grown, in-situ backgate close to the 2DES. For the compressibility measurements under MIRO conditions much smaller density variations are sufficient ($1 \times 10^8/\mathrm{cm}^2$, as an order of magnitude). This can be done by a BG at a greater distance from the 2DES, for example the surface of the chipcarrier that the sample is mounted on. This introduces a number of problems as we will describe in section 7.3.2. However, due to sample limitations we had to adopt this approach for our MICRO measurements.

[1] The density can in principle be changed using the persistent photoconductivity effect by illumination at low temperature (see section 2.3.2). For our goals, however this can not be used: The 5/2 study should be made for one given disorder potential. Illumination changes the density together with the disorder from ionized donors. The MICRO studies require an $ac-$modulation of the density and thus require reversibility.

[2] Introducing only little doping between QW and BG is in principle possible but not easy to reliably do in practice.

5.3 Results on quality indicators

In search of 2DES parameters indicating a pronounced 5/2 state and MIRO we tested about 20 heterostructures. We performed 4 point measurements of R_{xx} and R_{xy} on etched Hall bars of 400 μm width in an Oxford dilution refrigerator. For the 5/2 measurements a sample holder with specially designed silver sinter filters and thermocoax cables to thermalize electrons at low temperatures was used. The MIRO measurements were done with a different sampleholder equipped with a microwave waveguide as described in section 7.1.1. We measured the parameters electron density, electron mobility and quantum lifetime. The heterostructure design parameters are supplied by the growers. We refer to chapter 2 where the relevant design parameters and figures of merit are introduced. For the amount of doping a value of 100% corresponds to the point where the density saturates and electrons start accumulating also in the doping layer.

	FQHE, esp. 5/2	MIRO
density n	strong	weak
mobility μ	weak	none
quantum lifetime τ_q	none	none
spacer thickness	unclear	unclear
overdoping and Al%	weak	unclear
	No correlation between 5/2 and MIRO	

TABLE 5.2: Correlation of sample parameters with the pronouncedness of the 5/2 state and MIRO. See text for details and examples. Al% means the aluminum content of the AlGaAs in the doping region.

In table 5.2 we list to what extent sample parameters can be used to predict the pronouncedness of the 5/2 state and MIRO. We emphasize that we only investigated a limited number of wafers and that all of these were excellent in terms of mobility ($\mu > 8 \times 10^6$ cm^2/Vs). In the following two subsections we give details on table 5.2.

5.3.1 Correlation of 2DES parameters and $\nu = 5/2$

The pronouncedness of the $\nu = 5/2$ state is quantified by the activation gap $\Delta_{5/2}$ as measured from the temperature dependence of R_{xx} (we will give details in section 6.1.2). Figure 5.1 shows the activation gap $\Delta_{5/2}$ for our own data (black dots) and various values from the literature. The $x-$axis indicates the electron densities of the samples. Next to each data point we display the mobilities and

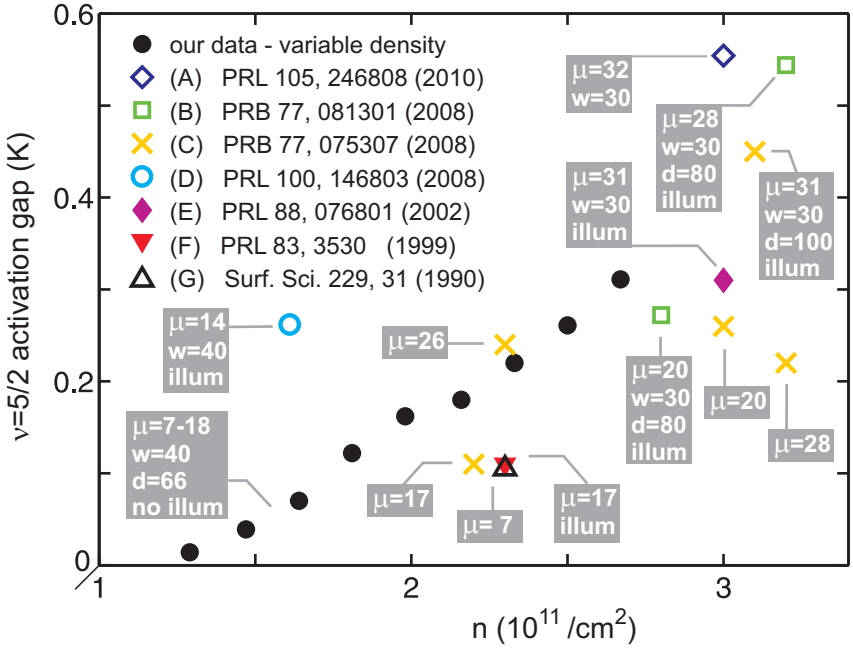

FIGURE 5.1: This page: comparison of our measured 5/2 activation gaps to literature values. Mobilities μ are given in units of 10^6 cm^2/Vs. The width of the QW w and the spacer thickness are in nanometers, if they are known. "illum" indicates that the samples were illuminated before measurement. (Publications are labeled with letters for easier reference in the main text.) Apparently, there is little correlation between mobility and the 5/2 energy gap $\Delta_{5/2}$.

Right page: Pronouncedness of MIRO for several wafers. Points indicate the wafers' electron density and spacer thickness. Other parameters (if determined) are given next to each graph. Graphs show R_{xx} in arbitrary units on a $B = 0 - 230$ mT axis. For backgated samples several densities are shown in colors. Microwave powers are chosen sufficiently high to reach saturation in MIRO amplitude. We find only little correlation between the pronouncedness of MIRO and the investigated parameters. See text for details.

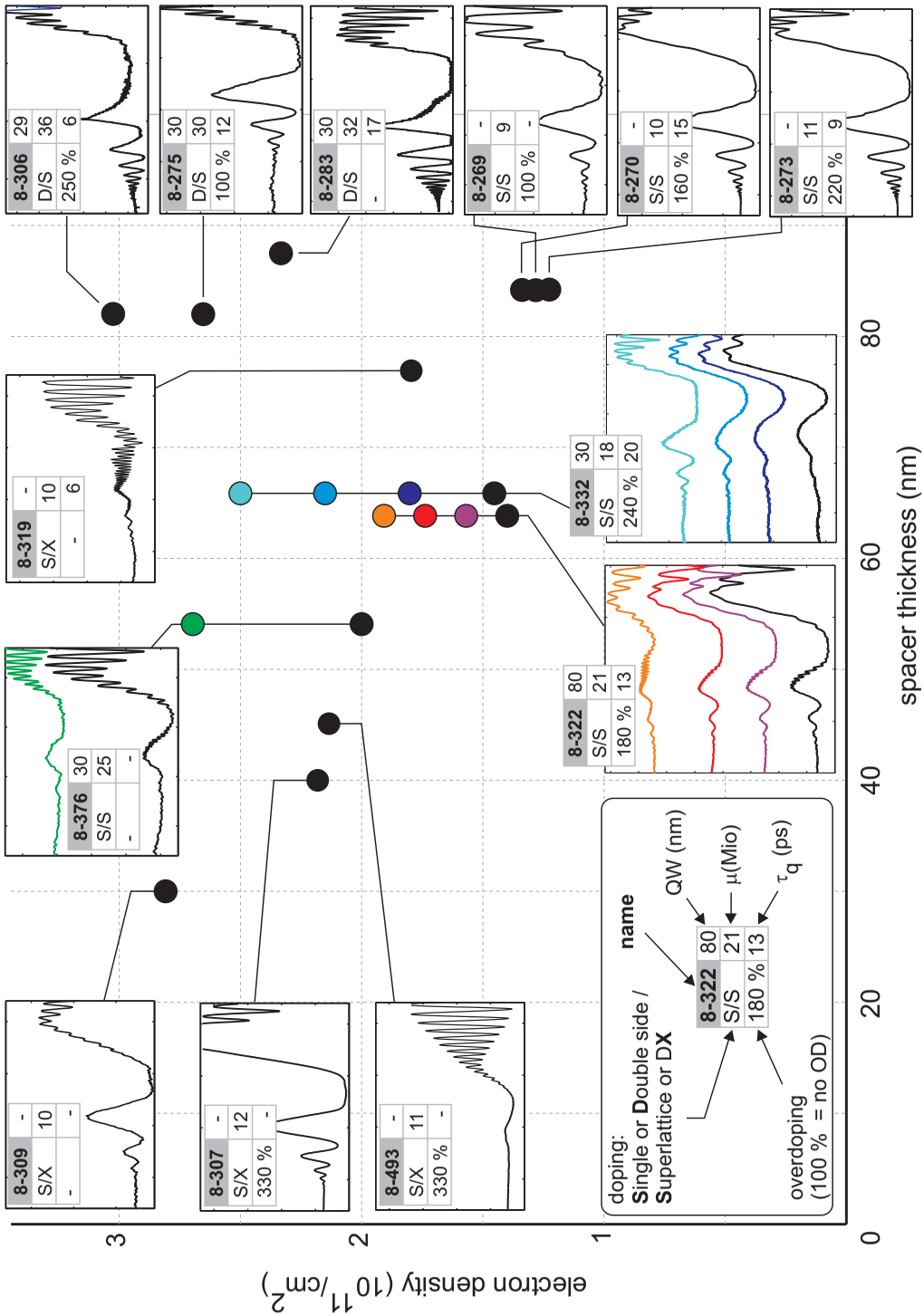
electron density (10^{11}/cm^2)
spacer thickness (nm)
0
20
40
60
80
1
2
3
8-309 - 10 - S/X - -
8-307 - 12 - S/X 330 % -
8-493 - 11 - S/X 330 % -
8-376 30 25 - S/S - -
8-319 - 10 6 S/X - -
8-322 80 21 13 S/S 180 % 13
8-332 30 18 20 S/S 240 % 20
8-306 29 36 6 D/S 250 % 6
8-275 30 30 12 D/S 100 % 12
8-283 30 32 17 D/S - -
8-269 - 9 - S/S 100 % -
8-270 - 10 15 S/S 160 % 15
8-273 - 11 9 S/S 220 % 9
doping:
Single or Double side /
Superlattice or DX
name
QW (nm)
μ(Mio)
τ_q (ps)
8-322 80 21 13 S/S 180 % 13
overdoping
(100 % = no OD)

other parameters if they are known. We now give details on the correlation between $\Delta_{5/2}$ and 2DES parameters:

Electron density: The 5/2 gap increases with electron density. This is apparent especially in our data which are all taken on the same sample and thus for the same bare disorder potential. This is expected, as all FQHE energy scales depend on the density (see section 3.2.1). We compare our data to theory in section 6.2.

Electron mobility: Only little correlation is observed with $\Delta_{5/2}$. Some examples illustrate the large scatter in the data in Fig. 5.1: First, compare our highest n data point with the result from (E). Density and mobility are considerably lower in our sample, however the measured gaps are similar. Then, comparing two $\mu = 28 \times 10^6$ cm^2/Vs samples from (B) and (C) having the same density, the gap differs by more than a factor of two. Probably the most striking example in this context is (D) and the $\mu = 28 \times 10^6$cm^2/Vs sample from (C): Density *and* mobility are increased by a factor of two for the latter, however, the activation gap is smaller. Also, apart from the published data, many very high mobility wafers show a weaker 5/2 state. Even though a high mobility seems to be a prerequisite these examples illustrate that μ is a poor figure of merit to predict the quality of the $\nu = 5/2$ state.

Quantum lifetime: In Ref. [13] (which partly relies on our measurements) it is shown that the 5/2 state can vary considerably while the quantum lifetime stays constant. Also, we have measured comparable 5/2 states on samples with very different τ_q (not shown).

Spacer thickness: The relevance of the spacer thickness for the 5/2 state remains unclear due to insufficient statistics. However, in section 6.2 we give theoretical evidence that a large spacer might be important.

Overdoping and Al%: An influence of overdoping on the 5/2 state is reported in Ref. [13]. From our own data we have not enough statistics to identify a clear trend. A very recent study [16] corroborates a certain importance of overdoping. There, also the Al content in the doping region was systematically investigated. The 5/2 state benefits from low Al content due to enhanced screening capability of the electrons remaining in the donor layer.

5.3.2 Correlation of 2DES parameters and MIRO

The pronouncedness of MIRO is quantified by the observed number of oscillations and/or number of regions of vanishing R_{xx}.[3] On the right page of Fig. 5.1 we give an overview of many wafers tested for MIRO. A typical MIRO trace is given for each sample together with additional experimental and design parameters. For wafers with a BG, data for several densities are shown.

Electron density: A weak trend can be observed that increasing electron density strengthens MIRO. However, for example the high density wafer 8-376 shows very poor MIRO.

Electron mobility: No correlation is seen between mobility and MIRO. Very high mobility wafers like 8-376 and 8-275 show poor MIRO. As for 5/2, a high mobility seems to be a prerequisite for pronounced MIRO, but not a sufficient condition. We note that all measured wafers are excellent in terms of mobility.[4]

Quantum lifetime: No correlation is observed with τ_q. However, statistics is limited as we did not determine τ_q for all wafers.

Spacer thickness: There seems to be a trend for better MIRO when the spacer thickness is large. Yet, to our surprise wafer 8-307 shows good MIRO even though the spacer is one of the thinnest that we measured.

Overdoping: Overdoping seems to play a certain role: Wafers 8-269, 8-270 and 8-273 are identical except for the amount of doping. Also, of the two similar wafers 8-275 and 8-306 the one with higher doping shows better MIRO. Yet, other highly overdoped samples like 8-332 show poor MIRO.

In summary, in spite of extensive testing we were not able to identify 2DES parameters that correlate convincingly with the pronouncedness of MIRO. We estimate that the most promising candidates are the spacer thickness and the overdoping level. We mention some other observations:

[3] Similar microwave powers and frequencies have to be used. The power near the sample is a difficult issue in our setup as it varies with frequency and position (see section 7.3.1). However, for large powers a saturation of the oscillation amplitudes is observed. We give traces for powers close to or above this value such that a further increase does not show more oscillations.

[4] In the literature pronounced MIRO (approaching vanishing R_{xx}) are mostly observed when mobilities exceed 10×10^6 cm^2/Vs. The only exception, to our knowledge, is a sample with a mobility of 0.56×10^6 cm^2/Vs and a very large density of 8.5×10^{11}/cm^2 [128].

- No wafer with an in-situ grown BG showed good MIRO. This hampers our compressibility experiments where density tunability is needed. We use the chip carrier as a BG instead.
- Other heterostructure parameters not listed here were partly investigated but also seem unrelated to MIRO. Especially the ratio τ/τ_q, the doping scheme (using DX-center or miniwell doping), and the 2DES layout (placing the 2DES in a QW or at a single heterojunction) have no clear effect on MIRO.
- There is no correlation between MIRO and the 5/2 state. Especially, the backgated sample 8-332 shows an excellent 5/2 state and was used for the measurements presented in chapter 6 . Also 8-319 shows a pronounced 5/2 but poor MIRO.
- The wafer 8-493 is an identical copy of 8-307, except for the spacer and the fact that it was grown two years later. Surprisingly, MIRO is nearly absent. This indicates that some aspect not considered here might be the limiting factor for MIRO.

5.4 Heterostructures used in this thesis

Here we give details on the wafers used for the two types of experiments in this thesis.

5.4.1 Heterostructure used for 5/2 experiments

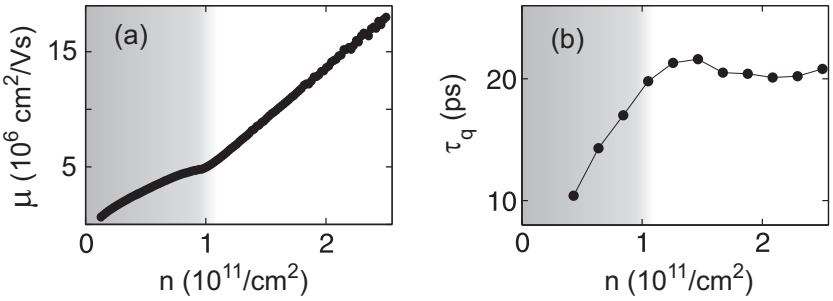

FIGURE 5.2: Characteristic properties of our sample as a function of the electron density n. (a) Electron mobility. (b) Quantum lifetime extracted from Shubnikov-de-Haas oscillations.

For the 5/2 experiments presented in chapter 6 we use wafer 8-332. It has an in-situ grown n^+-GaAs layer that serves as a backgate (BG) to tune the electron

density. The two-dimensional electron system (2DES) resides in a 30 nm wide quantum well located 850 nm above the backgate. The well is modulation doped from the top side only using an overdoped short period AlAs/GaAs superlattice located 66 nm away from the 2DES. A homogeneously doped region closer to the surface compensates for surface depletion. We refer to section 2.3.2 for details on this doping scheme.

The BG allows to tune the electron density n from complete depletion up to approximately $2.7\times10^{11}/\mathrm{cm}^2$. Fig. 5.2 depicts the electron mobility μ and the quantum lifetime τ_q as a function of n. The mobility reaches a value of 18×10^6 cm^2/Vs at the highest density. Above $10^{11}/\mathrm{cm}^2$ the mobility grows linearly. At lower densities the behavior is qualitatively different. This change is also visible in the quantum lifetime τ_q extracted from Shubnikov-de-Haas oscillations at low magnetic fields where spin-splitting is not resolved yet. It has roughly a constant value of 20 ps above $n = 10^{11}/\mathrm{cm}^2$, but sharply drops below this density. Subsequent measurements of quantum Hall features are performed at $n > 1 \times 10^{11}/\mathrm{cm}^2$.

The linear dependence of the mobility in this regime indicates that μ is limited by background impurities in the GaAs channel [23]. Remote ionized impurities (RI) are expected to play only a minor role for the transport mobility for this spacer thickness. Also, they would cause μ to grow super-linearly as $n^{1.5}$. The quantum lifetime τ_q is 200 to 500 times shorter than the transport lifetime τ calculated from the mobility in the density range above $n = 10^{11}/\mathrm{cm}^2$. This indicates that the quantum lifetime is limited by scattering from RI instead of background impurities. These issues were described in section 2.5.

5.4.2 Heterostructure used for MIRO experiments

Our goal here was to find a wafer with an in-situ grown BG that shows pronounced MIRO. As can be seen from Fig. 5.1 no such wafer could be identified.

We have to use the chip carrier as a BG. We first tried to use wafers 8-270 and 8-273. These are single side doped, they allow to change the density by a sufficient amount and they show reasonably good MIRO. Unfortunately it turned out that single electron transistors (SET) needed to measure the compressibility can not be operated on such SPSL overdoped wafers: Coulomb blockade oscillations as a function of the applied 2DES voltage were noisy, hysteretic and exhibited erratic jumps (see section 7.1.3 for the physics of SETs).

We finally identified wafer 8-307 which fullfills all requirements: It is single side doped, not overdoped and shows reasonably good MIRO. This wafer has a spacer thickness of 40 nm, an electron density of $2.1 \times 10^{11}/\mathrm{cm}^2$, a mobility of 12×10^6 cm^2/Vs and the 2DES is located in a single heterojunction at a total

depth of 116 nm below the surface. Doping is provided not in a GaAs miniwell but in the AlGaAs and thus DX centers are formed.

Chapter 6

Density dependence of the $\nu = 5/2$ energy gap

The $\nu = 5/2$ FQHE state and its possible relevance for topological quantum computation were introduced in section 3.3. Here we exploit a density tunable heterostructure that exhibits an excellent 5/2 state. To our knowledge this is the only density dependent study of a fully quantized 5/2 state performed on one single sample and thus for one given bare disorder potential. We first present the experimental results. (We focus on the 5/2 state and refer to the published results [62] for more detail.) Then we give a detailed data analysis, comparison to theory and discussion.

6.1 Experimental results for $\Delta_{5/2}$

Studies are performed on a 400 μm wide Hall bar. Details on the used wafer were presented in section 5.4.1. We perform 4 point measurements with standard lockin techniques in an Oxford dilution cryostat with a base temperature of ≈ 15 mK.

6.1.1 Overview of the second LL

Figure 6.1(a) shows the behavior of the longitudinal and Hall resistance for different densities at $T = 15$ mK when the spin up branch of the second LL is partially occupied: $2 < \nu < 3$. The FQHE features improve considerably with increasing n. The $\nu = 5/2$ state (marked by arrows) is well resolved at $1.5 \times 10^{11}/\mathrm{cm}^2$, $\nu = 7/3$ is slightly weaker and $\nu = 8/3$ emerges at about $2 \times 10^{11}/\mathrm{cm}^2$. Weakest, but clearly visible at the highest accessible densities are the 11/5 and 14/5 states. Also reentrant integer quantum Hall effect behavior (RIQHE)

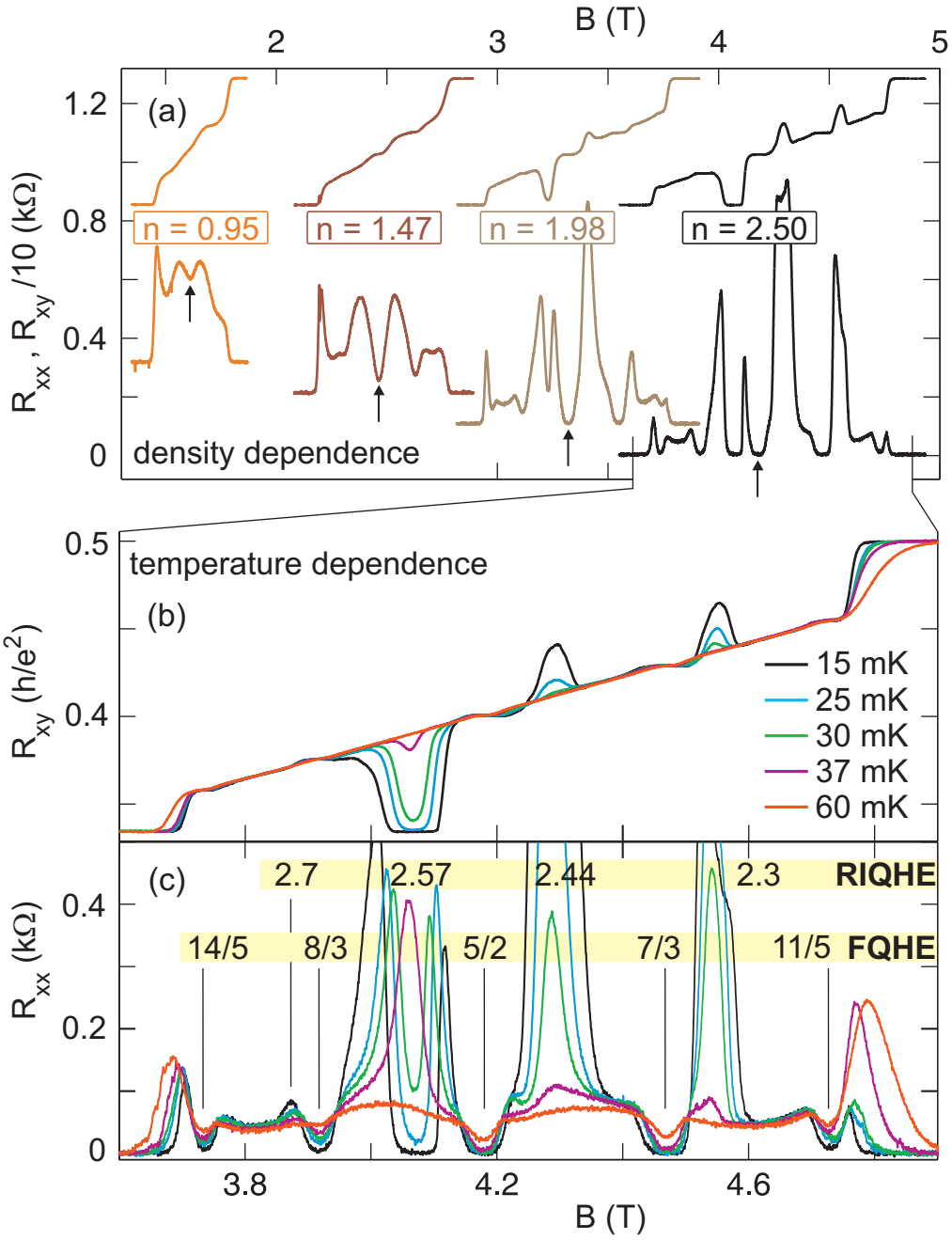

FIGURE 6.1: Evolution of the longitudinal and Hall resistances with density and temperature, shown between $\nu = 2$ and 3. (a) Density dependence of $R_{\rm xx}$ and $R_{\rm xy}$ (densities in units of $10^{11}/\mathrm{cm}^2$). All traces are taken at 15 mK. Filling 5/2 is marked by arrows. Other filling factors can be identified by comparing with panel (c). R_{xx}-traces are offset for clarity. (b) Temperature dependence of $R_{\rm xy}$ and (c) $R_{\rm xx}$ for $n = 2.5 \times 10^{11}/\mathrm{cm}^2$.

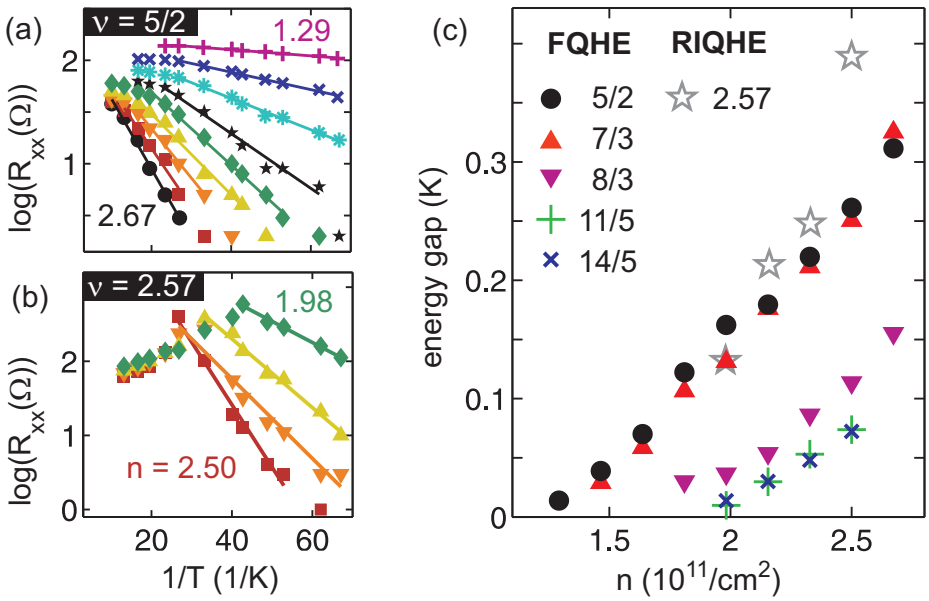

FIGURE 6.2: Arrhenius plots for (a) the 5/2-state and (b) the reentrant integer quantum Hall state at filling factor 2.57. Different symbols/colors correspond to different densities (all densities are given in units of $10^{11}/\mathrm{cm}^2$). Activation energies are calculated from linear fits in the activated regime. (c) Density dependence of the activation energies for the fractional quantum Hall states listed in the legend and for the $\nu = 2.57$ reentrant integer quantum Hall state.

is observed near fillings $\nu = 2.57, 2.44$ and 2.3. This reentrant behavior has been attributed to the formation of quantum liquid crystal phases from excess electrons or holes [129].[1]

6.1.2 Temperature dependence: Energy gap of the 5/2 state

Panels (b) and (c) of Fig. 6.2 show the temperature dependence of the transport quantities for a density of $2.5\times10^{11}/\mathrm{cm}^2$. 5/2 and other FQHE states strengthen considerably for lower temperatures. Energy gaps Δ are determined from the temperature-activated finite R_{xx} values in the minima using $R_{xx} \sim \exp(-\frac{\Delta}{2k_BT})$. Exemplary Arrhenius plots are displayed for filling 5/2 and various densities between $n = 1.29$ and $2.67 \times 10^{11}/\mathrm{cm}^2$ in Fig. 6.2(a). (The RIQHE at $\nu = 2.57$ also shows activated behavior, see [62].)

Energy gaps as a function of the electron density are shown in Fig. 3(c). Among the FQHE states 5/2 and 7/3 have the largest gaps. $\Delta_{5/2}$ reaches 310

[1] In the following we focus only on the 5/2 state and refer to [62] for details on other second LL filling factors observed in our data.

mK at the highest density. This is comparable, though less than the largest measured $\Delta_{5/2}$ to date (Ref. [54]: 558 mK, Ref. [130]: 544 mK, Ref. [53]: 450 mK, samples (A), (B) and (C) in Fig. 5.1).

It is an open question, whether the 5/2 state is fully spin-polarized (see section 3.3.3). A not fully polarized state might be identified from a kink in the magnetic field dependence of the energy gap associated with a change in spin-polarization. Our data shows no sign of such a spin transition but due to the limited density range we can not reach a definite conclusion. Experiments in an in-plane magnetic field may provide more insight.

6.2 Data analysis and discussion

The discrepancy between experimental values of the 5/2 energy gap and theoretical predictions is large (as will be quantified below). A number of different effects are responsible for this discrepancy. In contrast to what is customarily done in literature, where the discrepancy is often simply attributed to disorder, we give here a more careful analysis. The finite width of the electronic wave function as well as LL mixing effects influence the intrinsic energy gap considerably.[2] Both effects should be taken into account explicitly when comparing activation gaps. We do this in section 6.2.2. All numerical calculations of the expected 5/2 energy gap and the quasiparticle size were done by Prof. R. Morf from the Paul Scherrer Institute in Villigen, Switzerland.

In an effort to elucidate the remaining discrepancy, which still is substantial, we investigate the size of the 5/2 quasiparticles in section 6.2.3. We find them to be surprisingly large. This underlines that the usual treatment of disorder by a simple level broadening is questionable.

6.2.1 Ideal 2D system

We first address an idealized case: A strictly two-dimensional system without disorder and LL mixing. Also full spin polarization is assumed as valid for the Pfaffian. With these simplifications we are left with the Coulomb interaction term.

The energy gap of the 5/2 state is assumed to originate from a BCS like pairing of Composite fermions (see section 3.3). The gap is the energy needed to create a quasiparticle-quasihole exciton. Numerical calculations of the energy gap are performed in a spherical geometry. One calculates the energy of

[2]The wave function width depends on the design of the heterostructure and there is no clear-cut relation to density. The influence of LL mixing decreases with increasing density (at fixed filling factor), contrary to the Coulomb interaction strength.

a QP-QH excitation with maximal angular momentum for a finite system of N electrons on a sphere.[3] The maximum number of electrons tractable with reasonable numerical effort is today $N = 20$. Calculations are done in dimensionless units and yield the dimensionless gap parameters $\widetilde{\Delta}_{5/2} = \Delta_{5/2}/E_q$ with the Coulomb energy E_q as energy scale (see section 3.2.1). By extrapolation to infinite systems as $1/N \to 0$ we obtain that the dimensionless gap parameter $\widetilde{\Delta}_{5/2}$ equals 0.036. Within the accuracy of the extrapolation this is consistent with a value of 0.03 obtained from density-matrix renormalization group techniques [63].

Since the Coulomb energy E_q scales with the inverse of the electron distance the activation gap of the idealized system is proportional to the square root of the density: $\Delta_{5/2} \sim \sqrt{n}$. This is shown as Δ^{ideal} for our exact diagonalization $\widetilde{\Delta}_{5/2} = 0.036$ result in Fig. 6.3(a). These calculated gaps are more than one order of magnitude larger than our experimental values Δ^{exp}.

6.2.2 Intrinsic corrections to the 5/2 energy gap

The ideal 5/2 energy gap is reduced by intrinsic effects and by disorder. Only the latter can in principle be eliminated. We first address the intrinsic gap reduction due to the finite width of the wavefunction and LL mixing. All calculations yield dimensionless gap parameters. To obtain actual values we need to multiply with the Coulomb energy scale (see above).

Finite width correction

We first consider corrections to the theoretical energy gaps due to the finite width of the electronic wave function [57, 59]. The electronic system is not strictly two-dimensional. Rather, the wave function Ψ has a finite extension within the quantum well and perpendicular to the plane (see the left inset to Fig. 6.3(c) and also section 2.4). In particular, when the average distance $d \sim l_B$ between electrons is not large compared to the wave function width w (measured by the standard deviation of $|\Psi|^2$), the Coulomb interaction is effectively weakened. The dimensionless gap parameter $\widetilde{\Delta}$ thus decreases with increasing w/l_B. This effect is computed by repeating the previously described exact diagonalization of finite systems for different w/l_B. The result is plotted in Fig. 6.3(b) as circles. From a fit of the numerical results we obtain in the

[3] The quasiparticle (QP) and quasihole (QH) size is of order $12\, l_B$ (see below), which is large compared to the possible spacing on the sphere. We thus added the Coulomb energy necessary to bring the QP and QH infinitely apart. Furthermore, we investigated the contribution from the QP and QH quadrupole moments but found it to be negligible.

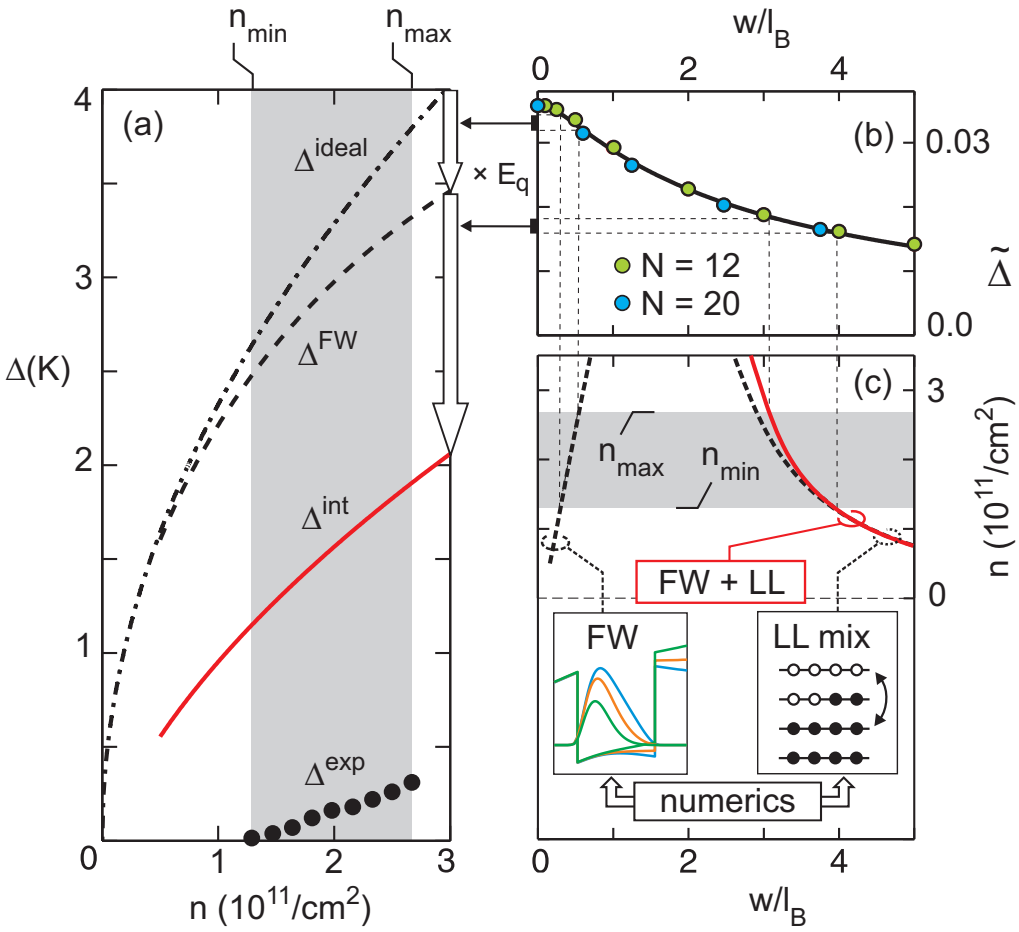

FIGURE 6.3: (a) Comparison of our measured 5/2 gaps to theory. See text for details. (b) Reduction of dimensionless gap parameter due to the normalized finite width w/l_B of the electronic wavefunction, obtained from exact diagonalization of up to 12 and 20 electrons. (c) Normalized finite width as a function of electron density. Note that the axes are reversed for better comparison with the other panels: The independent variable n is on the vertical axis. Left dashed line and inset: Actual finite width (FW). Right dashed line and inset: Effective width due to Landau level mixing. Solid red line: combined effect of FW and LL mixing.

w/l_B-range covered in this graph approximately

$$\widetilde{\Delta} = \frac{0.105}{2.59 + \sqrt{0.111 + (w/l_B)^2}} \tag{6.1}$$

To use this result we need to know the actual width w of the wavefunction in the QW as a function of electron density. We compute w for our specific heterostructure from a self-consistent Poisson and Schrödinger solver (see section 2.4). The left inset at the bottom of panel (c) shows the wave function in the QW for three different backgate voltages ($n = 1.0, 1.8$ and $2.7 \times 10^{11}/\mathrm{cm}^2$). The single-sided doping results in an asymmetric quantum well at low densities with the wave function pushed against the upper GaAs-AlGaAs interface. For increasing n, the wave function broadens and is more centered. Dividing the obtained widths by l_B yields the corresponding dimensionless widths. This is shown as the left dashed line in panel (c). The density range covered in our experiments is shaded. Using equation 6.1 we obtain the dimensionless gap parameters including finite width correction.[4] Panel (a) shows the resulting actual gaps Δ^{FW}. The correction due to the finite width is comparably small.

Landau level mixing correction

As a second correction, we take into account the effect of LL mixing. We refer to [62] for details on the calculation. It turns out that LL mixing causes a reduction of the Coulomb repulsion at short distances in a way very similar to the effects of the finite width of the wave function.The combined effect is accounted for by calculating an effective finite width w^{eff}. We find for our specific heterostructure approximately

$$w^{\mathrm{eff}}/l_B = 3.5\, n^{-0.25} + 0.9\, n^{-1} \tag{6.2}$$

where n is in units of $10^{11}/\mathrm{cm}^2$. The red solid curve in Fig. 6.3(c) shows this result.[5]

[4] The gap is reduced by an increasing amount as density increases. This is, however, only partly due to the increasing width w: As $l_B \sim 1/\sqrt{n}$, even a constant w would yield an increasing w/l_B and reduce the normalized gaps.

[5] The right dashed curve in panel (c) shows the effective width due to LL mixing alone. In our sample the LL mixing corrections dominate over the actual finite width corrections at $\nu = 5/2$. This is not surprising in view of the rather small cyclotron energy at these values of the magnetic field. The ratio of the Coulomb and cyclotron energy characterizes the LL coupling strength. It scales as $1/\sqrt{B}$ and is of order unity for our experiment. Note that the actual and effective finite width are not additive. Nevertheless, as the actual width is only a small correction, equation (6.2) should be a very good approximation for similar heterostructure designs.

Going to panel (b) using equation 6.1 we see that the reduction of $\widetilde{\Delta}$ is mainly the result of LL mixing effects and becomes more important at low densities. Finite width effects only lead to smaller corrections. Panel (a) shows the activation gap with both finite width and LL mixing corrections included as the intrinsic gap Δ^{int}. The corrections reduce the discrepancy between calculated gap and measured activation energy by about a factor of two. At the largest density there is still about a factor of 6 difference. In absolute terms this difference is about 1.5 K.

6.2.3 Disorder and quasiparticle size

Level broadening model

Finally, we address the influence of disorder. As described before (section 3.1.1, last paragraph) disorder is often accounted for by a static level broadening Γ. With Γ as the difference between the intrinsic and the experimentally determined energy gap $\Gamma = \Delta^{int} - \Delta^{exp}$ we find that Γ increases slightly with density and reaches $\Gamma \approx 1.5$ K at the highest density. An estimate for the influence of disorder can also be extracted from the electron mobility and the quantum lifetime. The mobility yields a broadening of only 1 mK. The quantum lifetime gives 0.19 K which is still much smaller than the Γ extracted from $\Delta_{5/2}$ measurements. Similar discrepancies have been reported before [131]. This is in line with the observation that the quality of FQHE is difficult to predict from the electron mobility (see section 5.3.1). Disorder from the remote ionized donors, although of little relevance for the mobility in these heterostructures, seems to play a central role for the 5/2 state [13, 16].

Saddle point model: Quantum tunneling

A more sophisticated way to treat disorder than a simple level broadening has been put forward (see section 3.1.1 and [41]). In contrast to the static level broadening model, the resistance depends not only on the disorder landscape but also on the size of the particles. The activation energy is substantially reduced if the quasiparticle size approaches or even exceeds the typical width of saddle points. The reason is that a large spatial extent of the QP facilitates tunneling through saddle points as illustrated in Fig. 6.4. The length scale of the saddle points is of order of the spacer thickness in modulation doped samples.

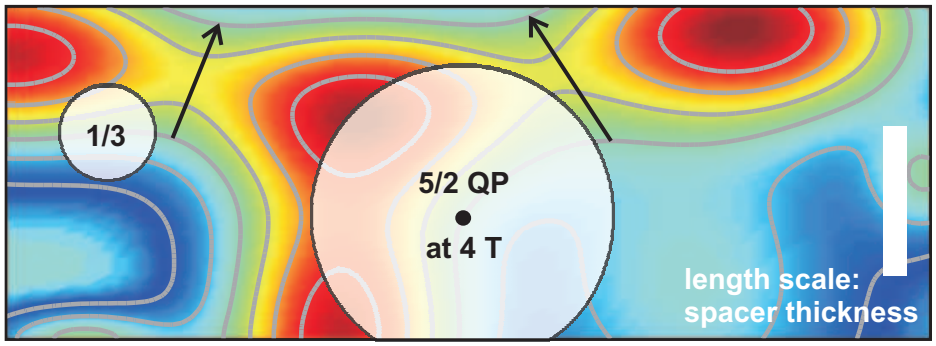

FIGURE 6.4: The disorder potential landscape from remote ionized donors (color and contour lines) has a length scale set by the spacer thickness (66 nm in our sample). Quasiparticles (QP) at filling $\nu = 1/3$ and $5/2$ are illustrated. The large size of the $5/2$ QP, greater than 150 nm at $B = 4$T, facilitates tunneling through saddle points. This produces dissipative resistance and reduces the measured activation energy.

5/2 quasiparticle size

To assess the possible importance of the quantum tunneling description of disorder we investigate the $5/2$ quasiparticle (QP) size. Details are given in the footnote.[6] The diameter of a typical QP is found to exceed 12 l_B. For a typical magnetic field of 4 T we find a quasiparticle size of more than 155 nm. In contrast, at $\nu = 1/3$ the typical QP size is around 2 l_B. Also $1/3$ is typically measured at much larger magnetic fields. For example, at 16 T, which corresponds to $n = 1.3 \times 10^{11}/\text{cm}^2$, the $1/3$ QP is only 26 nm in diameter. This is a factor of 6 smaller than the minimum size of the $5/2$ QP at 4 T.

The size of the $5/2$ QP of at least 150 nm at 4 T is larger than the spacer thickness in our heterostructure (66 nm) and thus larger than the length scale of saddle points in the RI disorder landscape as illustrated in Fig. 6.4. This facilitates tunneling through saddle points and reduces the activation energy. It can explain the large discrepancy between theory and experiment. It can also

[6] On a sphere occupied by N=20 electrons we localize two QHs on the north and south pole by a suitable pinning potential (left inset in Fig. 6.5) and numerically calculate the resulting charge density on the surface of the sphere. The diameter of the region of charge depletion will be interpreted as the size of the QH. Fig. 6.5 shows the charge density ρ along the polar angle θ (dashed line). It has pronounced dips at the north and south pole where the QHs are located. To find the missing charge (solid line) we integrate $(\rho - 1)\sin\theta$ along the polar angle θ. For the $5/2$ state we expect $-1/4$ for each QH. The missing charge has not yet settled at the equator. Hence, the true radius of the QH cannot be determined with confidence from exact calculations limited to 20 electrons on a sphere. Larger systems would be needed. However, it is possible to give a lower bound: As no plateau is observed in the missing charge, the QH radius clearly exceeds 6 l_B. Also our exact diagonalization results for varying strength of the pinning potential used to localize the QHs at the north and south pole give a lower bound of 4 l_B for the radius.

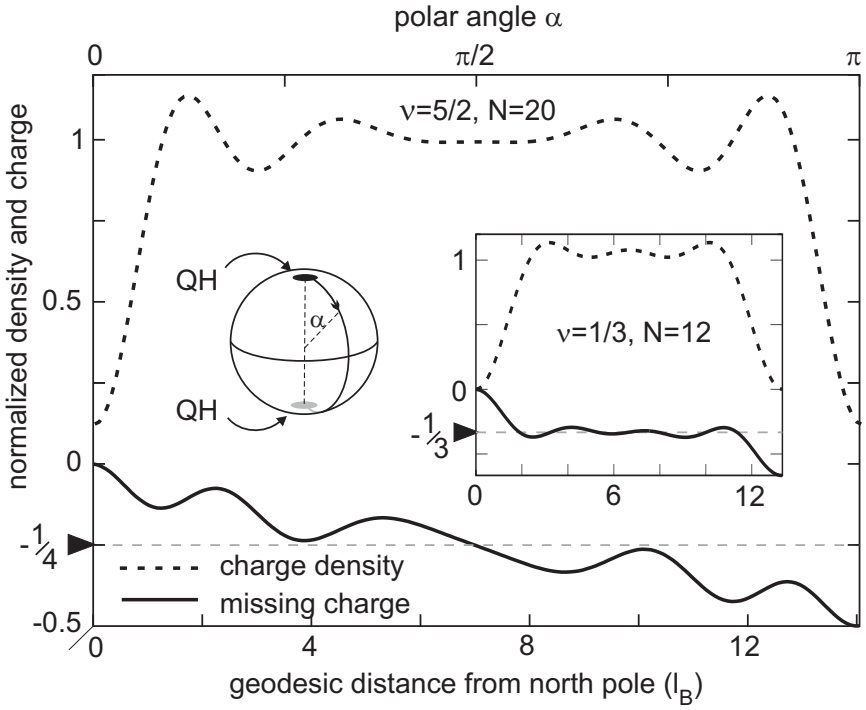

FIGURE 6.5: To determine the size of quasiholes for $\nu = 5/2$ and $1/3$ we put two quasiholes on a sphere occupied by N = 20 and 12 electrons respectively (left inset). The missing charge associated with the quasiholes is obtained from integration along the polar angle θ. For $1/3$ it levels at 2 l_B from the poles (right inset). For $5/2$ no plateau is observed even for 20 electrons. The quasihole diameter is thus $\gtrsim 12$ l_B, which is about 150 nm at $B = 4$T.

explain that this discrepancy is larger than suggested by the quantum lifetime, even though τ_q is limited by the same type of disorder, namely the ionized impurities in the doping layer.

6.2.4 Conclusions

Electron density tunable heterostructures offer unique opportunities. We here used an excellent sample to investigate the density dependence of the $\nu = 5/2$ state for one given bare disorder potential. As expected, the $5/2$ state is considerably strengthened with increasing density.

The density dependence of the $5/2$ energy gap was measured. The discrepancy between theory and experiment is large, even taking intrinsic corrections into account, namely the finite width of the wavefunction and LL mixing. The remaining discrepancy of roughly 1.5 K must be attributed to disorder. We compared this to an estimate of the level broadening obtained from the quan-

tum lifetime and found the latter to be an order of magnitude smaller. This indicates that the 5/2 quasiparticles are sensitive to different aspects of the disorder landscape than electrons in the weak magnetic field regime.

In an effort to elucidate this discrepancy, we investigated the size of the quasiparticles of the 5/2 state. These quasiparticles were found to be surprisingly large: The diameter exceeds 12 l_B or 150 nm at a magnetic field of 4 T. In a quantum tunneling model of the dissipative resistance the electrons need to tunnel through saddle points of the potential landscape to produce dissipative resistance. The geometric scale of the saddle points is determined by the spacer thickness. The large size of the 5/2 quasiparticles facilitates such tunneling events and reduces the activation energy. This can qualitatively explain the large discrepancy between theory and experiment.

Our results suggest that samples with larger spacers are needed to reduce the detrimental impact of disorder on the 5/2 activation energy because the relevant disorder length scale increases with the spacer thickness. For a larger ratio of the disorder length scale to the quasiparticle size tunneling across saddle points will be suppressed and consequently the activation energy will be increased.

The size of the 5/2 quasiparticles is found to be of the same order of magnitude as the geometric features of quantum point contacts [76, 77] and interferometer nanostructures [75] designed to control them in experiments towards topological quantum computation. This likely is important for the proper interpretation of data obtained on such devices.

We also believe that excellent density tunable wafers like the one we used here offer a large potential for further investigations. For example it is possible to quickly switch between different filling factors by changing the electron density. Experiments of this kind with the goal to investigate the spin polarization of the 5/2 state are ongoing in our group. Furthermore, it is known that the 5/2 state looses its quantized nature when the second electronic subband in a wide quantum well is occupied [20]. To investigate the transition density tunable samples are needed. Such experiments are also pursued now in our group.

Chapter 7

Compressibility of a 2DES under microwave irradiation

In this main experimental chapter of this thesis, we aim at measuring the compressibility of a 2DES under microwave irradiation in order to see predicted microwave induced compressibility oscillations (MICRO, see section 4.2.2). Measurements are done with the help of a single electron transistor (SET) as sensitive local probe. After the setup, the sample fabrication and the principle of measurement, we describe the actual experiments: The SETs need to be characterized carefully as their properties change with magnetic field and microwave irradiation. Two surprising complications are encountered: First, the microwave power at the sample position is strongly inhomogeneous and varies with frequency. Second, the compressibility even in the absence of microwave radiation shows unexpected behavior. Finally we present compressibility measurements in the presence of microwaves. MICRO are observed. Strong magnetoplasmon structures are visible. The data are analyzed and discussed.

7.1 Methods

7.1.1 Microwaves in a dilution refrigerator

Compressibility measurements with the help of a single electron transistor (SET) need to be performed at ultra-low temperatures T $\lesssim$ 100 mK. Even though MIRO can be seen above 1 K, the SET that we use as potential probe requires these low temperatures (the properties of SETs are described in section 7.1.3). We used a top loading Oxford dilution cryostat. The sample, placed near the end of a sample holder of approximately 3 m length, is immersed directly in the ^{3}He/^{4}He mixture.

Figure 7.1 illustrates the measurement setup. Microwave radiation is generated outside the cryostat by a backward wave oscillator (BWO) that can cover frequencies from 50 to 170 GHz. The radiation is guided in an oversized, metallic hollow waveguide with a cross section of 6.5 × 13 mm^2 (WG19) that is incorporated in the sample holder. The waveguide is blanked off at the top with a quartz glass window and black polyethylene foil to block visible light. It is sealed at the bottom with a Kapton window. Between the windows the waveguide is always kept evacuated. After the Kapton window the waveguide is terminated by a horn. The sample is located near the opening of the horn (see Fig. 7.1). The sample is glued into a chipcarrier with 24 pins that are connected by 24 thermocoax cables to the top of the sample holder outside the cryostat where measurement equipment can be connected.

To regulate the power of the microwave radiation a variable attenuator is used. The attenuation level is regulated by the amount of current I_{att} applied to the attenuator. After the attenuator a beam splitter is incorporated in the waveguide and a fixed part of the radiation is supplied to a broadband detector. However, the radiation power measured at this position is not the power that arrives at the sample: Before reaching the sample the radiation is damped as it travels approximately 4 m in the waveguide. Moreover, the waveguide is oversized for the frequencies we use and the geometry contains twists, tapered sections and a horn near the sample. Multiple reflections can occur that strongly change with frequency. Also, the radiation field near the sample may be inhomogeneous due to nodes in the radiation electric field. These difficulties are in fact observed in our setup and are described in section 7.3.1.

7.1.2 Sample design and fabrication

Measurements are performed on Hallbar-shaped 2DES with aluminum based single electron transistors (SETs) evaporated on the surface. Details on the used heterostructure were given in 5.4.2. A detailed fabrication protocol can be found in Appendix B. Here we describe general aspects of the sample fabrication.

Hallbars are fabricated by standard optical lithography techniques. The mesa is defined by wet-chemical etching. Alloyed metallic contacts are fabricated from a Au/Ge/Ni compound and thermal annealing. Bondpads are coated with an additional Cr/Au layer to facilitate wire-bonding.

Connections are added for the subsequent fabrication of SETs. These connections consist of a thin layer of AuPd and a thick layer of Au on top. Near the region where the SET is later placed, the Au does not entirely cover the thin AuPd (see lower left panel in Fig. 7.2). This is needed because the aluminum for the SETs makes better electrical contact to AuPd than it does to

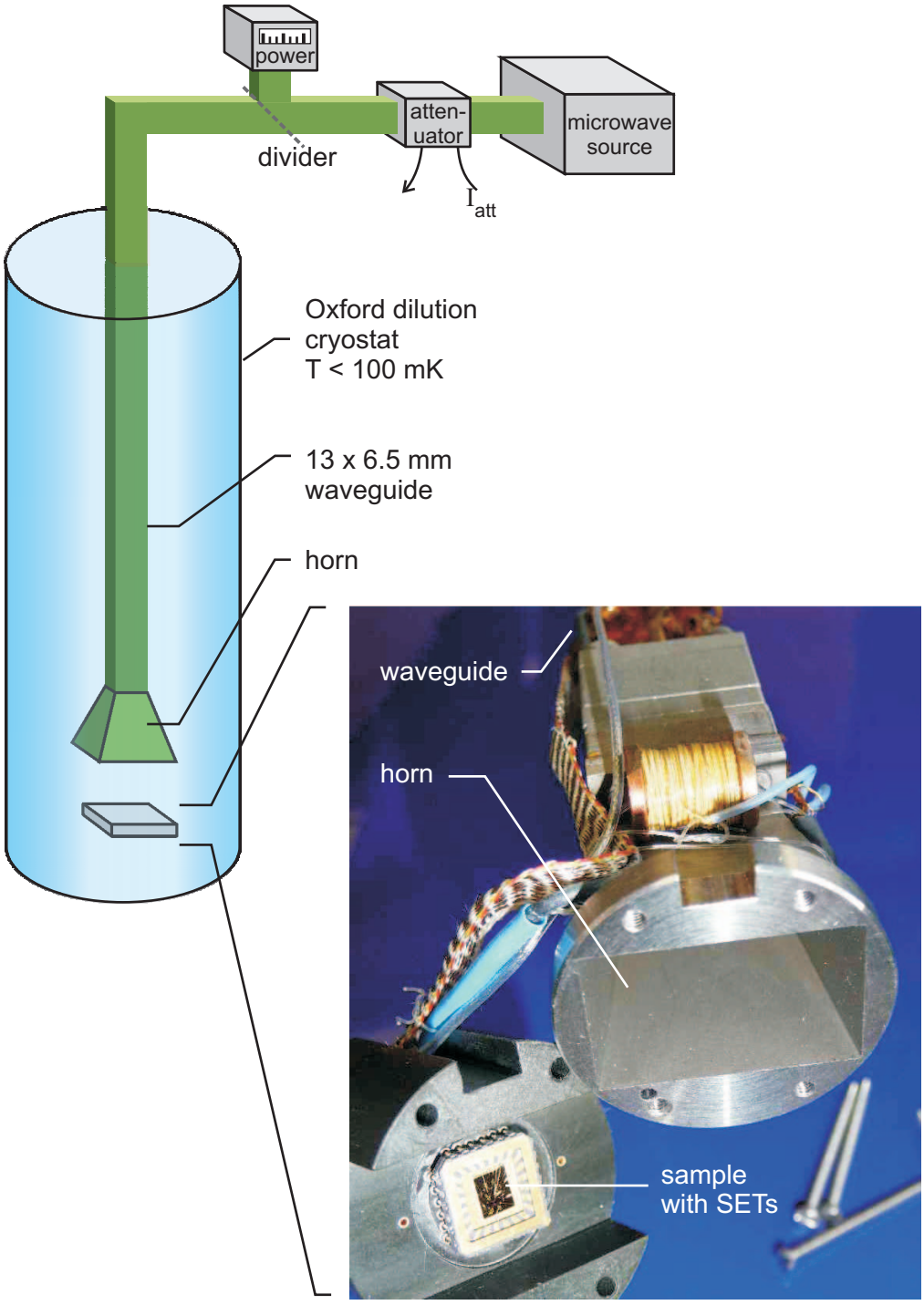

FIGURE 7.1: Overview of the measurement setup: Microwave radiation is guided into a dilution cryostat by a metallic hollow waveguide. The power is controlled by an attenuator and measured by a power meter. Magnification: Photograph of the sample and the horn at the end of the waveguide.

Au (purple plague). Furthermore, the Au layer is thicker than 100 nm while the total amount of Al for the SET is much less. The thin Al might not be able to climb the high step and thus electrical contact between the SET connections and the actual SET would be broken.

The SETs used in this work are fabricated in the group of Prof. Amir Yacoby at Harvard University, USA. In this group a recipe for SET fabrication had been developed by Basile Verdene. The research group then moved from Weizmann Institute of Science, Israel, to Harvard University. Setting the process up again was done by Jonah Waissman and Vivek Venkatachalam with partial help from us. All SETs that we use for measurements are fabricated by Vivek Venkatachalam.

An SET as we use it consists of a small metallic island that is weakly coupled to two leads by tunnel junctions (we describe the physics of SETs in the next section). Due to the required small dimension electron beam lithography is used to define the SET structures. Metalization then takes place in a two-step process: First, a 25 nm thick layer of Al is evaporated to form the island. The Al surface is then oxidized by exposure to oxygen with controlled time and pressure.[1] In a second evaporation the source and drain leads are metalized, each overlapping the island in a small area (see lower right panel in Fig. 7.2). The overlap regions form at the same time capacitive couplings as well as tunnel junctions. The capacitances are defined mainly by the overlap area, the tunnel coupling strength mainly by the oxidation time and pressure. This is because the tunnel coupling depends exponentially on the oxide thickness and the capacity linearly. The sample remains in the evaporation chamber during the entire process of the first evaporation, the oxidation and the second evaporation. The selective evaporation is possible by defining the structures as narrow, deep trenches in the E-beam resist and evaporation from different angles. For trenches perpendicular to the evaporation direction metal deposition is shaded by the resist. Thus, only the island is deposited in the first step. After the first evaporation the sample is oxidized and the angle is adjusted in-situ, this time shading the island and metalizing source and drain leads. The shading only works for narrow trenches. Once the trenches surpass a certain width selectivity is lost. This can clearly be seen in the lower right panel of Fig. 7.2. After SET fabrication the samples are sent to our institute where liftoff is performed and the samples are glued into chip carriers, bonded, mounted in the sample holder and tested at room temperature before cooldown and measuring.

[1] We did not measure the thickness of the oxide layer. In a similar SET fabrication process the oxide thickness was measured to be $\lesssim 2$ nm [34].

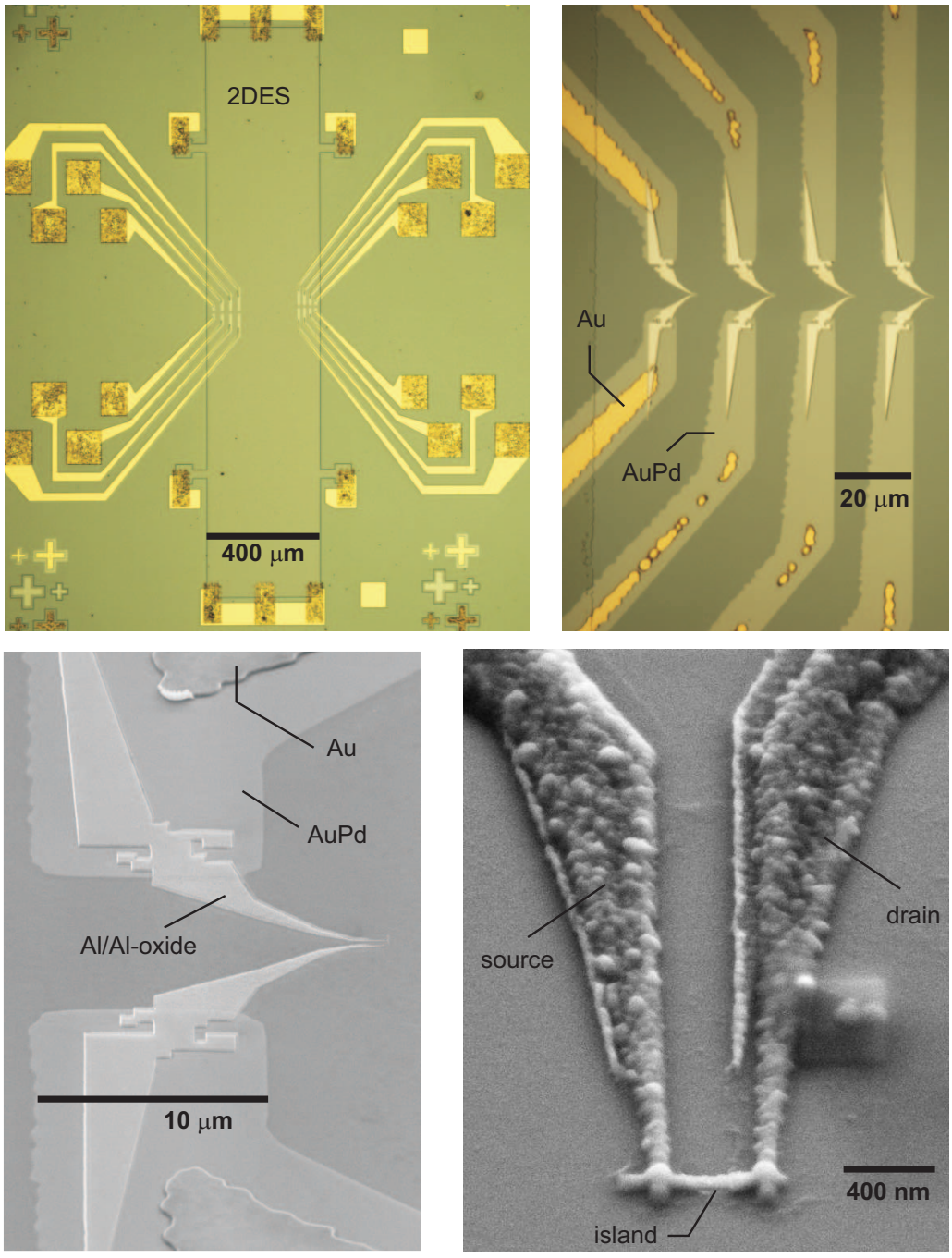

FIGURE 7.2: Top: Photographs of a Hallbar with connections for 8 single electron transistors (left) and magnification with 4 SETs (right). Bottom: SEM images of SET legs overlapping the thin AuPd layer of the connections (left) and a close-up on the island area of an SET (right).

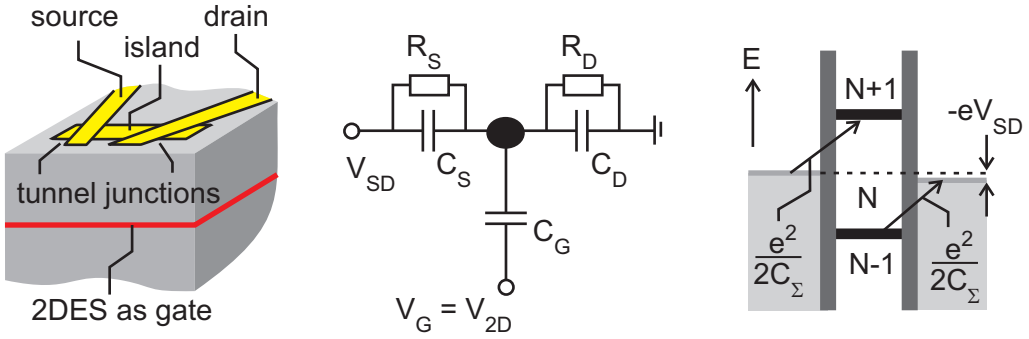

FIGURE 7.3: Left: Sketch of an SET on a sample surface. The buried 2DES serves as a gate. Middle: Capacitive (to gate) and resisto-capacitive (source and drain leads) coupling of the island to its surroundings. Right: Energy diagram for adding or subtracting an electron to/from a neutral island.

7.1.3 Single electron transistor as local potential probe and principle of compressibility measurement

For compressibility measurements small changes in the chemical potential have to be detected. For this a single electron transistor (SET) is used. After reviewing Coulomb blockade as the working principle of an SET we describe its use in our compressibility measurement.

Coulomb blockade as working principle of SETs

An SET consists of an island, a source contact, a drain contact and a gate as sketched in Fig. 7.3. Source and drain are capacitively coupled to the island as well as weakly tunnel coupled. The gate is only capacitively coupled to the island. In our experiments we use the buried 2DES as a gate. The capacitive coupling of the island to its surroundings leads to a charging energy

$$E_{\text{charge}} = \frac{e^2}{2C_\Sigma}; \qquad C_\Sigma = C_S + C_D + C_G. \tag{7.1}$$

that has to be payed for adding or subtracting an electron from the island (see right part of Fig. 7.3). Shrinking the size of the device reduces the capacity and increases the charging energy. Charging effects become important when the charging energy surpasses the thermal energy of electrons: $E_{\text{charge}} > k_B T$.

The gate, in our case the 2DES, can be used to modify the preferred charging state of the island: In the situation depicted in the right panel of Fig. 7.3 the Fermi level of the leads and the quasi-Fermi level of the island with N electrons are aligned. The energy E_{charge} has to be payed to add or subtract an electron.

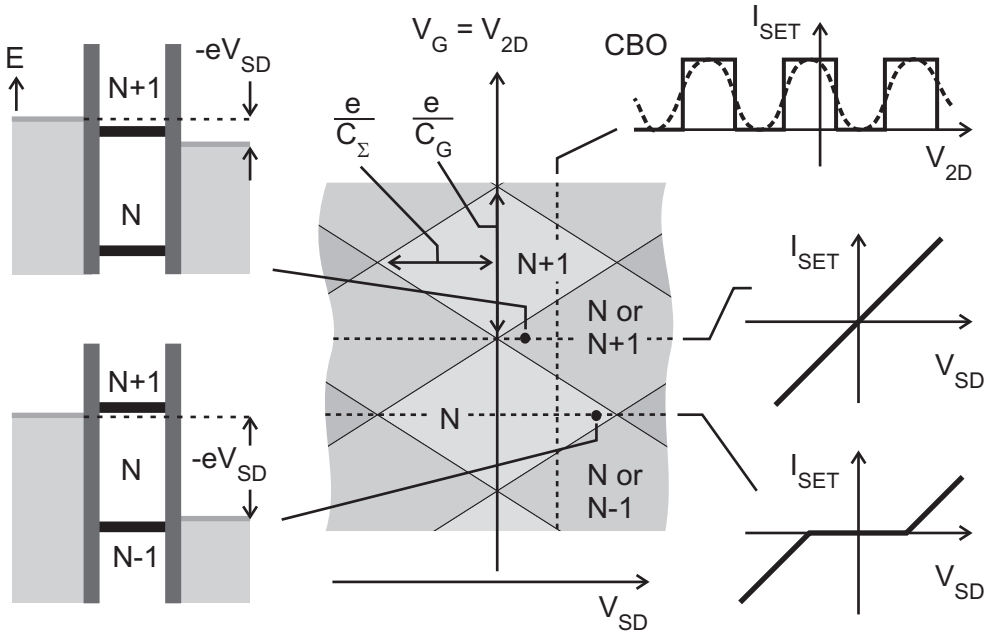

FIGURE 7.4: Middle: Charge stability diagram of an SET. Left: Two situations for finite source-drain and gate voltages. Right: Cuts through the charge stability diagram: In the top panel I_{SET} shows Coulomb blockade oscillations (CBO) as a function of V_{2D}. Dashed is a realistic trace including finite temperature and noise. On the bottom two different $I-V$ curves. The lower one shows Coulomb blockade as a region of current suppression.

Changing the electrostatic potential of the 2DES can lead to a situation where N or $N+1$ electrons are equally likely on the island (top left panel in Fig. 7.4). A current can then flow through the SET upon applying a source-drain voltage and the $I_{\mathrm{SET}}-V_{\mathrm{SD}}$ characteristics is linear. Otherwise, current is suppressed in a finite voltage window (bottom left panel in Fig. 7.4). The $I_{\mathrm{SET}}-V_{\mathrm{SD}}$ characteristics shows a flat region. This situation is called Coulomb blockade.

At a fixed source-drain voltage we can switch between current and current suppression by changing the electrostatic potential of the 2DES by a voltage V_{2D} applied to an electrical contact. The resulting changes in I_{SET} are called Coulomb blockade oscillations (CBO, see top right panel of Fig. 7.4). In our experiments we will measure electrostatic potential changes from changes in the current through the SET.

The reason for Coulomb blockade is the discreteness of the electronic charge resulting in a finite charging energy. Energy quantization due to quantum mechanical confinement may add to this effect but plays usually no role for metallic SETs. This can be different in semiconducting SETs due to the much

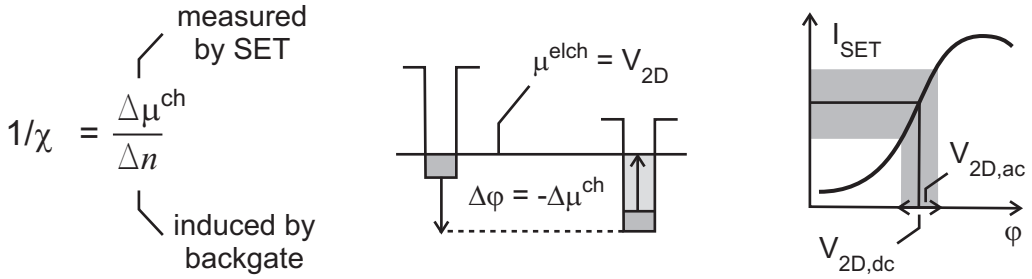

FIGURE 7.5: Left: Idea of compressibility measurement. Middle: The electrochemical potential is fixed by the voltage applied to the 2DES. Density-induced changes in the chemical potential (measured from the bottom of the QW) thus have to be balanced by an equal and opposite change in electrostatic potential φ. This is detected by the SET. Right: The sensitivity of the SET, namely the change in current induced by changes in electrostatic potential, is measured by applying a modulation voltage $V_{\mathrm{2D,ac}}$ directly to the 2DES.

lower density of states. For more details on the physics of SETs we refer to [132, 133] and references therein.

Principle of compressibility measurement

We introduced the (inverse) compressibility $1/\chi$ in section 2.1 as $\partial\mu^{\mathrm{ch}}/\partial n$. The basic measurement idea is to induce Δn by a voltage applied to a backgate and to measure the resulting $\Delta\mu^{\mathrm{ch}}$. Here we develop how this idea can be put into practice with the help of a single electron transistor.

- A density change Δn is induced in the 2DES by applying a voltage ΔV_{BG} to the backgate:
$$\Delta n = \frac{\partial n}{\partial V_{\mathrm{BG}}}\Delta V_{\mathrm{BG}} \tag{7.2}$$
In order to perform a lock-in measurement we periodically modulate the BG voltage with a function generator. The quantity $\partial n/\partial V_{\mathrm{BG}}$ is determined prior to compressibility measurements for example from the change in the slope of the Hall curve.

- The induced density change leads to a change in the chemical potential of the 2DES:
$$\Delta\mu^{\mathrm{ch}} = \frac{\partial\mu^{\mathrm{ch}}}{\partial n}\Delta n \tag{7.3}$$
where the inverse compressibility $1/\chi = \partial\mu^{\mathrm{ch}}/\partial n$ is the quantity we are interested in.

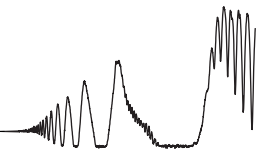

- The change in chemical potential is balanced by an equal and opposite change in the electrostatic potential φ of the 2DES:

$$\Delta\varphi = -\Delta\mu^{\mathrm{ch}} \tag{7.4}$$

  This is because in equilibrium the sum of the two, the electrochemical potential $\mu^{\mathrm{elch}} = \varphi + \mu^{\mathrm{ch}}$ is fixed by the voltage V_{2D} applied to an electrical contact to the 2DES (see Fig. 7.5).

- The change in electrostatic potential is measured as a change in current through the SET:

$$\Delta I_{\mathrm{SET}} = \frac{\partial I_{\mathrm{SET}}}{\partial\varphi}\Delta\varphi \tag{7.5}$$

  The sensitivity of the SET $\mathrm{sens} = \partial I_{\mathrm{SET}}/\partial\varphi$ is the slope of the CBO (see Fig. 7.5). We describe below how it is maximized during measurement.

Inserting equations 7.2 to 7.5 into each other relates the applied BG voltage to the measured change in current through the SET. Solving for $1/\chi$ we find:

$$1/\chi = -\frac{\mathrm{signal}}{\mathrm{sens}} \Big/ \frac{\partial n}{\partial V_{\mathrm{BG}}}, \qquad \begin{aligned} \mathrm{signal} &= \frac{\partial I_{\mathrm{SET}}}{\partial V_{\mathrm{BG}}} \\ \mathrm{sens} &= \frac{\partial I_{\mathrm{SET}}}{\partial\varphi} \end{aligned} \tag{7.6}$$

The electrical measurement setup is shown in Fig. 7.6. We apply a modulation voltage to the BG and to the 2DES at two incommensurate frequencies to measure the SET sensitivity in parallel with the response to density changes.[2] The quantities are separated by two lock-ins referenced by the respective modulation frequencies. Inserting units convenient for our experiments we get

$$1/\chi[10^{-14}\mathrm{eVcm}^2] = -\frac{\mathrm{signal}}{\mathrm{sens}}\,\frac{\Delta V_{\mathrm{2D}}[\mu\mathrm{V}]}{\Delta V_{\mathrm{BG}}[\mathrm{V}]} \Big/ \frac{\partial n}{\partial V_{\mathrm{BG}}}[10^8/\mathrm{Vcm}^2] \tag{7.7}$$

where ΔV_{2D} and ΔV_{BG} are the amplitudes of the modulation voltages. In our experiments we typically use $\Delta V_{\mathrm{2D}} = 100\ \mu$V and $\Delta V_{\mathrm{BG}} = 1$ V. The amount of electron density change per Volt applied to the BG is typically $\frac{\partial n}{\partial V_{\mathrm{BG}}} \approx 2 \times 10^8/\mathrm{cm}^2\mathrm{V}$.

In this thesis we always use the *inverse* compressibility instead of the compressibility $\partial n/\partial\mu^{\mathrm{ch}}$. The reason is that it corresponds to what we measure:

[2] The modulation voltage $V_{\mathrm{2D,ac}}$ applied to the 2DES in order to measure the SET sensitivity changes the electron density as well. However, the modulation amplitude is typically four orders of magnitude smaller than the BG voltage. We thus regard the density as constant for the sensitivity measurement.

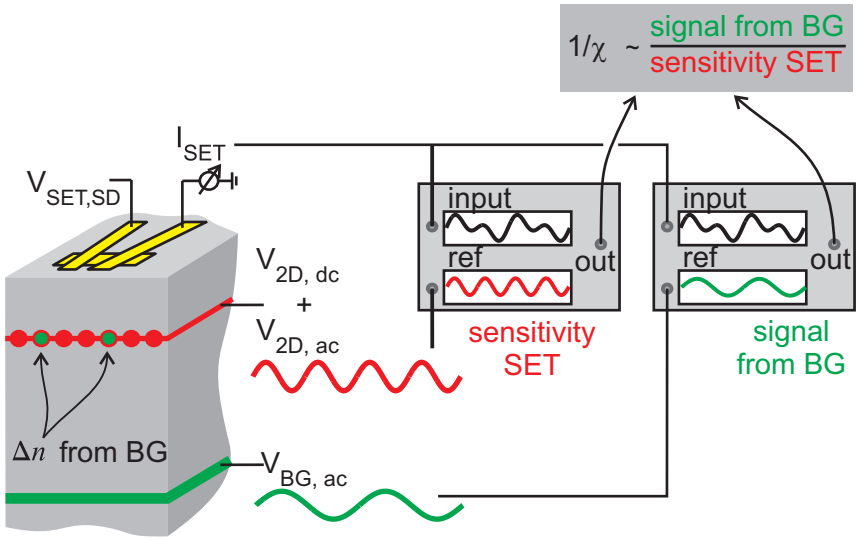

FIGURE 7.6: Compressibility is measured by inducing a time periodic density modulation with a BG voltage and measuring the resulting changes in SET current with a lock-in amplifier. The sensitivity of the SET is measured in parallel by applying a small ac modulation voltage of a different frequency directly to the 2DES and measuring the SET current with a second lock-in amplifier.

We induce a density change and measure μ^{ch}, not vice versa. On a more practical level we also use $1/\chi$ to avoid singularities in the graphs: $1/\chi$ can become negative for small electron densities (see section 7.3.2). Also the measurement signals may fluctuate close to zero or to the negative. Inverting the results would lead to large fluctuations and singularities with sign inversions. $1/\chi$ is the "nicer" quantity to plot.

SETs with superconducting gap

Here we describe a technical complication. It is not of fundamental importance but needs to be taken into account for experiments. In our experiments $I_{\mathrm{SET}} - V_{\mathrm{SD}}$ curves are substantially different from what is shown in Fig. 7.4. This is because the Al making up the SETs is a superconductor at low temperatures and low magnetic fields. Thus, no current can flow through the SET unless the source-drain voltage overcomes also the superconducting gap (see for example [134, 135]). A typical situation is depicted in Fig. 7.7.

The superconducting gap is gradually suppressed with increasing magnetic field. The critical magnetic field that quenches superconductivity is only 10 mT for bulk aluminum at $T = 0$ K (the critical temperature is 1.2 K which is large compared to our measurement temperature of about 50 mK). Yet, due to the thin film the critical field is much higher for our SETs. We observe a

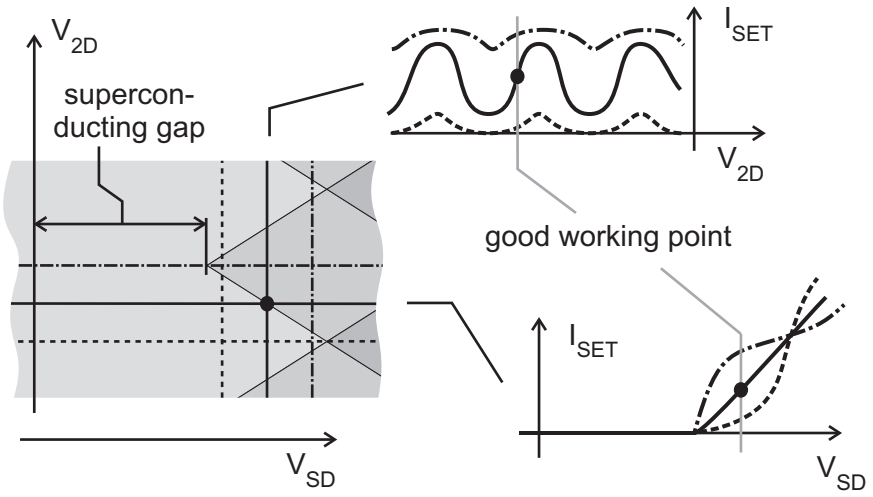

FIGURE 7.7: A superconducting gap modifies the charge stability diagram. Insets: To find a working point with high SET sensitivity both the source-drain voltage and the gate voltage (in our case the 2DEG voltage) have to be chosen correctly.

complete suppression of superconductivity at $300 - 500$ mT. Unfortunately, we are interested exactly in the field range where the transition takes place. The source-drain voltage therefore has to be continuously adjusted when sweeping the magnetic field.

Selection of SET working point to maximize SET sensitivity

For best results, compressibility measurements should be performed at maximum SET sensitivity. For this the working point of the SET has to be chosen carefully in the $V_{2D} - V_{SD}$ plane as illustrated in Fig 7.7.

As mentioned above, the superconducting gap is suppressed in the magnetic field range covered in our experiments. During a $B-$sweep the SET source-drain voltage has to be continuously adjusted. Concerning the 2DES voltage, we found that in most cases no adjustment is necessary for a typical magnetic field interval. Instead, a good value for V_{2D} is chosen prior to each B-sweep.[3]

Furthermore, the sensitivity is strongly altered by microwave irradiation, making the selection of a good working point even more crucial. Examples for different magnetic fields and microwave powers are given in the next section.

[3]We implemented an adaptive procedure as well: $V_{2D,dc}$ was changed by a small step. If this increased the sensitivity the next step was taken in the same direction, if it decreased the direction was reversed. This, however, did not always work well and in any case strongly limits the magnetic field sweep rate as B-induced changes need to happen slower than $V_{2d,dc}$-induced ones. Fortunately the adaptive procedure was often not necessary.

7.2 Characterization procedure and proof of compressibility measurement

To put the compressibility measurement principle described in the last section into practice requires preparatory characterization measurements. In this section we go through the necessary steps: First, the transport properties of the 2DES are checked, then the SETs are characterized with respect to their source-drain and 2DES voltage behavior. Finally, as a proof of principle, we present a compressibility measurement in the absence of microwave radiation.

7.2.1 2DES transport properties

Transport properties of the samples are checked for two reasons: First, we verify that MIRO are observed and we check their pronouncedness for various microwave powers. The top left panel of Fig. 7.8 is a representative example for the heterostructure used for compressibility measurements. For a given heterostructure we usually find hardly any variation among different Hall bars.

In the top right panel of Fig. 7.8 we introduce a color code for microwave powers that we will frequently refer to in the following. Note that we usually specify the *source* power. The power arriving at the sample can be very different, as we discuss in detail in section 7.3.1.

We measure also the amount of density change induced per Volt of applied BG voltage. This quantity is needed to evaluate later compressibility measurements. As most of our samples do not have an in-situ grown BG we instead use the metal surface of the chip carrier on top of which the sample is placed. The distance from BG to 2DES therefore is the thickness of the substrate, which is about 0.5 mm in our case. Due to this large distance we need high voltages to achieve a substantial density change. In the bottom panels of Fig. 7.8 we applied +30 V, 0 V and −30 V. Densities are extracted from the B-field position of certain filling factors.

In the bottom left of Fig. 7.8 we point out an anomaly observed in the longitudinal resistance for different applied BG voltages: At $B = 0$ we find that R_{xx} decreases with increasing density as expected due to increased screening of disorder. For the same reason one expects an increased amplitude of the SdH oscillations (see equation 2.20), and this is what we do observe on samples with an in-situ grown BG. Here, however, the SdH amplitude is maximal for *zero* BG voltage, not for the maximal density. This is consistently observed on all samples of our wafer without an in-situ BG where we need to use the chip carrier to change the electron density. We will come back to this finding in section 7.3.2.

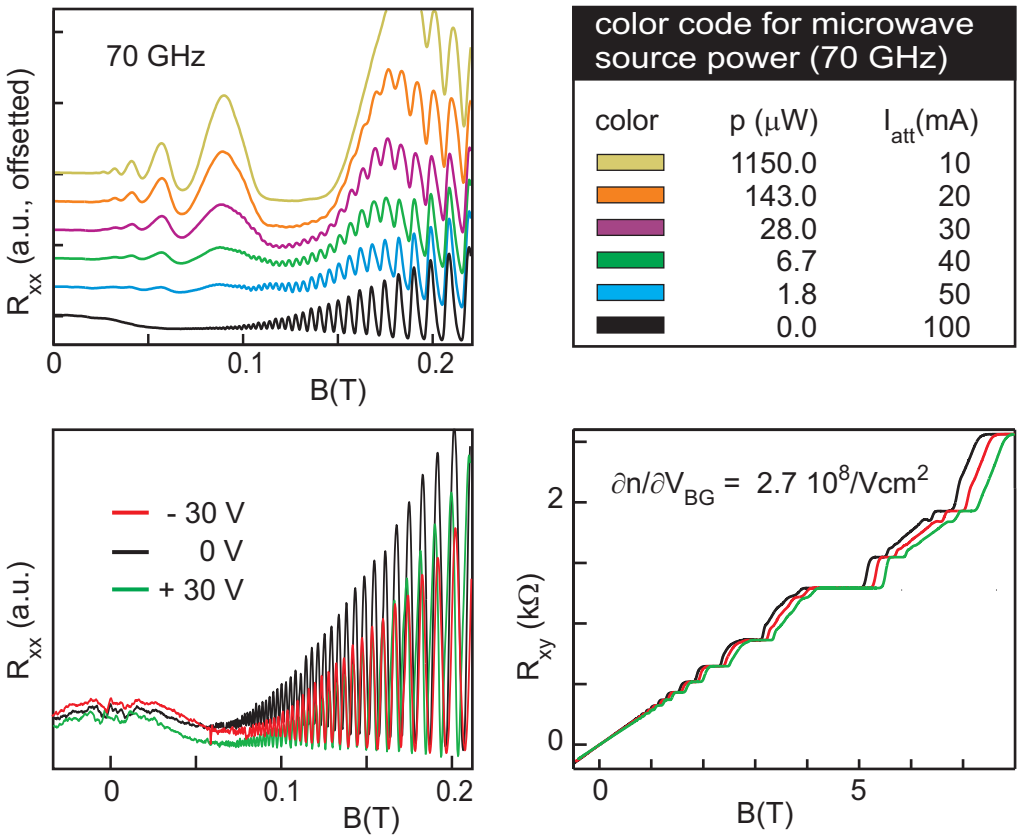

FIGURE 7.8: Top left: MIRO traces typical for the sample we use for compressibility measurements. Top right: In the following we will indicate microwave source powers by a color code. Bottom left: Anomalous V_{BG} dependence of SdH oscillation amplitude. Bottom right: Hall resistance for different backgate voltages.

7.2.2 SET characterization: V_{SD} dependence

We check the $I_{\mathrm{SET}} - V_{\mathrm{SD}}$ characteristics of our SETs as a function of the applied magnetic field and the microwave power and frequency. We do not yet apply a modulation voltage to the 2DES or BG (in contrast to measurements described in the next section).

Figure 7.9 shows in the left panel typical $I_{\mathrm{SET}} - V_{\mathrm{SD}}$ traces of an SET for different magnetic fields in the absence of microwave irradiation. Each bundle of traces corresponds to various 2DES voltages (acting as a gate to the SET). From these plots we can identify the V_{SD} values at which the CBO amplitude is maximal. Due to the gradual suppression of the superconducting gap the first CBO shifts to lower V_{SD}. We record these values and fit them with a polynomial as a function of B-field for later use as SET working points. This part is very straightforward and poses no problems.

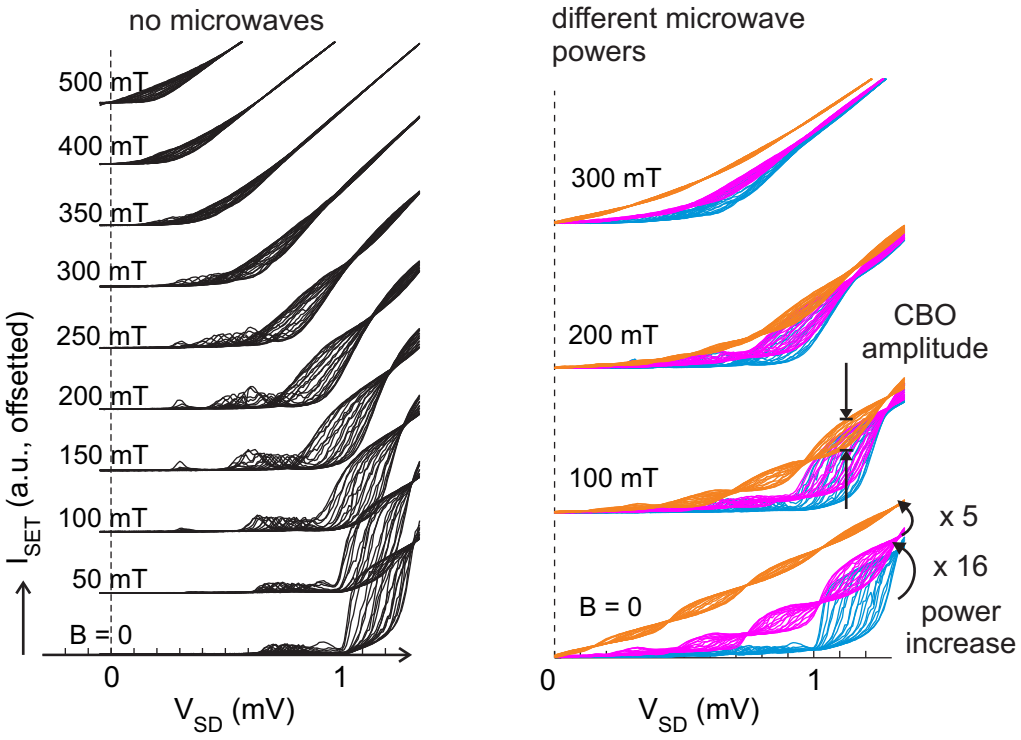

FIGURE 7.9: Left: Source-drain characteristics of an SET in absence of microwaves. At each magnetic field a number of traces for different V_{2D} has been overlayed to illustrate the Coulomb blockade oscillation (CBO) amplitude. At $\approx$ 500 mT the superconducting gap is completely suppressed. Right: Three microwave irradiation powers are shown for each $B-$field (powers indicated by colors as in Fig. 7.8). The CBO amplitude is reduced by the radiation.

In the right panel of Fig. 7.9 we show the $I_{\mathrm{SET}} - V_{\mathrm{SD}}$ characteristics of an SET for three microwave irradiation powers of a fixed frequency. The SET characteristics are modified substantially. Especially the amplitude of CBOs can be strongly reduced. The amount of this reduction shows a complicated dependence on four things: The particular SET, the applied magnetic field, the microwave power sent into the cryostat and the microwave frequency (details are given in section 7.3.1). This can cause serious problems: If the sensitivity of an SET is reduced too much by the radiation, we can not use it for measurements.

The superconductivity of the SETs introduces a number of features in the $I_{\mathrm{SET}} - V_{\mathrm{SD}}$ traces: At source-drain voltages slightly before the first CBO sets in, a smaller peak is seen whose position shifts with V_{2D} (in the above example between $V_{\mathrm{SD}} = 0.7$ and 1 mV for $B = 0$). Another peak with fixed position at about $V_{\mathrm{SD}} = 0.4$ mV arises at about $B = 100$ mT. Furthermore, in the presence of microwave radiation CBOs are seen also in the superconducting gap. The

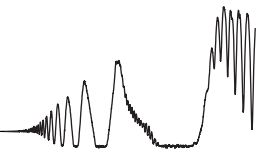

finite slope of the $I_{\mathrm{SET}} - V_{\mathrm{SD}}$ traces induced by the microwave irradiation in the superconducting region can be a non-monotonous function of the applied magnetic field, as is the case in Fig. 7.9. We do not go into this rich field of physics as it does not influence our use of the SET as a local probe.

7.2.3 SET characterization: $V_{2\mathrm{D}}$ dependence

We check the $I_{\mathrm{SET}} - V_{2\mathrm{D}}$ characteristics of our SET as a function of the applied magnetic field and the microwave power and frequency. For this, the source-drain voltage is fixed according to the previously recorded values. Here we apply a modulation voltage to the 2DES and BG and simultaneously measure three quantities:

- dc current through the SET I_{SET}
- SET sensitivity $\partial I_{\mathrm{SET}}/\partial V_{2\mathrm{D}}$
- BG signal $\partial I_{\mathrm{SET}}/\partial V_{\mathrm{BG}}$

In Fig. 7.10 we give an example of these three quantities taken at four different magnetic fields covering the range that we later need for compressibility measurements. Each graph shows four colored traces corresponding to different microwave source powers (see Fig. 7.8). The maximum power shown here would be judged as fairly low from transport studies because MIRO are poorly pronounced. In fact, most transport studies were carried out at powers roughly 40 times larger. This illustrates a problem of our measurements: Judging from transport data we would like to measure compressibility at much larger powers but our SETs loose sensitivity then.

We observe that in general the sensitivity of SETs decreases with increasing magnetic field and especially with microwave power. The combination of suppressing the superconductivity together with microwave irradiation makes the SET behavior more complicated than simple CBO. For example the pink trace in Fig. 7.10 shows an additional maximum within one CBO that develops with increasing microwave power. Correspondingly, the SET sensitivity (which is the derivative of I_{SET}) shows multiple maxima, as does the BG signal. At 300 mT, for this SET, the sensitivity and the BG signal are very small and no measurements can be performed at higher microwave powers. The data shown in Fig. 7.10 are representative for all our SETs, even though there is a certain amount of variation.

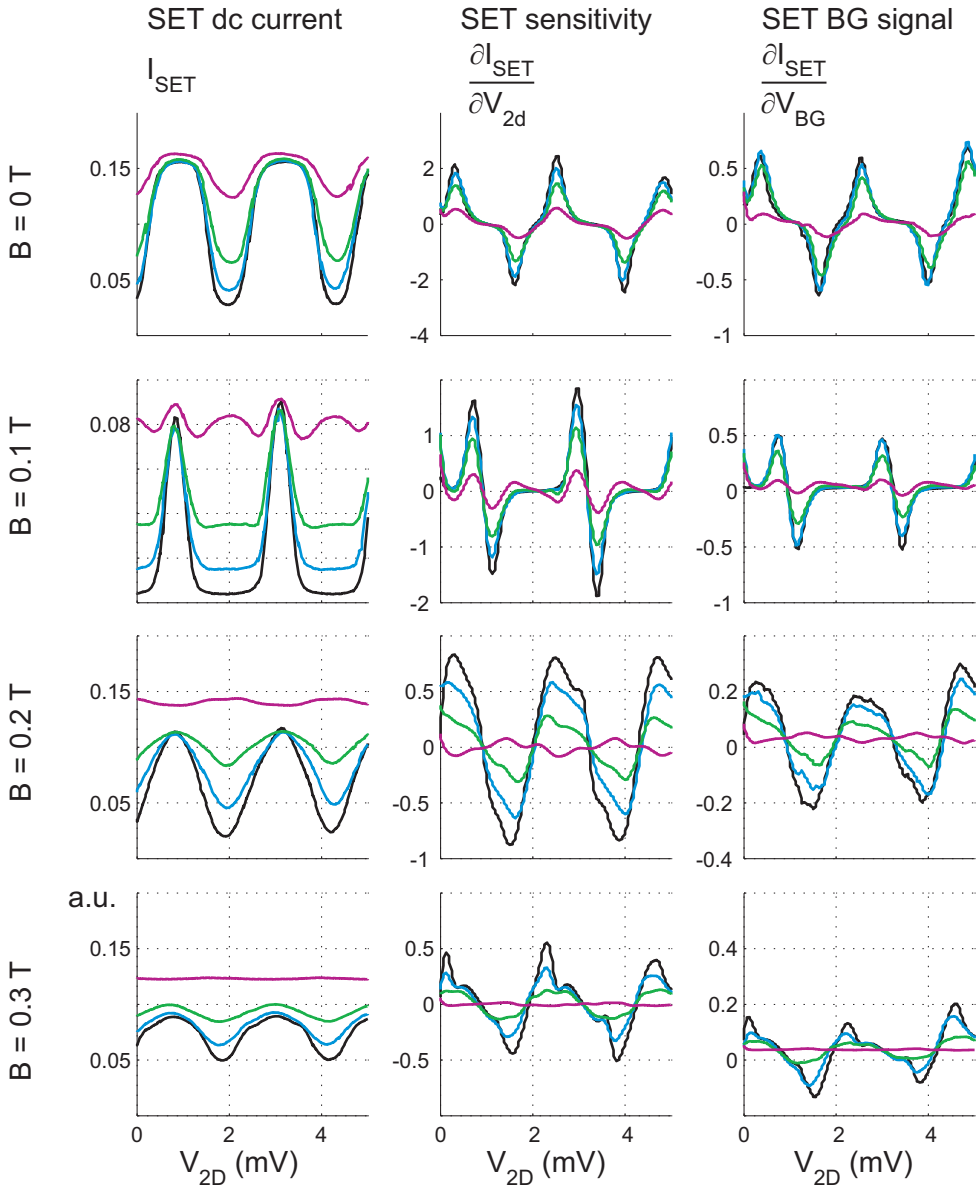

FIGURE 7.10: V_{2D} characteristics of an SET for different magnetic fields. Powers are indicated by colors as in Fig. 7.8. To the 2DES we apply both a dc-voltage (shown on the x-axes of the graphs) and a small ac-modulation voltage. To the backgate we apply an ac-voltage to modulate the electron density. The SET dc-current, the sensitivity and the BG signal are measured in parallel, the latter ones by lock-in amplifiers. Units on y-axes are arbitrary but consistent for each quantity. Even for the largest power shown here (pink trace), where the SET sensitivity is low, MIRO are poor in a transport measurement.

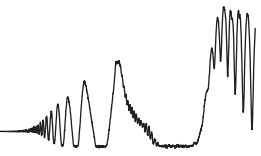

7.2.4 Compressibility measurement without microwaves

As a proof of principle we perform a compressibility measurement without microwave irradiation. An example is shown in Fig. 7.11. The measurement principle was described in detail in section 7.1.3. During magnetic field sweep from 0 to 300 mT the sensitivity of the SET (shown in red) drops considerably. Accordingly, the average signal induced by the BG drops as well. The signal *normalized* by the sensitivity is on average constant. It is proportional to the inverse compressibility $1/\chi$ and is shown in black.

For increasing magnetic fields the inverse compressibility shows peaks. This is expected: The density of states develops LLs that become more separated with increasing B as sketched in the insets (see also section 3.2). When the Fermi energy is between two LLs - or in a minimum of the DOS for overlapping levels - the inverse compressibility is expected to be large. For comparison we show the longitudinal resistance R_{xx} in blue.[4] As expected, the positions of peaks in $1/\chi$ correspond to minima in R_{xx}.

For the particular measurement shown in Fig. 7.11 parameters are as follows:

- BG efficiency: $\partial n/\partial V_{\mathrm{BG}} = 2 \times 10^8/\mathrm{cm}^2\mathrm{V}$
- modulation amplitude on BG: $V_{\mathrm{BG,ac}} = 1.44$ Vpp
- modulation amplitude on 2DES: $V_{\mathrm{2D,ac}} = 200\ \mu$Vpp

Near $B = 0$ where SdH peaks are absent we measure a ratio of BG signal to the SET sensitivity of about 0.1. According to equation 7.7 the inverse compressibility is thus $1/\chi = 7.1 \times 10^{-14}$ eVcm^2. We will comment on this value together with other results in section 7.3.2.

This measurement confirms that we can measure compressibility with the help of SETs. It also underlines the importance of normalizing the BG signal by the sensitivity of the SET as the latter varies during the $B-$sweep. As shown in Figs. 7.9 and 7.10 the sensitivity is further altered when the sample is irradiated with microwaves.

7.3 Results

We first report two unexpected complications: the variations of the microwave intensity near the sample and the variations of the compressibility at zero mag-

[4]The longitudinal resistance is not measured at the same time with the other data: For compressibility measurements no current is driven through the 2DES. Only the dc- and ac-voltages are applied as described above.

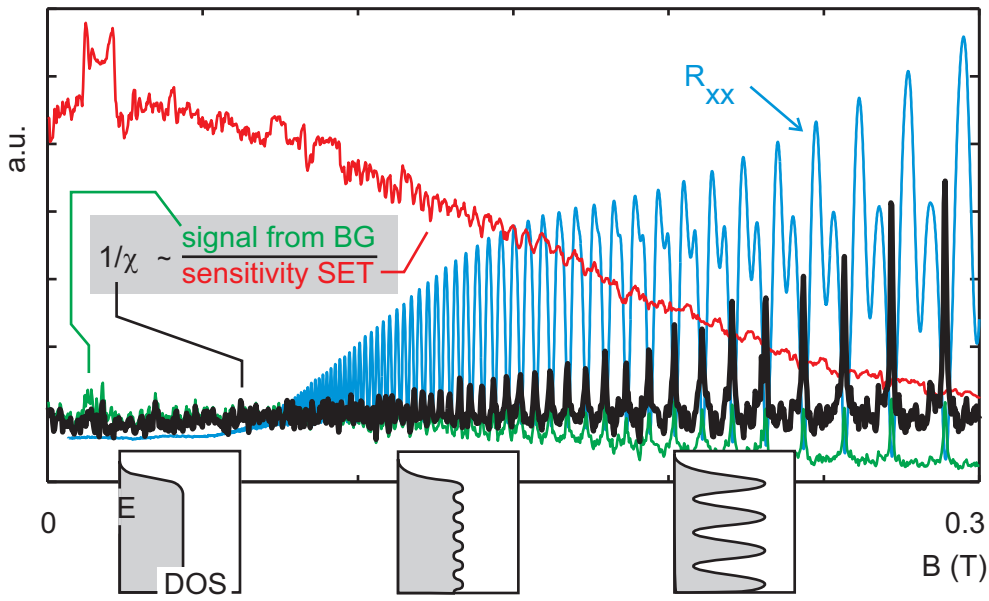

FIGURE 7.11: To verify that we can measure the (inverse) compressibility we show data in the absence of microwaves. A density modulation induced by the BG leads to changes in the chemical potential that are detected by the SET. Normalizing this signal by the SET sensitivity (which is measured in parallel) yields the black trace. This quantity is (proportional to) $1/\chi$. Peaks in the inverse compressibility coincide with minima in R_{xx} as expected.

netic field in the absence of microwaves. These two sections are of a somewhat technical nature. Yet, the implications are important for the interpretation of compressibility measurements which will be presented in section 7.3.3.

7.3.1 Microwave power near the sample: Irregular frequency and position dependence

We address here an issue that hampers all our measurements: The microwave power in the vicinity of the sample. We will show in this section that for a fixed power sent into the sample holder the power reaching the sample varies *strongly* with frequency and position. We have three ways to characterize the power: First, we place a calibrated, commercial power meter near the position of the sample (while the sample holder is on the laboratory table). Second, we use the pronouncedness of MIRO in transport measurements. Last, we use the SETs as they strongly react to microwave radiation. Each of these methods has advantages and drawbacks:

commercial power meter	transport behavior	SET behavior
not in cryostat instead of sample	in cryostat on sample	in cryostat on sample
calibrated sensor averages over 2×4 mm^2	radiation effect unclear averages over Hall bar	radiation effect unclear local

Commercial power meter (sample holder not in cryostat)

We placed a calibrated power sensor at the approximate position of the sample while the sample holder was placed on the laboratory table. The power absorbed in the 2×4 mm^2 opening is measured for frequencies between 50 and 70 GHz at fixed microwave source power.[5] The position of the detector is then shifted by approximately 1 mm within the plane of the imaginary sample and the measurement is repeated. Results are shown as different traces in the top left panel of Fig. 7.12. We find:

- Power depends strongly on frequency. We see variations of up to a factor of 50 or more. Changes are not smooth but abrupt on the frequency scale shown.

- Power distribution is strongly inhomogeneous. Upon changing the detector position some intensity peaks vanish and others arise, for example at 55 or 68 GHz.

We verified that changing the microwave source power by a certain factor only scales the result by the same factor (not shown). The variations along the frequency axis stay exactly the same.

The average power detected near the sample position is roughly 50 times smaller than near the source. This is because not all the radiation leaving the horn is detected in this way and partly because of losses in the waveguide.

We can not assume the measured intensities to be the ones seen by the sample, as the geometry and possible reflection patterns are strongly altered when the chip carrier is replaced by the detector. Also the sample holder itself may deform due to thermal contraction.

[5]We fixed the *generation* power of the BWO source. The output power then slightly changes with frequency. An example is given in the bottom trace of Fig. 7.12. The generation power was here fixed for $50 - 76$ GHz and, using a different BWO, for $75 - 110$ GHz. The source output power varies by a bit more than a factor of two. This is more than an order of magnitude less than variations near the sample. Also variations here are smooth. Therefore we regard the output power as constant for a given generation power. The color code introduced in Fig. 7.8 actually refers to generation power.

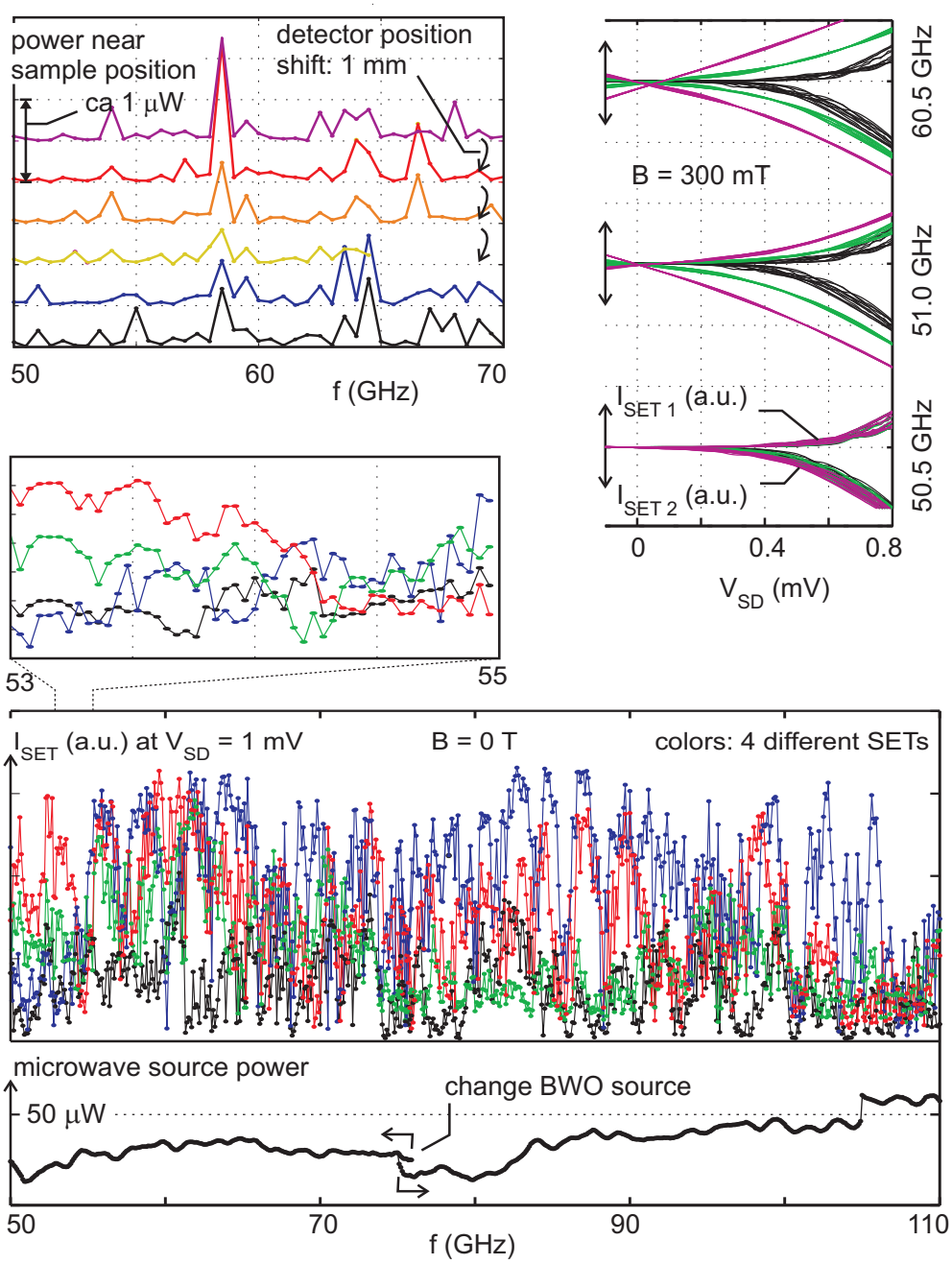

FIGURE 7.12: Top left: Microwave power measured by a commercial power meter. The 2×4 mm opening is placed approximately at the sample position and is shifted between different traces. Right: Comparing $I_{\mathrm{SET}} - V_{\mathrm{SD}}$ characteristics of two SETs for different microwave frequencies and powers (powers indicated by colors as in Fig. 7.8). Bottom panel with magnification: The frequency dependence of I_{SET} at fixed V_{SD} shows erratic variations. No correlations are apparent between SETs. Very bottom trace: Microwave source output power shows only weak frequency dependence.

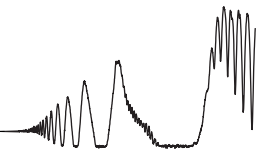

Microwave power and transport behavior

We use the pronouncedness of MIRO to estimate the microwave power. In Fig. 7.13 we show the frequency dependence of MIRO transport data for four fixed microwave source powers. We observe the following:

- Pronouncedness of MIRO shows moderate frequency irregularities.
- Variations can be abrupt on the GHz scale. This supports a sudden redistribution of the radiation field in the vicinity of the sample.
- A saturation effect is observed: Frequency variations are most pronounced for moderate powers and are mostly absent for the highest power shown where the pronouncedness of features has saturated.

We also mention that most of our Hall bars have roughly the same size of 0.4 mm width and 0.4 to 1 mm length. One experiment on a considerably smaller HB (80×100 μm) did show slightly more pronounced frequency variations of MIRO data.

Using MIRO to assess microwave power has the drawback that we do not know a priori how the sample reacts to different powers and especially to spatial intensity variations. It is likely that some sort of averaging over the HB area takes place, but it is for example possible that areas with high power are more important in the averaging than areas with low power. The details of this are unknown.

SET as power meter

We showed in the last section that SETs react strongly to microwave radiation. Here we use this effect to assess the microwave power at the sample. A drawback of using the SETs as power sensors is that we do not know the mechanism by which the radiation influences them. A first guess would be heating but antenna effects of the SET connections may be important.

We find very strong variations in the SETs' reactions to microwaves. This points to a strong frequency dependence and inhomogeneity of the radiation field and is in line with the findings from above.

The top right panel of Fig. 7.12 shows $I_{\mathrm{SET}} - V_{\mathrm{SD}}$ characteristics for two SETs located 20 μm apart on the same Hall bar and measured in parallel (the $y-$axis for the second SET is inverted). Bundles of the same color correspond to traces at various 2DES voltages but fixed microwave source power (powers indicated by colors as in Fig. 7.8). We observe that the microwave induced change in $I_{\mathrm{SET}} - V_{\mathrm{SD}}$ is strongly frequency dependent: At 50.5 GHz traces

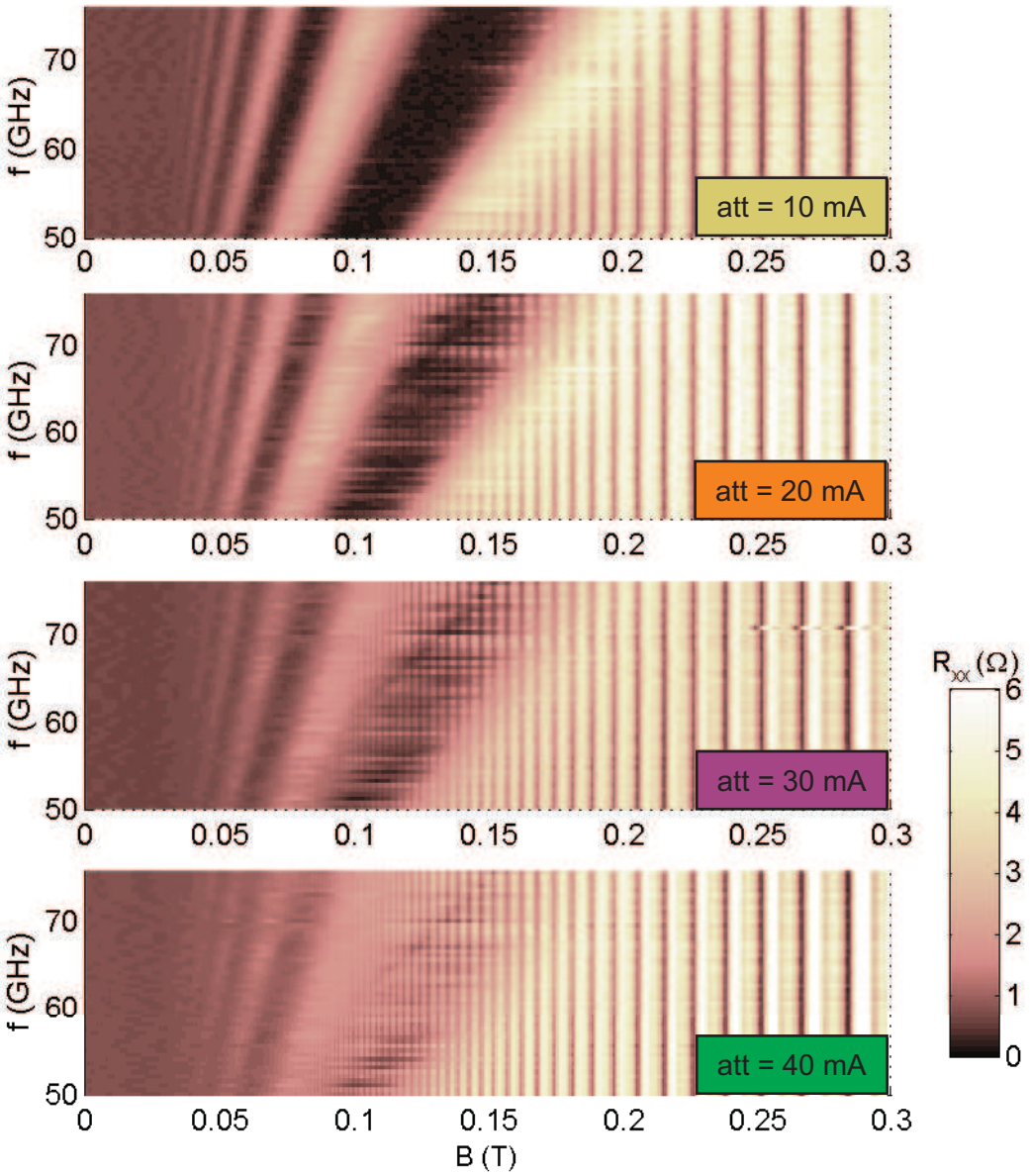

FIGURE 7.13: Longitudinal resistance of a 2DES under microwave irradiation shown as color plots on $f - B$ axes for different microwave source powers. (Powers are decreased by roughly a factor of 4.5 between graphs from top to bottom. Powers indicated by colors as in Fig. 7.8.) Variations in the pronouncedness of MIRO indicate that the power near the sample changes irregularly with frequency. The irregularities are moderate compared with local SET measurements (see below).

look similar to the absence of microwaves (black), whereas at 51 GHz they are strongly affected. Furthermore, the two SETs respond differently for different frequencies: At 51 GHz the change in SET 2 is much stronger than SET 1 while at 60.5 GHz both are affected approximately equally.

We use SETs as local power sensors more efficiently by measuring the change in current I_{SET} at *fixed* source-drain voltage. The lower panel of Fig. 7.12 shows the frequency dependence of I_{SET} from four SETs distributed unequally over the sample width of 0.4 mm. The results are erratic but completely reproducible. We find

- strong irregularities in the frequency dependence, becoming smooth only on the sub-GHz scale (see magnification),
- no apparent correlation is seen between different SETs.

Conclusions on microwave power variations

We present our conclusion on the above findings here as it is important for the following compressibility measurements: *Microwave power near the sample varies strongly as a function of both position and frequency.* Surprisingly large variations are observed using methods with spatial averaging (commercial detector and transport data). Local SET measurements indicate even stronger variations. Antenna effects may be involved in the SETs but they can not explain the variations observed with the other two methods.

7.3.2 Irregularities in compressibility near $B = 0$ without microwaves

We need to address another issue before interpreting compressibility measurements under microwave irradiation: The (inverse) compressibility at zero magnetic field in the absence of microwaves $1/\chi(B, p = 0)$. We find that it shows considerable variations among different SETs and especially among different samples (though all from the same heterostructure).

We mentioned in section 2.1 that the inverse compressibility in the single particle picture (sp) is the same as the inverse DOS. For GaAs this is

$$1/\chi_{\mathrm{sp}} = \frac{\pi\hbar^2}{m^*} = 3.58 \times 10^{-14}\ \mathrm{eVcm}^2. \tag{7.8}$$

Taking electron-electron interactions into account modifies this result. In Hartree-

Fock approximation one finds [136]

$$1/\chi_{\mathrm{HF}} = \frac{\pi\hbar^2}{m^*} - \sqrt{\frac{2}{\pi}}\frac{e^2}{4\pi\varepsilon\varepsilon_0}\frac{1}{\sqrt{n}} \tag{7.9}$$

which becomes negative at a critical electron density $n_{\mathrm{c,HF}} = 6.4 \times 10^{10}/\mathrm{cm}^2$. The sign change has been observed in experiment (for example [137,138]). The samples we used for MICRO measurements do not have an in-situ grown BG and thus we can not tune the density over a wide range. We did use one sample with a BG (that, however, showed no response to microwaves) and indeed could observe the sign change in the inverse compressibility at a critical density of $n_c = 1.6 \times 10^{11}/\mathrm{cm}^2$. This agrees reasonably well with $n_c = 1.1 \times 10^{11}/\mathrm{cm}^2$ from Ref. [138].[6] Our compressibility measurements are done at $n = 2.1 \times 10^{11}/\mathrm{cm}^2$, so we are safely in the regime where $1/\chi > 0$.

Table 7.1 gives an overview over parameters of samples we used for compressibility measurements. Listed are also the SETs we used on each sample together with the $1/\chi(B, p = 0)$ values measured by these SETs. Two findings are striking:

- Variations in $1/\chi(B, p = 0)$ are huge. SETs on the same sample tend to have similar values.
- Values of $1/\chi(B, p = 0)$ are too large.

With the latter we mean that $1/\chi(B, p = 0)$ should be *smaller* than the value given in equation 7.8 because electron-electron interactions reduce the result. With no exception we observe *larger* values. We currently have no explanation for this result. We speculate about two possible reasons:

First, it is known that disorder can locally modify the global DOS: Disorder induced density variations lead, together with a density dependent compressibility, to spatial variations in the compressibility. Also, localized states may get charged in a Coulomb dominated way [42,137].[7] Similar effects may explain spatial variations in $1/\chi$. Yet, one would not expect to find only larger values.

[6] Equation 7.9 assumes an infinitely thin 2DES. The finite width of the wavefunction, as also discussed in Ref. [136], adds two effects: On the one hand the finite widh-softening of the Coulomb interaction tends to reduce the negative correction due to interactions. On the other hand Stark like shifts of energy levels can make the compressibility more negative. The latter seems to dominate both in Ref. [138] as well as our own measurements.

[7] We note that in the 2DES' metallic regime the charging effects refer to localized states *not* in the 2DES but for example in the doping layer [137]. However, for the effect on the SET these two cases are equivalent.

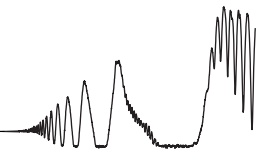

sample	$\partial n/\partial V_{\mathrm{BG}}$ [$10^8/\mathrm{cm}^2\mathrm{V}$]	MIRO [quality]	MICRO [quality]	SET [pins]	$1/\chi(B, p=0)$ [10^{-14} eVcm^2]
307-01-l	2.0	good	weird	12-17	7
				13-15	6
307-01-lur	2.2	good	bad	15-11	6
				14-12	7
				16-10	10
				13-08	11
307-03-l	6.0	poor	none	13-11	1
307-03-lr	2.0	good	bad	11-12	444
307-04-r	1.7	ok	none	01-22	294
				12-16	611
				11-14	82
				13-15	350
307-01-l-2	1.9	good	good	21-24	7
				13-11	7
307-05-r	2.6	ok	bad	16-14	61
				01-02	17
				11-12	12

TABLE 7.1: Overview over relevant samples, their BG efficiency, pronouncedness of MIRO transport data, pronouncedness of microwave-induced compressibility oscillations (MICRO), used SETs (named by bonding pins) and the inverse compressibility measured by these SETs at zero magnetic field in the absence of microwaves. All samples are from the same wafer and have an equilibrium density of $2.1 \times 10^{11}/\mathrm{cm}^2$. For sample 307-01-l, "weird" MICRO refers to a behavior different from all others, see section 7.3.3.

Second, it may be important that we use the chipcarrier as a BG. In fact, on one sample from a different heterostructure with an in-situ grown BG we observed a "reasonable" value for $1/\chi(B, p=0)$ of about 1.6×10^{-14} eVcm^2 at the equilibrium density of $2.3 \times 10^{11}/\mathrm{cm}^2$. This wafer, however, showed no response to microwaves. Another finding points in the same direction: For the wafer we used for MICRO the quantity $\partial n/\partial V_{\mathrm{BG}}$ varies between different Hall bars (see table 7.1). This indicates that the chipcarrier as BG does not behave like a clean plate parallel to the 2DES. The induced density changes may locally be larger than we assume from analyzing transport data. This is supported by the anomalous density dependence in the SdH oscillations (see Fig. 7.8) that we observe on all Hall bars from this wafer. Yet, one would expect to find larger and smaller values of $1/\chi(B, p=0)$, not only too large ones.

We also compared the values of $1/\chi(B, p=0)$ to the compressibility peaks

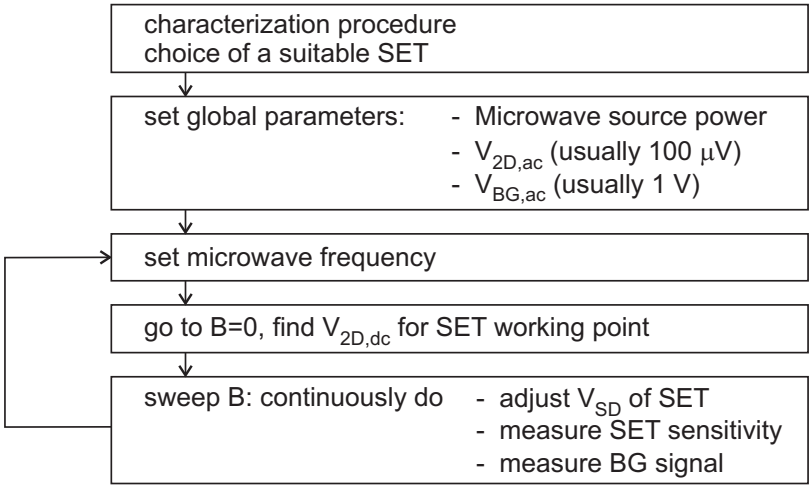

FIGURE 7.14: Measurement procedure used for most compressibility measurements.

due to SdH oscillations (still in the absence of microwaves). Due to little statistics and different reactions of the SETs to magnetic fields we can draw no quantitative conclusions. Qualitatively, the large scatter in $1/\chi(B, p = 0)$ is also reflected in the SdH regime (i.e. for a 100 times larger value of $1/\chi(B, p = 0)$ the SdH peaks are not invisibly small oscillations but rather scale up as well).

Due to the large variations and the "wrong" values of $1/\chi(B, p = 0)$ subsequent measurements of $1/\chi$ in non-zero B and under microwave irradiation cannot be interpreted quantitatively. We will focus on changes induced by the radiation, not on numbers.

7.3.3 Results on compressibility under microwave irradiation

In this section we present our results on the compressibility of a 2DES under microwave irradiation. Unless otherwise stated the displayed data are from sample 307-01-l-2 because it showed the best results (see table 7.1). We first describe the measurement scheme and give some examples. Then we present systematic results on frequency dependence and radiation power dependence. A measurement of the electron density dependence in a very limited density range is given in the appendix. Last we address the observed variations between different samples. Data analysis and discussion is postponed to the next section.

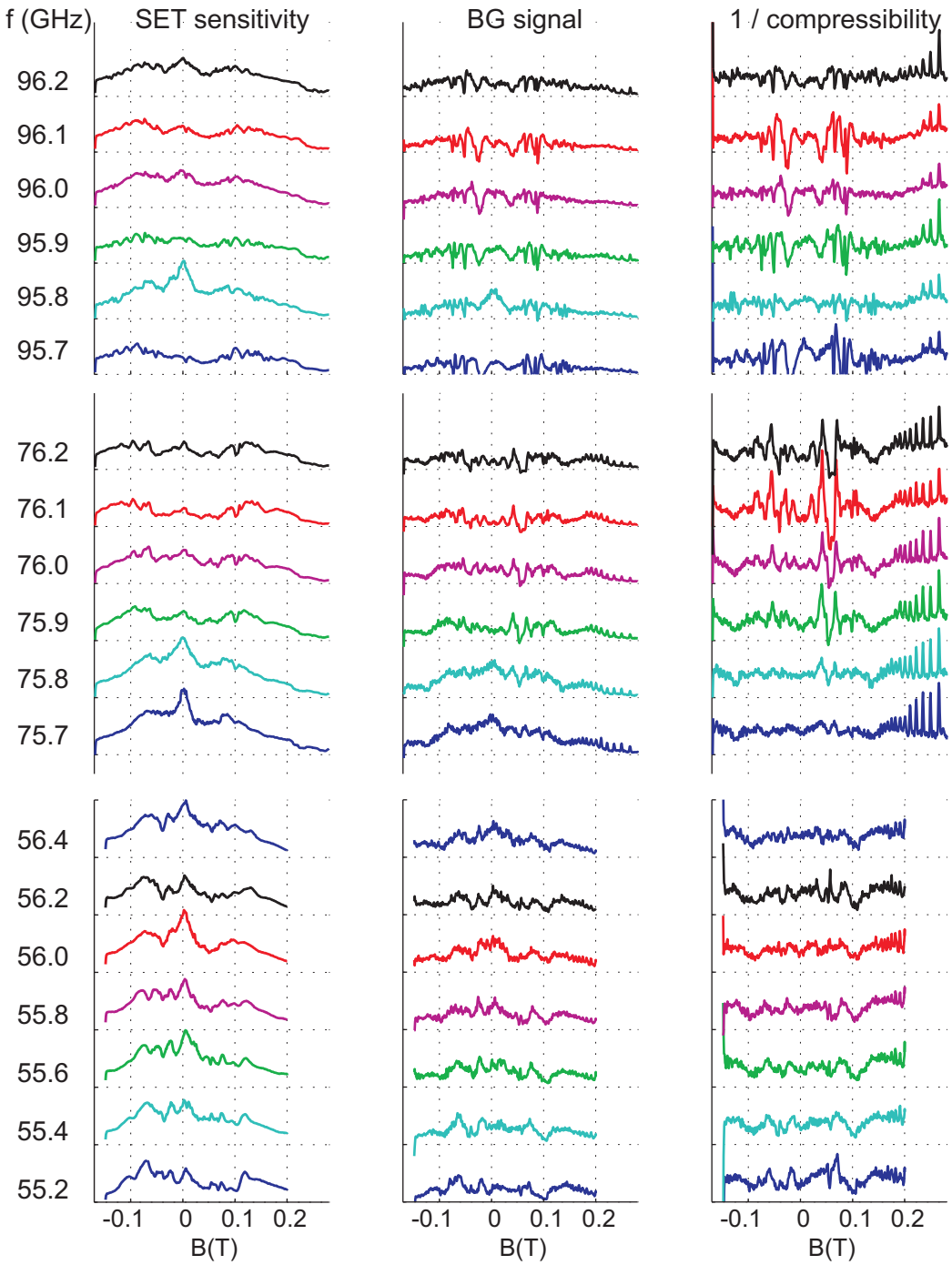

FIGURE 7.15: Exemplary measurements of the inverse compressibility for selected frequencies. Dividing the BG signal (middle column) by the SET sensitivity (left) we obtain the result which is proportional to $1/\chi$. Traces are offset, units are arbitrary. Microwave source power corresponds to the green trace in Fig. 7.8.

Measurement scheme and examples

It turns out that often $1/\chi$ as a function of magnetic field shows large fluctuations. A single trace is hardly interpretable. To identify effects of microwave irradiation we need to systematically investigate the frequency dependence. The measurement scheme is illustrated in Fig. 7.14.

Figure 7.15 shows exemplary traces of the two measurement quantities (the SET sensitivity and the BG signal) as well as their ratio signal/sensitivity which is proportional to $1/\chi$. Examples are taken in the vicinity of three different frequencies, namely $f = \omega/2\pi = 56, 76$ and 96 GHz. We observe the following:

- A single trace shows rather large fluctuations. These are mostly due to plasmons as we will see below.
- Fluctuations tend to become more pronounced with increasing frequency. $1/\chi$ can become negative.
- Changes in frequency on the sub-GHz scale can alter $1/\chi$ considerably.
- At larger magnetic fields, when $\omega < \omega_c$, no or little effect of microwaves is seen and SdH peaks take over. Fluctuations are mostly absent.

Frequency dependence of $1/\chi$

We will in the following present color plots of $1/\chi$ on $f - B$ axes. Figure 7.16 shows covered frequency range from 50 to 110 GHz.[8] Due to the reasons described in section 7.3.2 we do not give absolute values for $1/\chi$. The colorbar indicates low and high values. We refer to Fig. 7.15 to compare the amplitude of typical microwave induced effects to the dark values. Three types of structures can be identified (see also right page of Fig. 7.16):

1. At $\omega \gtrsim \omega_c$ SdH peaks are seen. Here the inverse compressibility is not altered by the microwave irradiation.
2. Curved structures start at $B = 0$ and asymptotically approach $\omega = \omega_c$. This suggests the involvement magnetoplasmons.

[8] There is a slight discontinuity at 75 GHz. This is because the magnetic field depends slightly on the sweep history of the magnet. At $f > 75$ GHz a different B-range is covered which results in slightly different actual magnetic fields at the same nominal values. Also, a tiny shift of the entire picture to positive B is seen, which has the same origin.

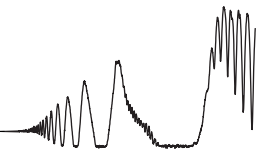

3. Fan like structures can be seen running along $\omega = (i + \phi_i)\omega_c$ for $i = 1, 2, 3, \ldots$ with a phase ϕ. These are the sought for microwave induced compressibility oscillations (MICRO).[9]

Features 1. and 3. are reminiscent of MIRO transport data (Fig. 7.13) while feature 2. is entirely absent in transport. Features 2. and 3. are induced by the microwave irradiation. They suppress the SdH peaks up to $\omega \approx \omega_c$. In the following we give details on these different types of features.

Magnetoplasmon signatures in $1/\chi$

Plasmons are collective excitations of the electronic system. The spectrum depends on the sample dimensions. For a 2DES with electron density n the plasma frequency $f_p = \omega_p/2\pi$ is given by

$$\omega_p^2 = \frac{ne^2}{2\varepsilon\varepsilon_0 m^*}k \tag{7.10}$$

where $\varepsilon = 6.9$ is the mean of the vacuum and GaAs dielectric constants and $k = 2\pi/\lambda$ is the wavevector of the plasma oscillation (see [139, 140] for reviews on 2D plasmons). A finite geometry imposes restrictions on the wavevectors: Integer multiples of half of the wavelength must fit into the sample dimensions L_x and L_y. This corresponds to $k_{x,y} = i_{x,y}\pi/L_{x,y}$ with $i_{x,y} = 1, 2, 3, \ldots$ and $k = \sqrt{k_x^2 + k_y^2}$.

In a magnetic field the plasma oscillations hybridize with the cyclotron frequency.[10] The resulting magnetoplasmon spectrum is (numbers are for GaAs)

$$\omega_{mp} = \sqrt{\omega_p^2 + \omega_c^2} \tag{7.12}$$

$$f_{mp}[\mathrm{GHz}] = f_p\sqrt{1 + 17.4\left(\frac{B[\mathrm{T}]}{f_p[100\ \mathrm{GHz}]}\right)^2} \tag{7.13}$$

[9] We use the term MICRO (microwave induced compressibility oscillations) only for features in $1/\chi$ that are periodic in $1/B$ and proportional to the microwave frequency. The magnetoplasmon signatures are not meant, even though they are induced by microwaves as well.

[10] We here treat only bulk magnetoplasmons. A second branch describes edge-magnetoplasmons that propagate along the sample edge. Their frequency drops with increasing B and is, for $\omega_c \gg \omega_p$ proportional to $1/B$. Both branches can be described by (assuming circular geometry)

$$\omega_\pm = \sqrt{\omega_p^2 + (\omega_c/2)^2} \pm (\omega_c/2) \tag{7.11}$$

See for example Ref. [141] for a review. In our data we do not observe edge magnetoplasmons.

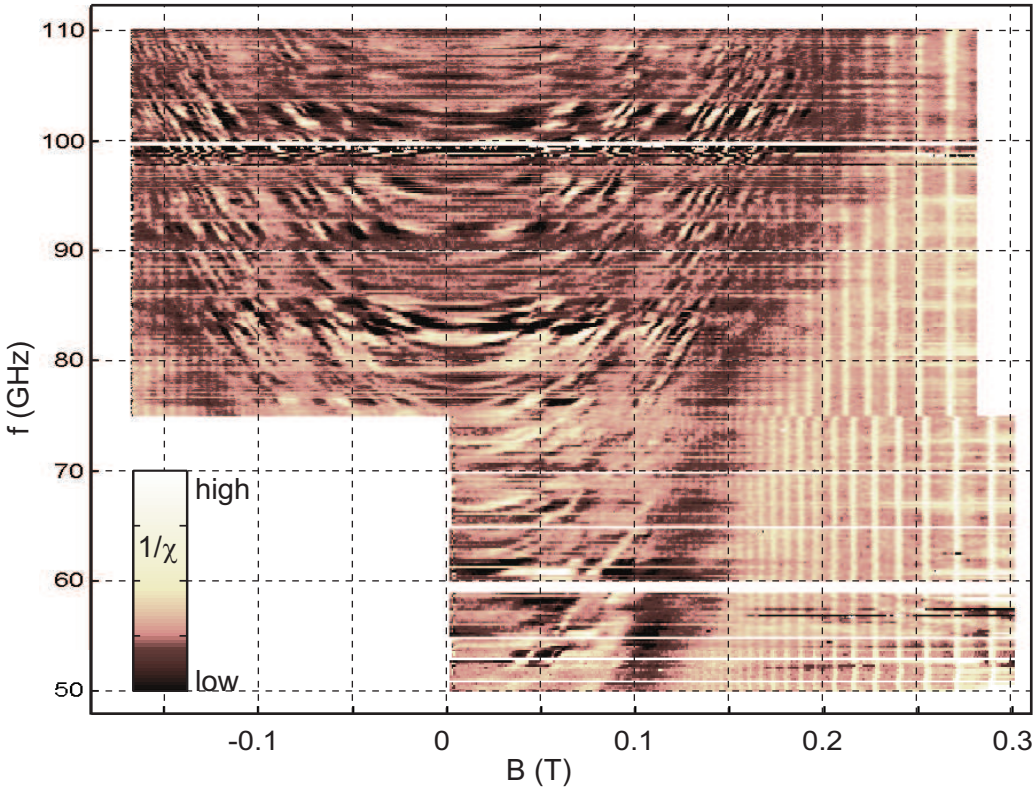

FIGURE 7.16: Inverse compressibility of a 2DES under microwave irradiation shown as a color plot on $f - B$ axes. One minimum in $1/\chi$ following $\omega = (i + \phi_i)\omega_c$ can be clearly be observed for $i = 1$. Two more are harder to see but can be identified by data averaging (see Fig. 7.20). Furthermore, SdH peaks are identified as vertical lines and curved lines indicate the presence of magnetoplasmons. See footnote 8 for the discontinuity at 75 GHz and the offset in B of 5 mT. The microwave source power is between the green and the pink trace in Fig. 7.8.

Right page: The same data overlayed with the three types of structures that can be identified: 1.: Peaks in the inverse compressibility are observed where the longitudinal resistance has a minimum (SdH oscillations). 2.: Magnetoplasmon structures are observed. Black lines are hybridizations according to equation 7.13 of ω_c and exemplary values of ω_p, namely 50, 67, 75, 82 and 92 GHz. 3.: Fan like MICRO minima in $1/\chi$ are highlighted in green, multiples of ω_c in blue.

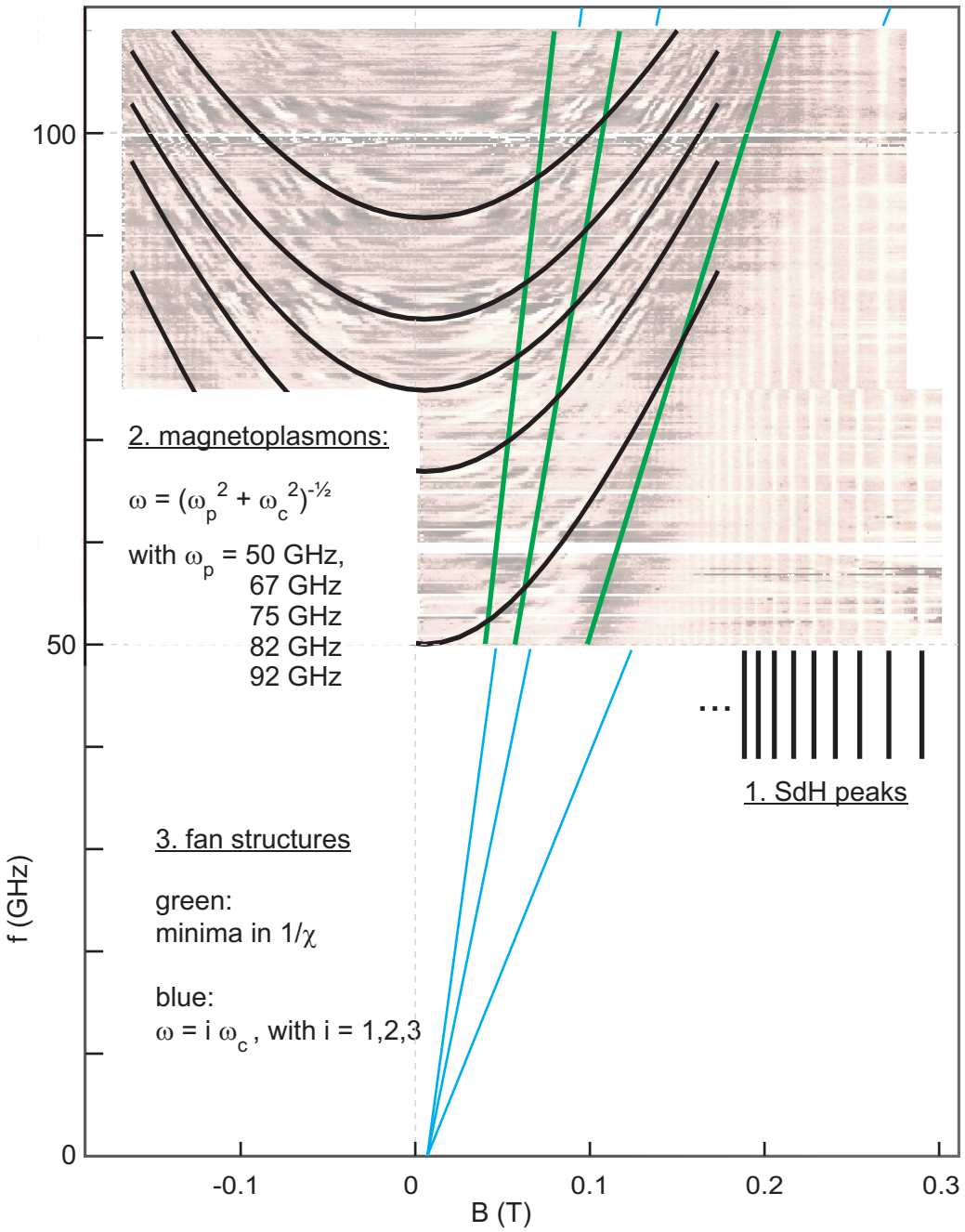
100
50
0
f (GHz)
-0.1
0
0.1
0.2
0.3
B (T)
2. magnetoplasmons:
ω = (ω_p^2 + ω_c^2)^-½
with ω_p = 50 GHz,
67 GHz
75 GHz
82 GHz
92 GHz
1. SdH peaks
3. fan structures
green:
minima in 1/χ
blue:
ω = i ω_c , with i = 1,2,3

Magnetoplasmon structures are clearly observed in our compressibility data. The black lines in Fig 7.16 are plotted from the above equation for exemplary frequencies ω_p which are chosen arbitrarily to run along prominent features in the data. For such fixed ω_p the $B-$dependence of ω_{mp} fits almost perfectly to the observed structures. We emphasize that no free parameter is involved here. Even though clearly identified, the magnetoplasmon signatures are interrupted in an irregular way. We suspect that this is due to the interplay with other features in the inverse compressibility, namely the $1/B$ periodic MICRO. However, it seems that this is not sufficient to explain the erratic structure in the magnetoplasmon data.

The Hall bar on which the data from Fig 7.16 was taken has dimensions of $L_x = 0.4, \quad L_y = 2.0$ mm. This corresponds to minimum plasmon frequencies $f_x = 38, \quad f_y = 17$ GHz. It is not surprising that we observe many plasmon lines because the number of allowed modes per frequency interval increases quickly for frequencies larger than the fundamental one. 50 GHz corresponds to $\lambda/2 = 231$ μm, 100 GHz to $\lambda/2 = 58$ μm. We also note that the plasmon features in our data are often stronger in amplitude than MICRO and can yield negative values of $1/\chi$ (see Fig. 7.15).

As mentioned, plasmons are collective excitations. In that sense it is not surprising that they are reflected in thermodynamic quantities like the compressibility, even though we ignore the physical mechanism that relates the two quantities. Moreover, it is possible that we measure not a magnetoplasmon induced change of the compressibility but rather pick up electric fields associated with magnetoplasmons.

MICRO signatures in $1/\chi$

The predicted MICRO are $1/B$ periodic and proportional to the microwave frequency. These structures are indeed observed. In Fig 7.16 green lines indicate minima in $1/\chi$. The first order minimum is clearly seen. Higher oder minima are strongly disturbed by magnetoplasmon signatures but can be identified (it helps to look at Fig 7.16 from a shallow angle along the suspected lines ;-). The influence of magnetoplasmons is reduced for lower microwave power and MICRO can be identified better (see Fig 7.17). By an averaging procedure described in section 7.4 MICRO can be unambiguously identified.

One could argue that the first order minimum $1/\chi$ is not a signature of predicted MICRO but instead is related to the accumulation of magnetoplasmon resonances that all approach $\omega = \omega_c$. The observation of higher order oscillations that *cross* the magnetoplasmon features allows us to safely discard this possibility.

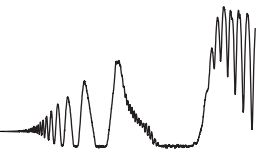

In Fig 7.16 we also indicate as blue lines the condition $\omega = i\ \omega_c$ for $i = 1, 2, 3$. Minima in $1/\chi$ are found at microwave frequencies slightly larger than multiples of ω_c. As we will see in section 7.4 they coincide with minima in transport data.

Power dependence of $1/\chi$

Figure 7.17 shows the inverse compressibility under microwave irradiation for three fixed microwave source powers. The microwave induced structures get more pronounced with increasing power. Fan-like MICRO structures are best identified in the top panel with least power. Here these structures are very weak, but also the disturbance by magnetoplasmon signatures is minimized.

Variations between different samples

As indicated in table 7.1 only few samples show appreciable compressibility response to irradiation. In the top panel of Fig. 7.18 we show an example from 307-01-lur. This is typical for the most pronounced effect of microwave irradiation on a sample other than 307-01-l-2, which was used for most of the shown data. The structure at $\omega \approx \omega_c$ can be identified. However, higher order MICRO are absent or very weak and also magnetoplasmon signatures are much less pronounced.

We also mention an exceptional example: the bottom panel of Fig. 7.18 shows data from sample 307-01-l where the inverse compressibility at zero magnetic field is strongly changed from its dark value. The power dependence of $1/\chi$ on this sample is displayed in Fig. 7.19 for a fixed frequency. With increasing power negative values are observed and MICRO become huge in relation to the SdH peaks (compare this to Fig. 7.15 where MICRO and SdH peaks are of similar amplitude). Eventually, the compressibility near $B = 0$ rises also. Surprisingly, this behavior was observed on a sample from the same wafer as all other data. However, we could not reproduce this exceptional behavior. This exceptional sample is the best in the sense that up to five MICRO are clearly pronounced.

7.4 Data analysis and discussion

The experimental results described in the last section are discussed here. First, we perform a data averaging technique in order to bring out MICRO more clearly and to distinguish them from SdH oscillations, plasmonic effects and noise. Then we compare the locally measured compressibility data with global transport data. The minima in both quantities are found to coincide. We discuss

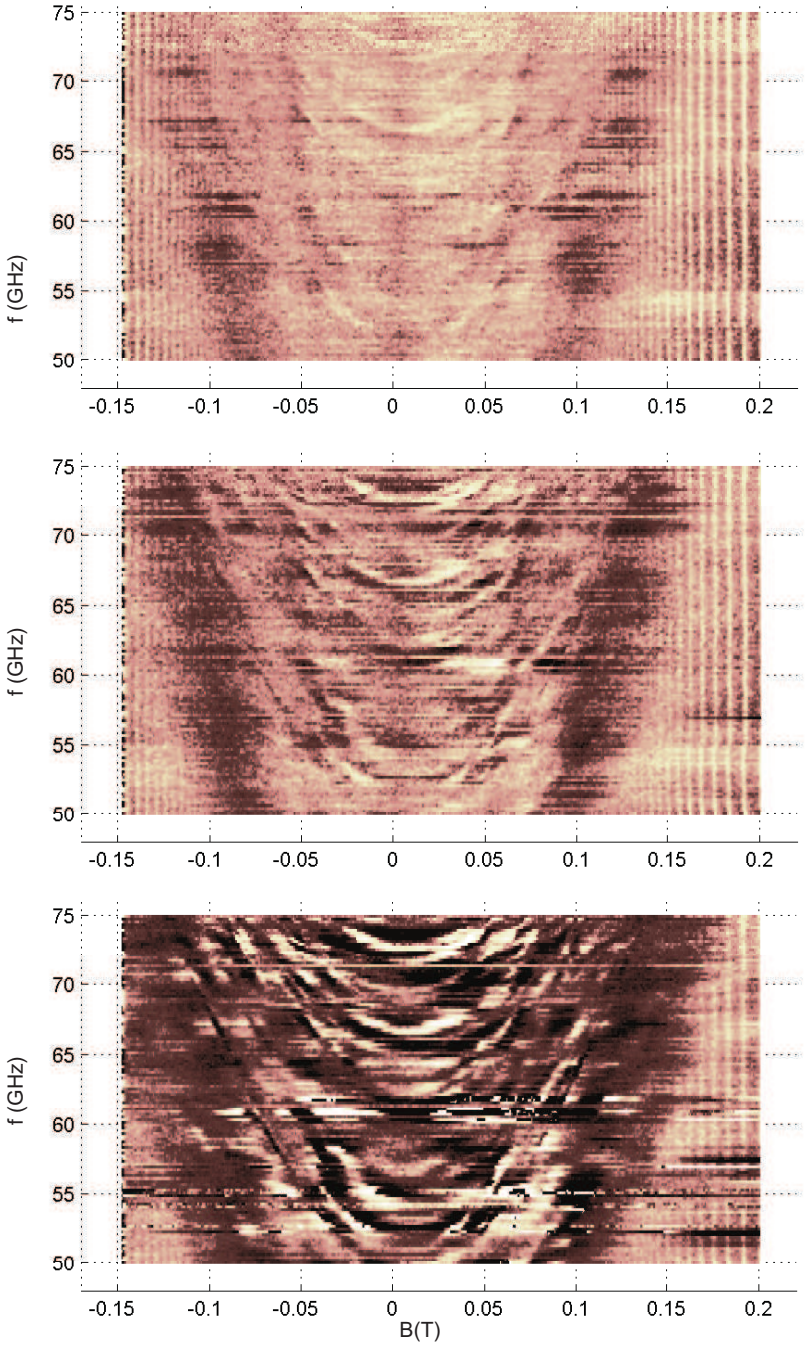

FIGURE 7.17: Power dependence of inverse compressibility. The source output powers are increased by a factor 4.4 between graphs and correspond to the blue, the green and the pink trace in Fig. 7.8.

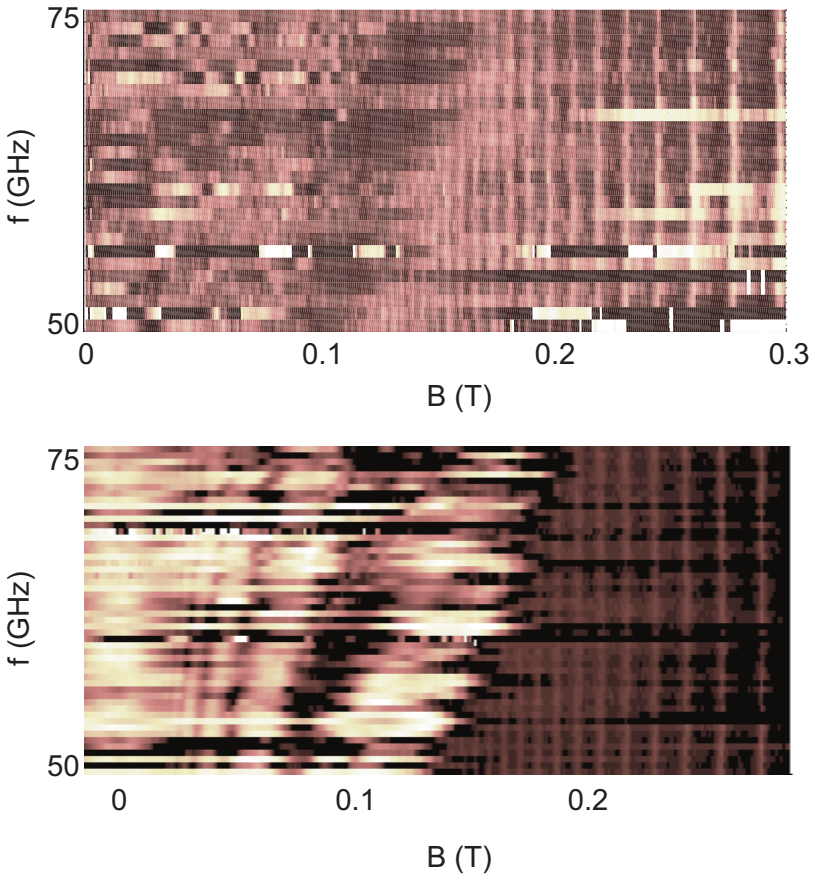

FIGURE 7.18: Examples for the variations of $1/\chi$ among different samples from the same wafer. Top: Typical example from the "second best" Hall bar. Bottom: Exceptional example: Here $1/\chi$ is strongly affected also near $B = 0$.

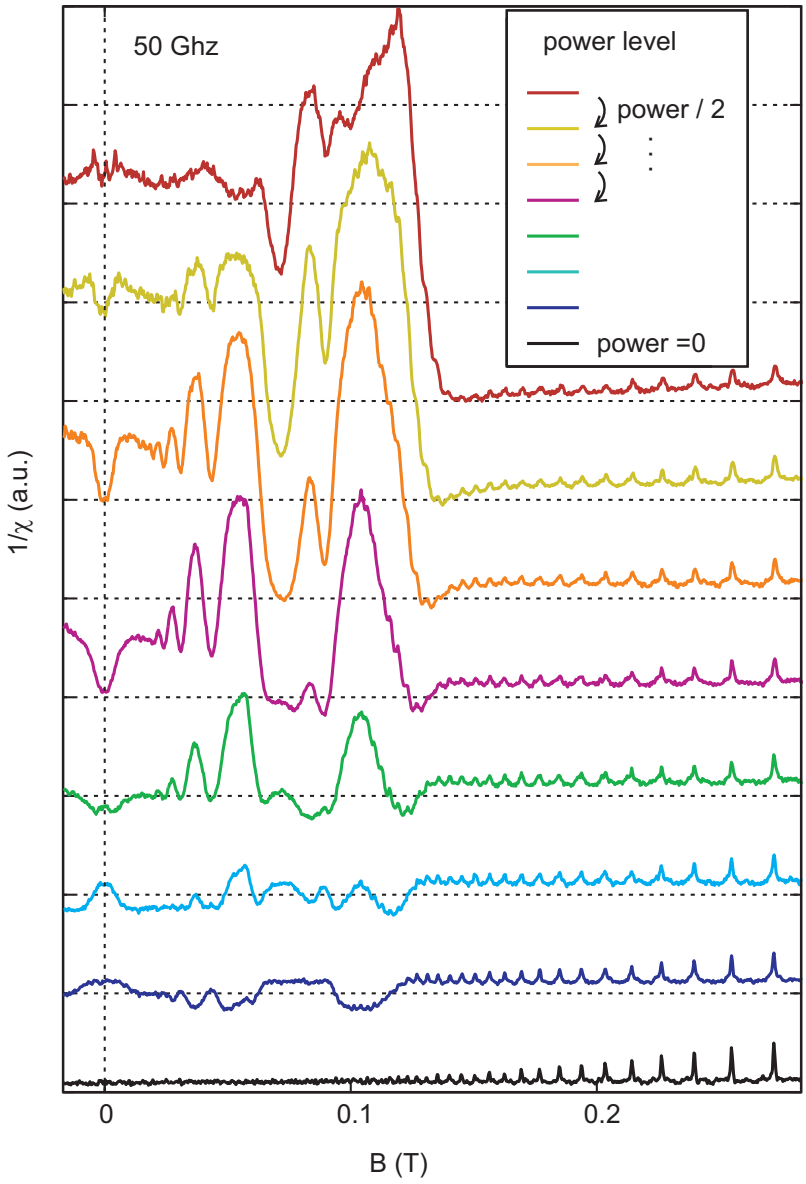

FIGURE 7.19: Power dependence of $1/\chi$ in an exceptional, never reproduced case. (Same sample as bottom panel of Fig. 7.18)

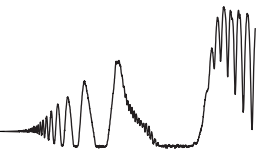

to what extent our findings can be compared to the theoretical predictions. Finally we describe possible future experiments.

7.4.1 Data averaging to highlight MICRO

In order to highlight MICRO in our data we perform a frequency dependent rescaling of the B axis such that $\omega = \omega_c$ is always at a fixed value on the $x-$axis. The scaling relation is given on the left page in Fig. 7.20. A rescaled version of a typical $1/\chi$ dataset is shown. We chose the data from the top panel of Fig. 7.17 which were taken at comparatively low microwave power. Features proportional to the microwave frequency show up as vertical structures, SdH peaks are curved.

We average the rescaled $1/\chi$ values over certain frequency intervals. The results are shown as black lines on the left page in Fig. 7.20 and the averaging intervals are given. Shown in blue are typical not averaged traces from within the interval. The averaging suppresses SdH and plasmon signatures and highlights MICRO. Averaging over $50 - 75$ GHz brings out 4 MICRO.

A dip is observed in $1/\chi$ at $B = 0$. We also observe a slight asymmetry that we attribute to incorrect values of the magnetic field due to trapped flux. (Actually, the data shown here were shifted by -6 mT on the $B-$axis such that the dip is found at $B = 0$. Even though we ignore the physical origin of the dip there is a priori no reason for asymmetry. See also footnote 8 for this issue.)

7.4.2 Comparison of compressibility and transport data

For comparison, we perform the previously described averaging procedure also for transport data as shown on the right page in the top panel of Fig. 7.20. Averaging over $50 - 75$ GHz yields the red trace shown in the bottom panel. Six oscillations can be seen. The transport data used in Fig. 7.20 was taken at a microwave source power which is comparatively low for a transport measurement (green trace in Fig. 7.8). The compressibility data used for the averaging were taken at even lower power (blue trace in Fig. 7.8).

Comparing the pronouncedness of MIRO and MICRO

The number of oscillations brought out by the averaging is comparable for MIRO and MICRO. We thus speculate that, along with oscillations in transport, also $1/\chi$ would show more pronounced oscillations if we could perform the measurements at higher microwave powers. We are here limited by the SETs that tolerate only small amounts of microwave power and by the magnetoplasmon signatures that overwhelm all other features.

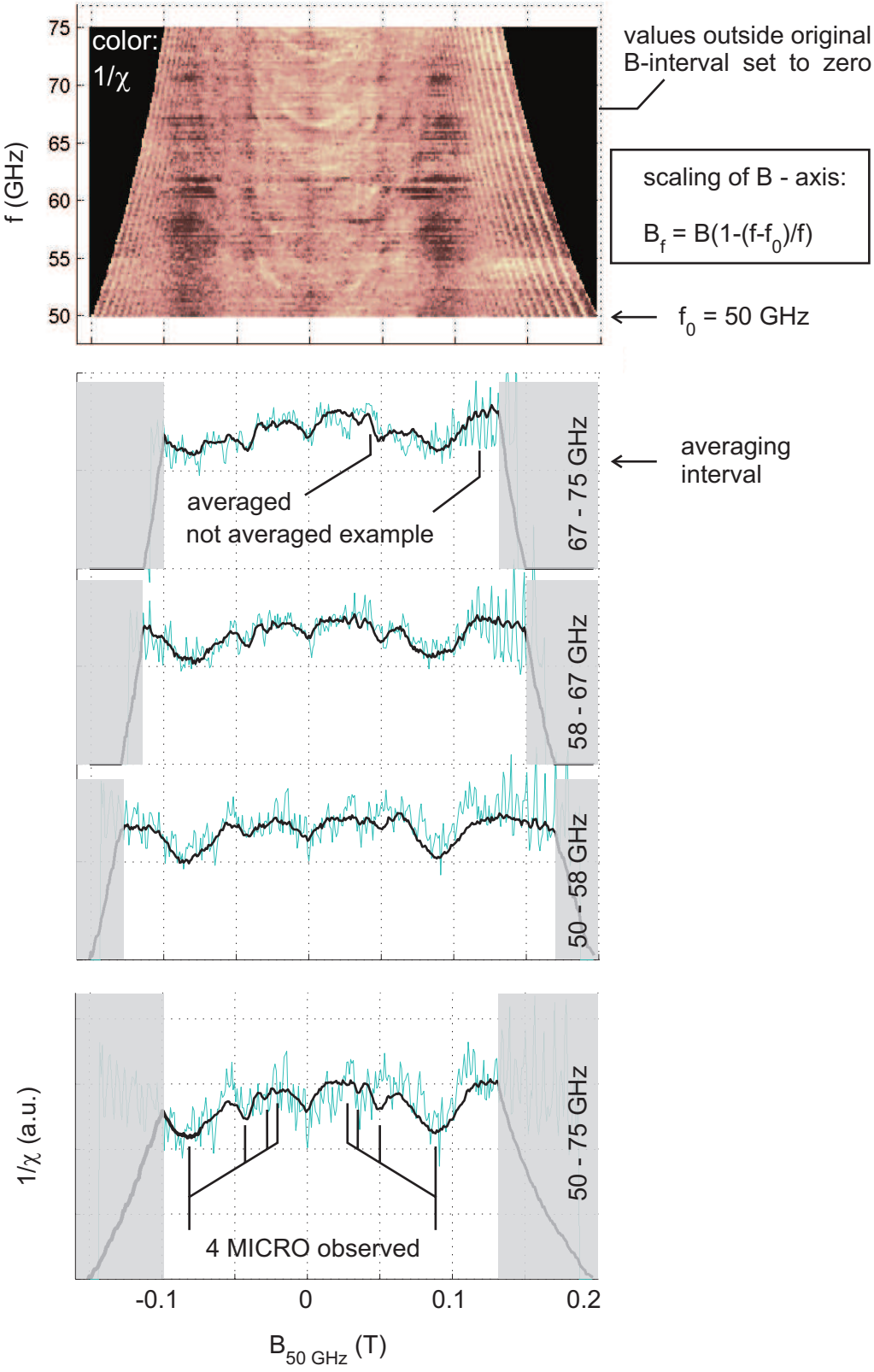
color:
1/χ
f (GHz)
75
70
65
60
55
50
values outside original B-interval set to zero
scaling of B - axis:
$B_f = B(1-(f-f_0)/f)$
f_0 = 50 GHz
averaging interval
averaged
not averaged example
67 - 75 GHz
58 - 67 GHz
50 - 58 GHz
50 - 75 GHz
4 MICRO observed
1/χ (a.u.)
-0.1
0
0.1
0.2
$B_{50\ GHz}$ (T)

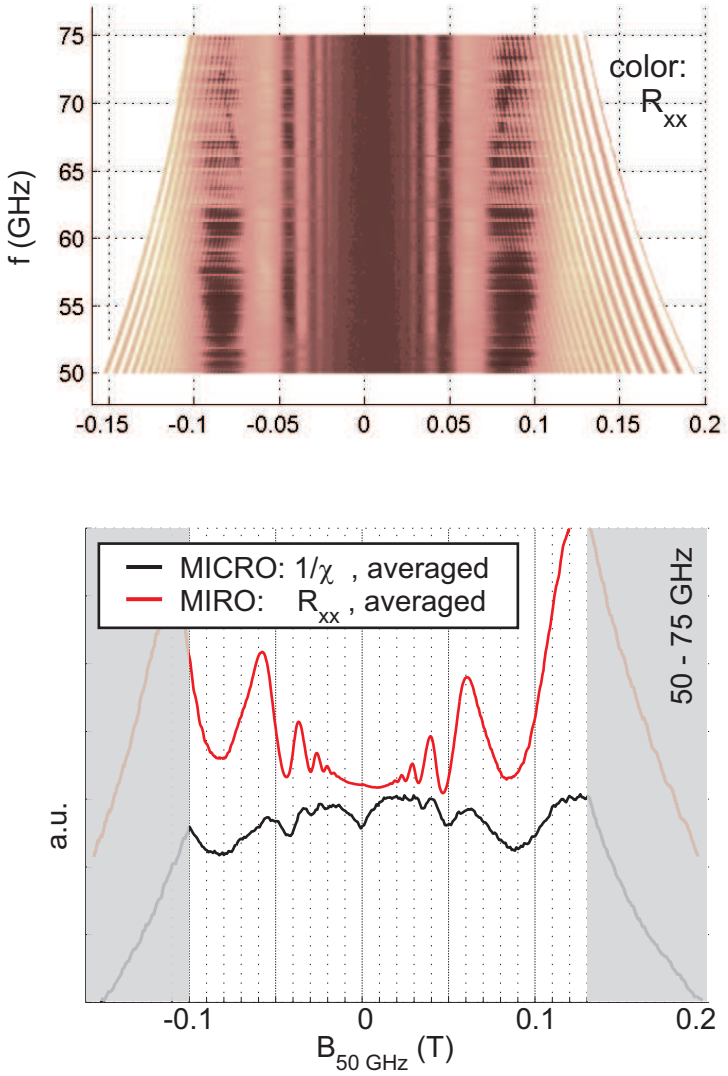

FIGURE 7.20: Left page: Top: Frequency dependent rescaling of $1/\chi$ data shows features that are proportional to f as vertical structures. Below: Frequency averaging (black traces) suppresses SdH and magnetoplasmon signatures and highlights MICRO compared to single not averaged traces (blue).

This page: Top: Frequency dependent rescaling of transport data. Bottom: Comparison of transport (offset) and $1/\chi$ data, both averaged. MIRO are more pronounced than MICRO, but the number of oscillations is comparable. Minima in R_{xx} and $1/\chi$ coincide within experimental uncertainty (see text).

Comparing the irregularities of MIRO and MICRO

The microwave power in the vicinity of the sample was found to exhibit strong variations as a function of position and microwave frequency. This is for example apparent in the very pronounced irregularities in the SET behavior under irradiation (see section 7.3.1). We here address the question to what extent these irregularities are present in the compressibility that is measured by those SETs.

The observed frequency irregularities are much stronger in $1/\chi$ than in transport. However, we estimate for example from Fig. 7.20 that a large part of the irregularities are due to magnetoplasmon resonances. This claim is supported by measuring in parallel with two SETs located 20 μm apart. We found that even though the two SETs react *differently* to the same settings of microwave source power and frequency, they measure very *similar* values of $1/\chi$. We note, however, that this measurement was performed on sample 307-01-l that showed exceptional behavior (see section 7.3.3).

This may indicate that, even though we perform local measurements, the measured values of $1/\chi$ reflect properties of the 2DES averaged over a certain characteristic length scale. For the moment we can not quantitatively compare the averaging length scales of MIRO and MICRO. More experiments are needed here and the role of the local perturbation of the SET, present in the MICRO but not in the MIRO measurements, would have to be taken into account.

Comparing the $B-$dependence of MIRO and MICRO: Minima coincide

Figure 7.21 shows compressibility data under microwave irradiation together with transport data for selected frequencies in order to identify the relative $B-$position of minima in MIRO and MICRO. The first order minimum in both types of oscillations clearly coincide. Also the higher order minima coincide as far as higher MICRO can be identified. The virtually perfect match of SdH-minima in R_{xx} and maxima in $1/\chi$ indicates that no substantial $B-$offset is present.

To further assess the relative position of MIRO and MICRO we revert to the averaging technique described in the last section. The bottom panel of Fig. 7.20 compares frequency averaged transport and compressibility data. The first and second order minima of both types clearly coincide. For higher order features we suffer from imprecise magnetic field values due to trapped flux in the magnet resulting in sweep history dependence. (See above for this issue.) We estimate that within experimental uncertainty also higher order minima of MIRO and MICRO coincide.

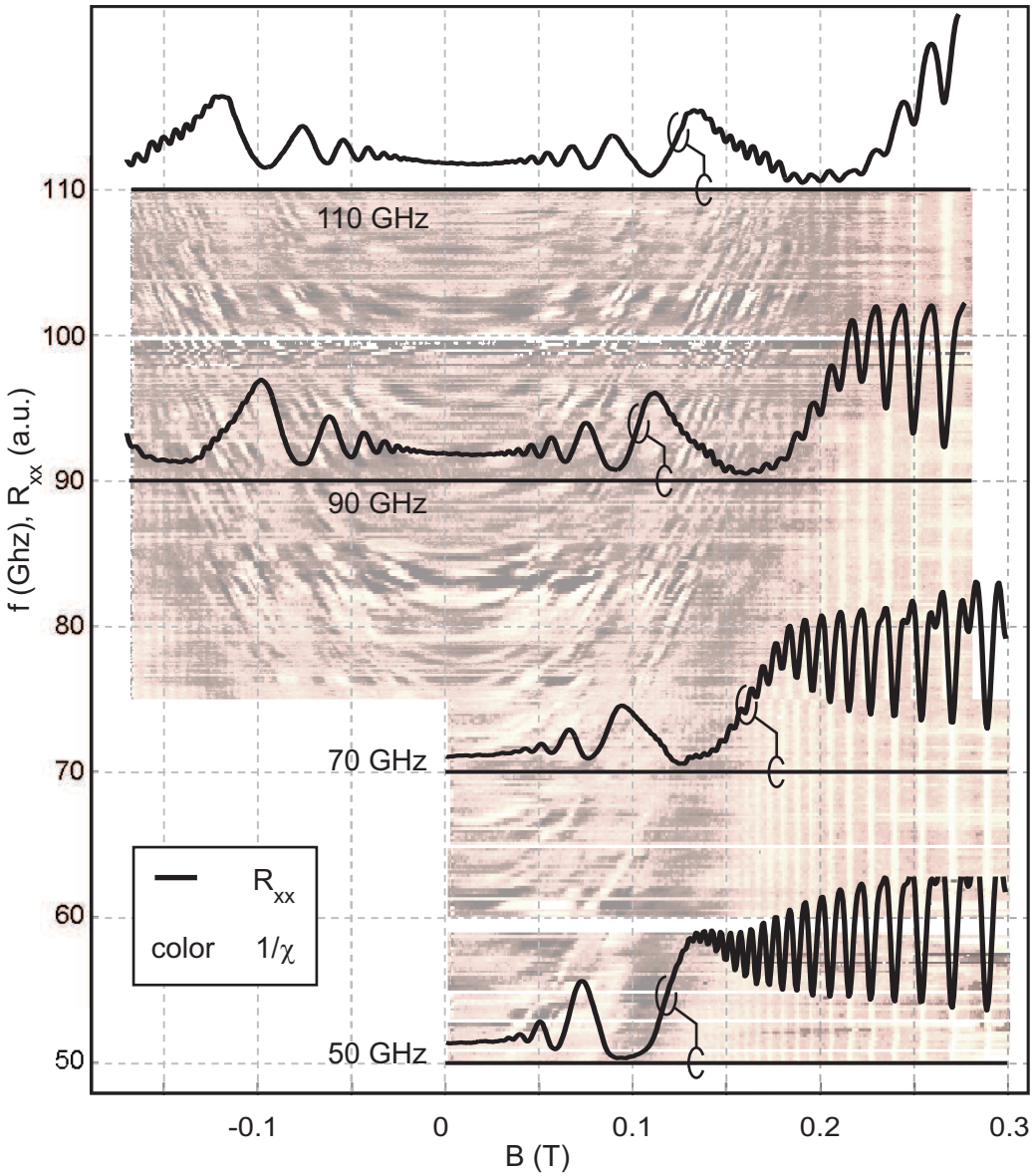

FIGURE 7.21: Color plot: Same $1/\chi$ data as Fig. 7.16. Black traces: Longitudinal resistance for selected frequencies, indicated in the color plot by horizontal lines. First order minima clearly coincide for both types of oscillations. Higher order minima of MICRO are harder to identify here. See Fig. 7.20 for better identification. In the regime of SdH oscillations resistance minima coincide with maxima in the inverse compressibility as expected (see also Fig. 7.11).

7.4.3 Comparison to theoretical prediction: Unexpected sign of $1/\chi$ oscillations

As described in the last section, the data measured during this work revealed microwave induced oscillations in the compressibility of a 2DES. Comparing with transport data we found that the minima in MIRO and MICRO coincide. While the observed $1/B$ periodicity of the inverse compressibility is as predicted in Ref. [10] (see also section 4.2.2), the sign is reversed. The microwave induced correction to $1/\chi$ was predicted to be positive in the regions where minima in R_{xx} are observed.[11] However our experiments can not be directly compared to Ref. [10]. We here describe aspects that need to be taken into account in a future, more specific theoretical analysis.

Nature of the density modulation: local versus global

The prediction in Ref. [10] treats density changes induced *locally by the measuring SET* and thus at finite wavevector q. Even though in our experiment the SET is a local perturbation, the density change is induced by a homogeneous BG, which corresponds to $q = 0$.

Non-equilibrium condition

To relate changes in the electrostatic potential φ measured by our SET to changes in the chemical potential μ^{ch} we assumed that the electrochemical potential $\mu^{\mathrm{elch}} = \varphi + \mu^{\mathrm{ch}}$ is constant because it is fixed by electrical contacts to the 2DES (see section 7.1.3). It might be possible that under the non-equilibrium conditions due to constant microwave irradiation the relation between the measured φ and the desired μ^{ch} is altered. Our measurement signal may thus not be directly proportional to the inverse compressibility.

Role of inhomogeneities

The microwave induced non-equilibrium conditions may lead to another complication in conjunction with disorder in the sample. Under equilibrium conditions the Einstein relation between the conductivity and the diffusion ensures that electric currents arise only from gradients in the electrochemical potential μ^{elch} (see Ref. [102] and section 4.2.2). As this is fixed by contacts, no spontaneous currents can flow even in a disordered sample.

[11] Our measurements do show the expected behavior in the SdH regime (see section 7.2.4). We can therefore exclude the possibility that our measurement method yields a sign error.

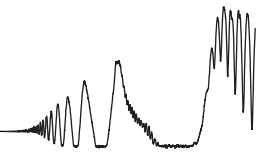

Under non-equilibrium conditions the Einstein relation does not hold and extra terms in the current arise (see Ref. [102]). These photocurrents are especially important near contacts, which represent large inhomogeneities [102]. But also within the sample disorder may lead, under non-equilibrium conditions, to photocurrents. The corresponding photovoltages could be detected by the SET. Our measurement signal thus may have contributions that arise not from a change in the compressibility but from photovoltages.

Further theoretical investigation is needed to clarify these issues.

7.4.4 Discussion of future experiments

Microwave induced compressibility oscillations could be observed in our measurements. To conclude, we discuss possible future experiments to increase data quality and to overcome some of the limitations we encountered with the current measurement setup.

Sample with in-situ backgate, sample quality

We suspect that the quality of our data is to a large part limited by the fact that we use the chip carrier as a BG (due to sample limitations, see section 5.4.2). Indications for this conclusion were discussed in sections 7.2.1 and 7.3.2. It is therefore desirable to repeat the experiments on a sample with an in-situ grown BG to improve the data quality. Furthermore, an in-situ grown BG would allow to induce electron density changes larger by roughly two orders of magnitude. It would allow to investigate the density dependence of MIRO and MICRO together. This deserves special interest as the inverse compressibility of a 2DES becomes negative for small densities (see section 7.3.2). Would microwave induced effects and magnetoplasmon signatures also vanish at this point?

We note that the pronouncedness of MIRO is only mediocre for the wafer we used for compressibility measurements. We observe at most 8 oscillations in R_{xx} of which none drop all the way down to zero. Compare this for example to Fig. 4.1 where 15 oscillations are observed including four zero resistance states. It is desirable to repeat the experiments on a sample that exhibits fully developed regions of vanishing resistance.

We currently have no heterostructure available for this kind of experiments. Unfortunately, as discussed in section 5.3.2, we have only scarce indications on how such a sample can be fabricated.

Scanning experiments

We observed a strong position dependence of several measured quantities: $1/\chi$ in the absence of microwaves, $1/\chi$ in the presence of microwaves, and also the microwave irradiation power near the sample. A setup with the ability to perform scanning SET measurements would allow to identify the spatial dependence of $1/\chi(B, p = 0)$ and MICRO. This might allow to separately assess the inhomogeneity of the radiation field and the properties of the sample in this field.

Experiments in a better defined microwave field

Another opportunity for improvement is in a better defined field distribution in the vicinity of the sample. This could be achieved with a coaxial cable as microwave waveguide. In such a setup fewer partial reflections and interference pattens would occur in the waveguide. A stripped end of the cable acting as a dipole antenna near the sample may result in a locally cleaner radiation field.

Influence of magnetoplasmons, sample size

Strong magnetoplasmon signatures are seen in our compressibility measurements. It is desirable to suppress those effects as they interfere with the $1/B$ periodic and $f-$proportional MICRO we are interested in. A simple way to suppress plasmons is to reduce the dimensions of the Hall bars: For a sample size of 58 μm the lowest frequency plasma oscillation is expected at ≈ 100 GHz at the electron density of $2.1 \times 10^{11}/\mathrm{cm}^2$ present in our heterostructure (see equation 7.13).

We did perform an experiment on two Hall bars of such small dimensions (40×50 $\mu\mathrm{m}^2$ and 60×100 $\mu\mathrm{m}^2$). MIRO were clearly observed and pronouncedness was comparable to larger Hall bars. This is in contrast to a claim that plasmons play an important part in the physics of MIRO [89, 142]. Unfortunately we could not observe MICRO on these samples. The data was of less quality than shown in the top panel of Fig. 7.18. We attribute this to the large variations in MICRO pronouncedness discussed in section 7.3.3 and also to SET limitations. More experiments on small samples to suppress magnetoplasmons are thus desirable.

Kapitel 8

Deutsche Zusammenfassung

Elektronen in eine zweidimensionale Schicht einzusperren hat sich als sehr fruchtbare Idee erwiesen. Zwei Nobelpreise wurden für Arbeiten auf diesem Gebiet vergeben: Ein Preis ging 1985 an Klaus von Klitzing „für die Entdeckung des quantisierten Hall-Effektes"(engl. integer quantum Hall effect, IQHE). Zum ersten Mal wurde dieser 1980 beobachtet [1], als von Klitzing bei tiefen Temperaturen und in einem Magnetfeld das Verhalten von Elektronen untersuchte, die auf eine Schicht beschränkt waren, ein sogenanntes zweidimensionales Elektronensystem (2DES). Überraschenderweise zeigte der Hall-Widerstand, welcher im klassischen Fall proportional zum Magnetfeld ansteigt, hier Plateaus. Die Widerstandswerte dieser Plateaus waren unhabhängig von den genauen experimentellen Bedingungen und lassen sich durch Naturkonstanten ausdrücken:

$$R_{xy} = \frac{h}{i\ e^2} \tag{8.1}$$

wobei $i = 1, 2, 3, \ldots$ eine ganze Zahl ist, h das Plancksche Wirkungsquantum und e die Elementarladung. Dort, wo im Hall-Widerstand Plateaus auftreten, wird verschwindender Längswiderstand R_{xx} gemessen. Die entscheidende Größe des IQHE ist der Füllfaktor ν. Dieser ist das Verhältnis aus Elektronendichte und Dichte magnetischer Flussquanten in der Probe.

Der zweite Nobelpreis wurde 1998 an Robert B. Laughlin, Horst L. Stormer und Daniel C. Tsui vergeben „für die Entdeckung einer neuen Quantenflüssigkeit mit gebrochenzahlig geladenen Anregungen". Sie hatten 1982 die Quanten-Hall-Merkmale, nämlich verschwindendes R_{xx} und Plateaus in R_{xy}, bei einem gebrochenzahligen Füllfaktor $\nu = 1/3$ beobachtet [2]. Eine theoretische Erklärung dieses gebrochenzahligen Quanten-Hall-Effektes (engl. fractional quantum Hall effect, FQHE) wurde 1983 vorgeschlagen [3].

Der einzige experimentelle Unterschied zwischen der Entdeckung des IQHE

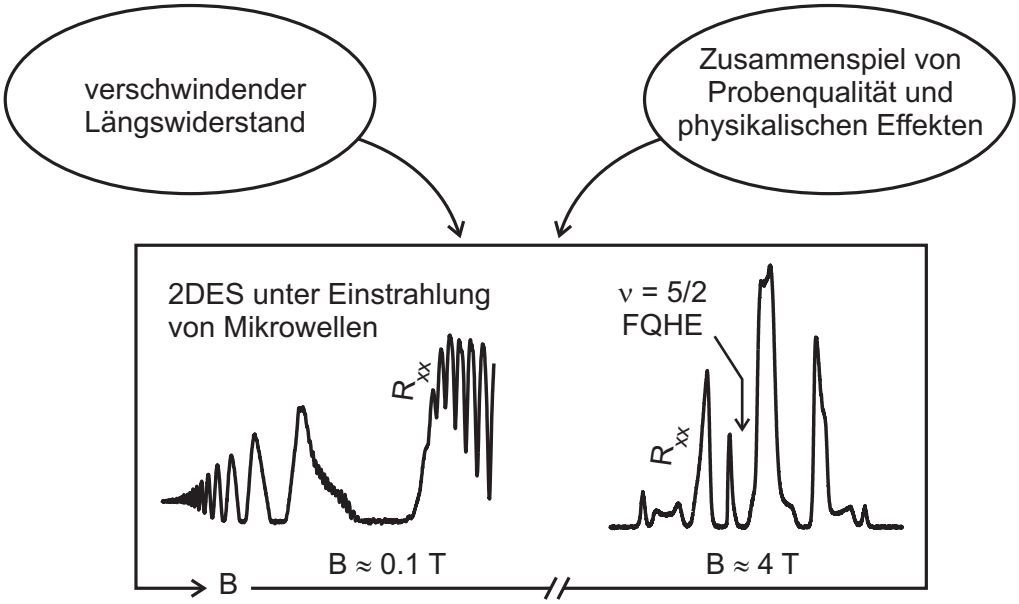

und des FQHE war die bei letzterem höhere Reinheit des Kristalls in den das 2DES eingebettet war, sowie eine niedrigere Messtemperatur. Eine Verbesserung der experimentellen Bedingungen und der Materialqualität hatte also *neue physikalische Effekte* hervorgebracht − ein Trend, der heute noch anhält.

In der vorliegenden Arbeit untersuchen wir zwei Effekte, die nur in den reinsten heute verfügbaren 2DES beobachtet werden. Charakteristisch für beide ist ein verschwindender Längswiderstand, jedoch in sehr unterschiedlichen Magnetfeldbereichen und aus unterschiedlichen Gründen. Es handelt sich um den FQHE bei Füllfaktor 5/2 sowie um das Verhalten des Längswiderstandes unter Mikrowelleneinstrahlung.

Der **FQHE bei Füllfaktor 5/2** war bei seiner Entdeckung 1987 eine Überraschung [4,5], da alle bis dahin beobachteten gebrochenzahligen Quanten-Hall-Zustände Füllfaktoren mit *ungeradzahligem* Nenner hatten. Diese können erklärt werden als der gewöhnliche QHE von neuen Teilchen, den composite fermions (zusammengesetzte Fermionen) [6]. Der 5/2-Zustand passte nicht in dieses Muster. In der Folge wurden verschiedene Erklärungen vorgeschlagen, insbesondere ein Mechanismus, bei dem sich zwei composite fermions ähnlich wie bei Cooper-Paarbildung zusammentun, was zur Bildung einer Energielücke führt. Dieser Mechanismus implizierte eine weitere neuartige Vorhersage: Die elementaren Anregungen des 5/2-Zustandes könnten nichtabelscher Statistik gehorchen. Hierbei kann der Zustand des Systems verändert werden, indem z. B. ein Teilchen um ein anderes herumgeführt wird. Diese nichtabelsche Statistik könnte einen sogenannten topologischen Quantencomputer möglich ma-

chen. Experimentell ist die Vorhersage allerdings noch nicht bestätigt.

Der 5/2-Zustand wird nur in den saubersten heute verfügbaren Proben beobachtet. In der vorliegenden Arbeit benutzen wir eine solche Probe, bei der die Elektronendichte während der Messung über einen weiten Bereich verändert werden kann. Wir untersuchen die Dichteabhängigkeit der Energielücke des 5/2-Zustandes und vergleichen diese mit theoretischen Vorhersagen. Um das Zusammenspiel von Probenqualität und physikalischen Effekten zu beleuchten, diskutieren wir den Einfluss verschiedener Arten von Unordnung auf den 5/2-Zustand. Auch die überraschend große Ausdehnung der Quasiteilchen spielt hier eine Rolle.

Der größte Teil dieser Dissertation befasst sich mit den **Eigenschaften von zweidimensionalen Elektronensystemen unter Mikrowellenstrahlung** bei tiefen Temperaturen und in schwachen Magnetfeldern. Die Magnetfeldabhängigkeit des Längswiderstandes zeigt hier $1/B$-periodische mikrowelleninduzierte Oszillationen (microwave induced resistance oscillations, MIRO) [7]. Bei Verwendung eines extrem reinen 2DES können diese Widerstandsoszillationen in endlichen Magnetfeldbereichen auf Null abfallen [8, 9]. In dieser Hinsicht gleichen sich MIRO und QHE, die zugrundeliegende Physik ist jedoch unterschiedlich: Der Hall-Widerstand wird von der Mikrowellenstrahlung nicht beeinflusst und zeigt keine Plateaus. Desweiteren treten MIRO, im Gegensatz zum QHE, bei Magnetfeldwerten auf, die unabhängig von der Elektronendichte sind. Die charakteristische Größe ist vielmehr das Verhältnis von Mikrowellenfrequenz ω und Zyklotronfrequenz $\omega_c = eB/m^*$, wobei e die Elementarladung ist und m^* die effektive Masse des Kristalls. Widerstandsminima treten auf, wenn

$$\omega = (i + \phi_i)\omega_c, \tag{8.2}$$

mit ganzzahligem $i = 1, 2, 3, \ldots$ und einer Phasenverschiebung ϕ_i. Der zugrundeliegende Mechanismus ist noch nicht abschließend geklärt.

In dieser Arbeit untersuchen wir speziell die Kompressibilität eines 2DES unter Mikrowelleneinstrahlung. Als eine thermodynamische Größe ergänzt diese elektrische Transportmessungen. Die inverse Kompressibilität $1/\chi$ ist die Änderung im chemischen Potential μ^{ch}, hervorgerufen von einer Änderung der Elektronendichte n:

$$1/\chi = \frac{\partial \mu^{\mathrm{ch}}}{\partial n}. \tag{8.3}$$

Wir messen $1/\chi$ lokal mit einem Einzelelektronen-Transistor (single electron transistor, SET), welcher sehr empfindlich für elektrische Potentiale ist. Dabei induzieren wir Änderungen in der Elektronendichte, die gemäß Gleichung 8.3 zu einer Änderung des chemischen Potentials führen und mit einem SET de-

tektiert werden. Um diese bekannte Technik für unsere Zwecke zu verwenden, muss die Heterostruktur, in die das 2DES eingebettet ist, verschiedene Anforderungen erfüllen: Sie sollte ausgeprägte MIRO zeigen, die Elektronendichte muss verändert werden können, und schließlich müssen die SETs verwendbar sein. Es stellte sich heraus, dass diese Kombination nicht einfach zu erfüllen war.

Wir konnten erfolgreich zeigen, dass Kompressibilitätsmessungen unter Mikrowelleneinstrahlung möglich sind. Die Kompressibilität zeigt Oszillationen, die denen des Längswiderstandes ähnlich sind. Die Ergebnisse können bei der Identifikation des zugrundeliegenden Mechanismus hilfreich sein.

Die vorliegende Arbeit ist in zwei Teile gegliedert. **Teil I** beschreibt die theoretischen Grundlagen, **Teil II** die durchgeführten Experimente und deren Diskussion. Jeder Teil ist in drei Kapitel unterteilt. Das jeweils erste beschreibt die Eigenschaften von 2DES, das zweite den FQHE bei Füllfaktor 5/2, und das jeweils dritte Kapitel ist den Eigenschaften eines 2DES unter Mikrowelleneinstrahlung gewidmet. Im Folgenden geben wir eine kapitelweise Zusammenfassung dieser Arbeit.

Kapitel 2 beschreibt klassische Eigenschaften von elektrischem Transport in Magnetfeldern sowie Grundlagen des 2DES. Verschiedene Designparameter und Materialeigenschaften von GaAs-Heterostrukturen werden, da für diese Arbeit wichtig, eingehender beschrieben.

Kapitel 3 stellt die Grundlagen des ganzzahligen und des gebrochenzahligen Quanten-Hall-Effektes dar, mit besonderem Augenmerk auf den 5/2-Zustand.

Kapitel 4 gibt eine Übersicht über den experimentellen und theoretischen Stand der Untersuchungen an 2DES unter Mikrowelleneinstrahlung.

Kapitel 5 ist das erste Kapitel des experimentellen Teils. Die Qualität der verwendeten Heterostrukturen ist für diese Arbeit kritisch, und ein nichttrivialer Teil war die Suche nach geeignetem Material. Wir haben daher den Zusammenhang verschiedener Designparameter und Kennzahlen mit der Ausgeprägtheit des 5/2-Zustandes und MIRO untersucht, insbesondere den Einfluss der Elektronendichte, der Elektronenbeweglichkeit, der Quanten-Lebensdauer (engl. quantum lifetime τ_q), der Spacer-Dicke (Abstand zwischen Dotierschicht und 2DES) sowie der Überdotierung.

Insgesamt ergab sich ein überraschend geringer Zusammenhang dieser Kennzahlen mit den untersuchten Effekten. Insbesondere die Beweglichkeit, welche in der Literatur standardmäßig als Qualitätskennzahl angegeben wird, ist wenig aussagekräftig: Ein hoher Wert ist zwar eine Voraussetzung für das Auftreten der uns interessierenden Effekte, korelliert jedoch

darüberhinaus kaum mit deren Ausgeprägtheit. Dies folgt aus unseren eigenen Untersuchungen von etwa 20 Wafern sowie aus der Literatur bei Gegenüberstellung der Energielücke des 5/2-Zustandes und der Beweglichkeit der Proben. Leider belegen unsere Ergebnisse hier hauptsächlich, dass klare Zusammenhänge fehlen und die begrenzenden Parameter nicht bekannt sind. Nichtsdestoweniger konnten wir für unsere Experimente geeignete Wafer identifizieren.

Kapitel 6 stellt die unseres Wissens nach einzige dichteabhängige Studie eines vollständig quantisierten 5/2-Zustandes dar, die auf *einer* Probe und also für ein *festes Unordnungspotential* durchgeführt wurde. Dies ist wichtig, da, wie in Kapitel 5 beschrieben, die Faktoren nicht bekannt sind, welche die Ausgeprägtheit des 5/2-Zustandes begrenzen. Wie zu erwarten steigt die 5/2-Energielücke mit zunehmender Dichte stark an.

Zum Vergleich mit der Theorie wurden von Prof. Dr. R. Morf (Paul Scherrer Institut, Schweiz) numerische Berechnungen durchgeführt, die explizit Mischungseffekte von Landauniveaus und die Breite der Wellenfunktion für unsere spezeille Probe berücksichtigen. Obwohl dies die Diskrepanz zwischen Theorie und Experiment um etwa einen Faktor zwei reduziert, sind die experimentellen Werte auch bei den größten Dichten noch etwa fünfmal kleiner als die vorhergesagten.

Eine mögliche Erklärung für diese Diskrepanz ist die überraschend große Ausdehnung der Quasiteilchen des 5/2-Zustandes: Diese haben bei einem typischen Magnetfeld von 4 T einen Durchmesser von über 150 nm. Das ist deutlich mehr als der Abstand der Dotieratome zum 2DES (66 nm) und damit mehr als die Korrelationslänge der von den ionisierten Donatoren hervorgerufenen Unordnungslandschaft, in der sich die Teilchen bewegen. Dies erleichtert Quanten-Tunnelvorgänge durch Sattelpunkte des Unordnungspotentials, was zu dissipativem Widerstand führt und die Energielücke entsprechend reduziert.

Kapitel 7 beschreibt unsere Ergebnisse zur Kompressibilität eines 2DES unter Mikrowelleneinstrahlung. Zunächst werden der Messaufbau und das Funktionsprinzip eines SET sowie dessen Charakterisierung beschrieben.

Anschließend behandeln wir zwei Komplikationen: Zum einen muss, um den Einfluss von Mirkowellen zu untersuchen, notwendigerweise auch der messende SET dieser Strahlung ausgesetzt werden, was dessen Eigenschaften stark beeinflusst. Einerseits macht dies eine äußerst sorgfältige Kalibrierung notwendig, erlaubt aber andererseits lokale Eigenschaften des

Strahlungsfeldes zu detektieren. Dieses stellte sich als überraschend inhomogen und frequenzabhängig heraus, was für eine saubere Interpretation der Kompressibilitätsmessungen berücksichtigt werden muss. Desweiteren mussten wir feststellen, dass auch die Kompressibilität ohne Mikrowelleneinfluss ein teilweise unerwartetes Verhalten zeigt: Die gemessenen Werte streuen stark für verschiedene Proben und Positionen auf derselben Probe und sind generell kleiner als erwartet. Der Grund ist vermutlich, dass wir keine Proben mit *integriertem* Gate zur Elektronendichteänderung (backgate) zur Verfügung haben. Wir mussten daher die Rückseite der Probe als solches Gate verwenden, was keine wohldefinierte Geometrie darstellt. Diese Einschränkung verhindert zwar vorerst eine quantitative Interpretation unserer Ergebnisse, der relative Einfluss der Mikrowenenbestrahlung kann aber bestimmt werden.

Mikrowelleneinstrahlung ruft in der Kompressibilität zwei Veränderungen hervor: Magnetoplasmonen werden angeregt, und $1/B-$periodische Oszillationen treten auf, die wir als MICRO bezeichnen (engl. microwave induced compressibility oscillations). Letztere sind stark von den Magnetoplasmonstrukturen überlagert und treten am deutlichsten bei niedrigen Mikrowellenleistungen und nach einem frequenzabhängigen Mittelungsverfahren hervor. Wir beobachten, dass die Kompressibilitätsoszillationen (MICRO) mit den Oszillationen in R_{xx} (MIRO) zusammenfallen. Das Vorzeichen der MICRO ist *entgegengesetzt*[1] zu dem der MIRO und damit engegengesetzt zu einer ersten theoretischen Vorhersage [10]. Es muss jedoch in Zukunft geprüft werden, inwieweit dort gemachten Voraussetzungen den Gegebenheiten unseres Aufbaus entsprechen.

Abschließend diskutieren wir mögliche zukünftige Experimente. Als besonders dringlich erachten wir das Auffinden von Proben mit integriertem backgate zur Elektronendichteveränderung. Dies würde insbesondere quantitative Aussagen ermöglichen sowie Messungen in unterschiedlichen Dichtebereichen, in denen ein qualitativ anderes Verhalten der Kompressibilität erwartet wird.

Teile der in dieser Dissertation dargestellten Ergebnisse wurden bereits veröffentlicht:

- J. Nuebler, V. Umansky, R. Morf, M. Heiblum, K. von Klitzing and J. Smet: *Density dependence of the $\nu = 5/2$ energy gap: Experiment and theory*, PRB **81**, 035316 (2010).

[1] Die Vorzeichen der Oszillationen in R_{xx} und χ sind entgegengesetzt. Unsere Graphen zeigen meist die inverse Kompressibilität $1/\chi$, da dies unserer Messmethode entspricht. Dementsprechen sind die Vorzeichen der Oszillationen in R_{xx} und $1/\chi$ gleich.

Appendix A

Electron density dependence of $1/\chi$

A.1 Globally changing the density with a BG

Figure A.1 shows three plots for different electron densities changed by a voltage applied to the backgate. As the sample has no in-situ grown BG we use, as always, the chip carrier as a BG to change the density. The attainable density range is unfortunately very limited: We applied +30 V and −30 V, respectively, which results in a change of roughly $\pm 6 \times 10^9/\mathrm{cm}^2$ or ±3%.

Magnetoplasmon signatures change slightly. A change is expected according to equation 7.13, but due to the erratic distribution we can not unambiguously identify certain structures and measure their frequency shifts.

The fan-like MICRO structures change little or not at all for decreased electron density (top panel) but are moderately less pronounced for increased density (bottom panel). We suspect that the reduced MICRO pronouncedness is due to density inhomogeneities. As described in section 7.3.2 we have evidence that such inhomogeneities arise because we use the chip carrier as a BG (see also inset in Fig. 7.8).

A.2 Locally changing the density with an SET

When a voltage is applied between the 2DES and the SET the electron density is locally modified.

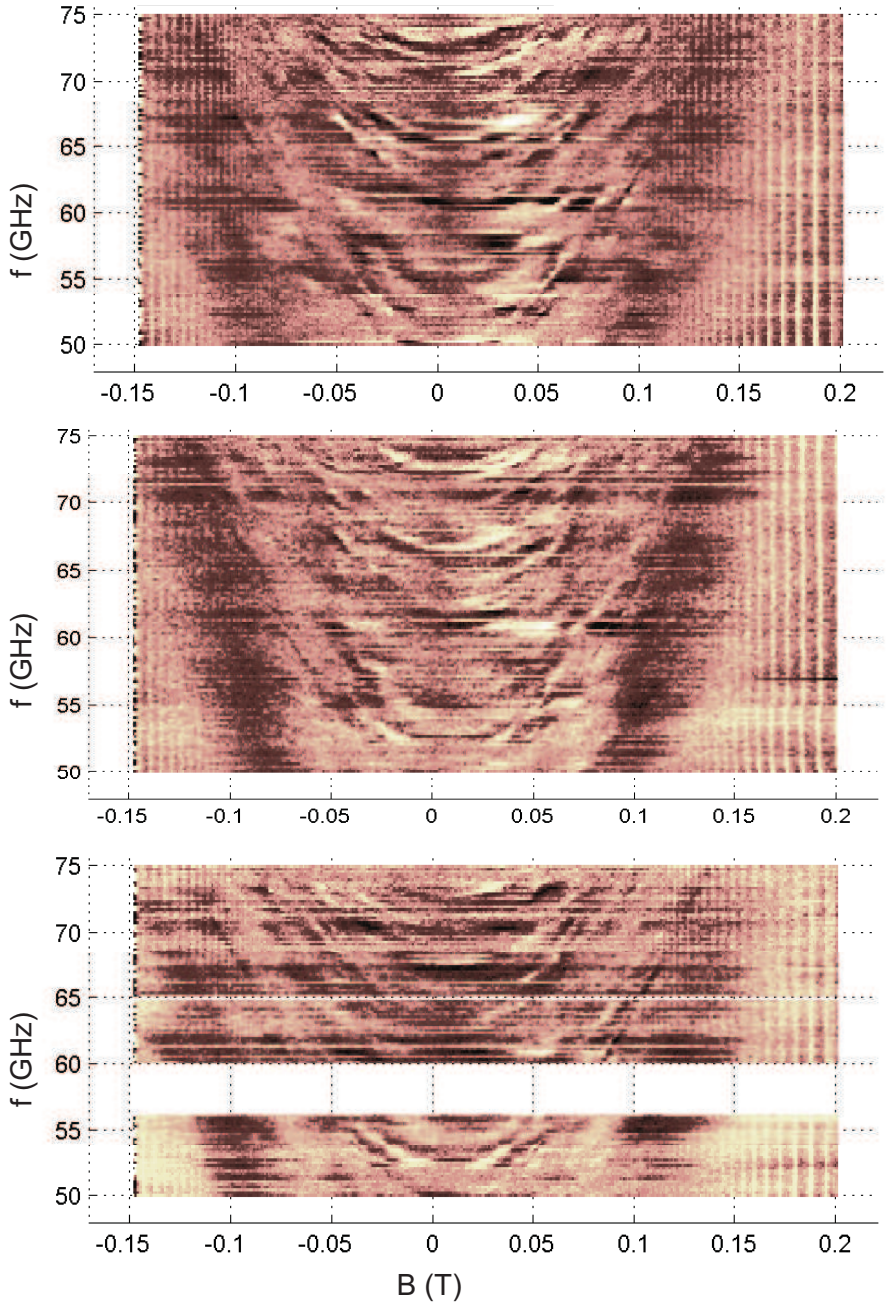

FIGURE A.1: Electron density dependence of inverse compressibility. The middle picture is the same as in Fig. 7.17, for the upper and the lower the electron density has been decreased and increased by $6 \times 10^9/\mathrm{cm}^2$.

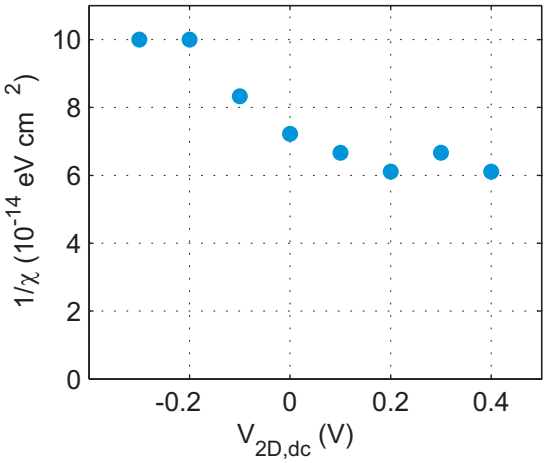

FIGURE A.2: Inverse compressibility in the absence of microwaves at $B = 0$ as a function of voltage applied between 2DES and SET. The electron density locally decreases when a positive voltage is applied.

Density dependence in the absence of microwaves

Here the inverse compressibility at zero magnetic field in the absence of microwaves was investigated. Fig. A.2 shows that $1/\chi(B, p = 0)$ decreases for smaller electron densities (that are found for positive voltage between 2DES and SET). This is in line with equation 7.9.

Density dependence under microwave irradiation

We also made an attempt to investigate the inverse compressibility under microwave irradiation with locally modified electron density. We did, however, not observe any significant changes: The magnetoplasmon signatures as dominant structures seem unaffected. MICRO were only poorly pronounced and no clear influence was identified. More experiments are necessary here.

Appendix B

Fabrication of single electron transistors

All single electron transistors (SET) used in this work were fabricated in the group of Prof. Amir Yacoby at Harvard University, USA. The fabrication recipe had been developed by Basile Verdene and adapted to new infrastructure by Jonah Waissman and Vivek Venkatachalam with partial help from us. A general overview over the fabrication and the working principle of SETs is given in section 7.1. Here we give a detailed fabrication protocol.

Sample preparation in Stuttgart (Optical lithography)

A rectangular piece of heterostructure of about 5×7 mm^2 is used. An example (fully processed) is given in Fig. B.1. More detailed pictures are in the main text, see Fig. 7.2.

1. Clean for 10 min in acetone with ultrasonication (use plastic beaker to reduce risk of shattering).
2. Mesa etch:
   (a) Spincoat with positive photoresist S 1805 (Rohm and Haas) for 30 s at 6000 rpm.
   (b) Bake on hotplate for 2 min at 90 °C.
   (c) Expose with mask aligner MA6 (Suess) for 15 s.
   (d) Develop in AZ 726 MIF (AZ electronics materials) for 30 s.
   (e) Wet etch in solution H_2SO_4:H_2O_2:H_2O (1:8:1000). Etching should stop between doping layer and 2DES ($95 - 100$ nm for wafer 8-307).

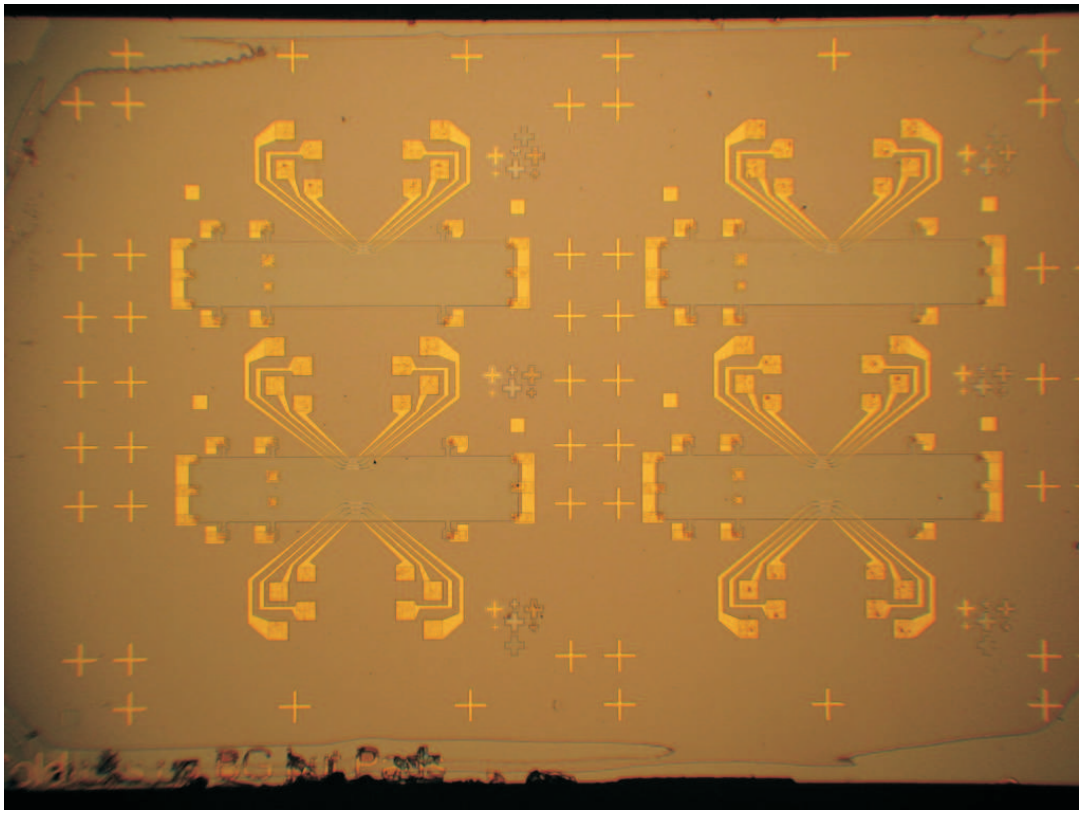

FIGURE B.1: Photograph of a fully processed sample with four Hall bars, two of them with four SETs, two with eight SETs (only the connections to the SETs are visible at this scale). Sample dimensions are $\approx 5 \times 7$ mm^2, the Hallbars are 0.4 mm wide.

3. Alloyed contacts:

   (a) Spincoat with negative photoresist AZ 5214 E for 30 s at 6000 rpm.

   (b) Bake on hotplate for 4 min at 90 °C.

   (c) Expose with mask aligner MA6 for 13 s.

   (d) Post exposure bake on hotplate for 1 min at 125 °C.

   (e) Flood expose (no mask) with mask aligner MA6 for 70 s.

   (f) Develop in AZ 726 MIF for 30 s.

   (g) Special cleaning before contact metalization:

      i. 30s O_2 plasma cleaning (0.3 torr, 200 W, using lower position in 100-EPLASMA SYSTEM from Technics Plasma GmbH)

      ii. 2 min immersion in 'Semico Clean'

iii. 5 s dip in DI water
iv. 5 s dip in HCl (30%)
v. 5 s dip in DI water
vi. immediately prepare for contact metal evaporation

(h) Metalization using Leybold Heraeus Univex:
i. 7.5 nm Ni
ii. 80 nm Ge
iii. 160 nm Au
iv. 36 nm Ni

(i) Liftoff in acetone, 55 °C.

(j) Anneal contacts using AZ500 from MBE Komponenten GmbH:
i. 120 s at 370 °C, forming gas 0.3 bar, no gas flow
ii. 50 s at 440 °C, forming gas 0.3 bar, no gas flow
iii. rapid cooldown, with forming gas flow

4. Shallow connections for SETs:
To allow the future SETs to climb onto these gates the thickness must be considerably less than what is used for the SETs. As the Al for the SETs has bad contact properties with Au, we use AuPd here.

(a) Spincoat with negative photoresist AZ 5214 E for 30 s at 6000 rpm.

(b) Bake on hotplate for 4 min at 90 °C.

(c) Expose with mask aligner MA6 for 13 s.

(d) Post exposure bake on hotplate for 1 min at 125 °C.

(e) Flood expose (no mask) with mask aligner MA6 for 70 s.

(f) Develop using developer AZ 726 MIF for 30 s.

(g) Metalization using Leybold Heraeus Univex:
i. 7 nm AuPd (40 % Pd)

(h) Liftoff in acetone, 55 °C.

5. Au pads for bonding and SET connection protection:
These are much thicker than the SET connections and overlap with them in most parts, except at the ends near the SETs (see Fig. 7.2 for detailed SEM pictures). They also overlap with the alloyed contacts to facilitate wire bonding.

(a) Spincoat with negative photoresist AZ 5214 E for 30 s at 6000 rpm.

(b) Bake on hotplate for 4 min at 90 °C.

(c) Expose with mask aligner MA6 for 13 s.

(d) Post exposure bake on hotplate for 1 min at 125 °C.

(e) Flood expose (no mask) with mask aligner MA6 for 70 s.

(f) Develop using developer AZ 726 MIF for 30 s.

(g) Metalization using Leybold Heraeus Univex:

i. 15 nm Cr

ii. 150 nm Au

(h) Liftoff in acetone, 55 °C.

6. Send to Harvard for SET fabrication.

SET fabrication at Harvard (Electron beam lithography)

Due to the small dimensions of the SETs (width of smallest structures ≈ 80 nm) electron beam lithography has to be used.

The Al-based SETs consist of an island with an oxidized surface and two leads, each of which overlaps the island surface in a small region (see main text, section 7.1.1). One single EBL writing is sufficient for *both* metalizations thanks to a directionally selective evaporation technique. The small features making up the main part of the SET are defined as narrow, deep trenches in the resist (width ≈ 100 nm, depth ≈ 350 nm). For metalization, the sample is mounted in the evaporation chamber at a polar angle of 35° with an in-situ variable azimuth angle. Varying the latter, one can selectively metalize trenches in one direction while the other direction is shaded due to the high aspect ratio of the trenches (see Fig. B.2).

1. Electron beam lithography:

(a) Spincoat resist MMA(8.5 %)MAA EL 6 % for 40 s at 5000 rpm (thickness ≈ 140 nm).

(b) Bake on hotplate for 10 min at 180 °C.

(c) Spincoat resist PMMA A4 for 40 s at 4000 rpm (thickness ≈ 200 nm).

(d) Bake on hotplate for 10 min at 180 °C.

(e) Expose sample in EBL system Elionix ELS-7000: 75 μm chip size, 60000 dots per inch. Dose factors are given in Fig. B.2.

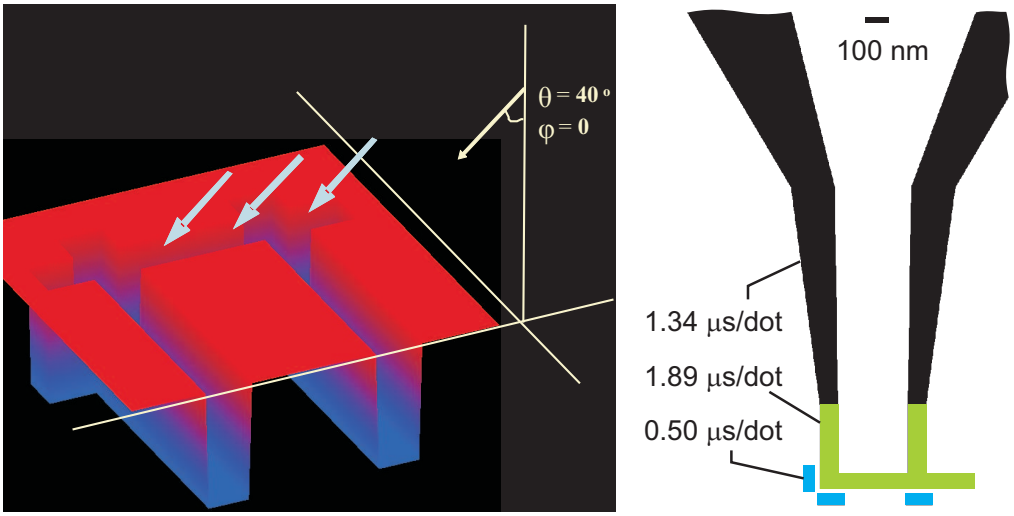

FIGURE B.2: Left: Selective metalization of SET island and leads by evaporation from different azimuth angles. (Picture adapted from Basile Verdene's fabrication protocol.) Right: Doses for EBL exposure of the SET region. The blue pads facilitate undercut formation.

(f) Develop in MIBK:IPA (1:3). Developing is done at 0°C (ice), supposably yielding more controlled conditions.

2. First evaporation (island): 15 nm Al

3. Oxidation: 2.8 torr of dry air for 6 min. Pump gas away before next step.

4. Second evaporation (leads): 30 nm Al

5. Send back to Stuttgart, usually without previous liftoff.

Last fabrication steps in Stuttgart

1. Liftoff: 2 hrs, acetone 55 °C, NO SONICATION !

2. Cleave sample in half.

3. Glue into chipcarrier: Apply a drop of PMMA with a brush. Put sample on drop. Use a tiny amount of PMMA to prevent flow onto the top side of the sample when it is placed in the drop.

4. Wire bonding. Proper grounding reduces the risk of destroying SETs. First, all 24 pins are shorted by wire bonding. Then, the sample is bonded. We also apply a bond wire to the chip carrier surface (next to the sample)

in order to use it as a backgate to change the electron density. The shorting ring is removed with a tweezer under an optical microscope only *after* the sample is mounted into the sampleholder and all pins are shorted by the breakout box at the other end of the sample holder. We also had success without this precaution, but usually adopted it nevertheless.

Bibliography

[1] K. v. Klitzing, G. Dorda, and M. Pepper, "New method for high-accuracy determination of the fine-structure constant based on quantized Hall resistance," *Phys. Rev. Lett.*, vol. 45, pp. 494–497, Aug 1980.

[2] D. C. Tsui, H. L. Stormer, and A. C. Gossard, "Two-dimensional magnetotransport in the extreme quantum limit," *Phys. Rev. Lett.*, vol. 48, pp. 1559–1562, May 1982.

[3] R. B. Laughlin, "Anomalous quantum Hall effect: An incompressible quantum fluid with fractionally charged excitations," *Phys. Rev. Lett.*, vol. 50, pp. 1395–1398, May 1983.

[4] R. Willett, J. P. Eisenstein, H. L. Störmer, D. C. Tsui, A. C. Gossard, and J. H. English, "Observation of an even-denominator quantum number in the fractional quantum Hall effect," *Phys. Rev. Lett.*, vol. 59, pp. 1776–1779, Oct 1987.

[5] W. Pan, J.-S. Xia, V. Shvarts, D. E. Adams, H. L. Stormer, D. C. Tsui, L. N. Pfeiffer, K. W. Baldwin, and K. W. West, "Exact quantization of the even-denominator fractional quantum Hall state at $\nu = 5/2$ Landau level filling factor," *Phys. Rev. Lett.*, vol. 83, pp. 3530–3533, Oct 1999.

[6] J. K. Jain, "Composite-fermion approach for the fractional quantum Hall effect," *Phys. Rev. Lett.*, vol. 63, pp. 199–202, Jul 1989.

[7] M. A. Zudov, R. R. Du, J. A. Simmons, and J. L. Reno, "Shubnikov–de Haas-like oscillations in millimeterwave photoconductivity in a high-mobility two-dimensional electron gas," *Phys. Rev. B*, vol. 64, p. 201311, Oct 2001.

[8] R. G. Mani, J. H. Smet, K. von Klitzing, V. Narayanamurti, W. B. Johnson, and V. Umansky, "Zero-resistance states induced by electromagnetic-wave excitation in GaAs/AlGaAs heterostructures," *Nature*, vol. 420, pp. 646–650, Dec. 2002.

[9] M. A. Zudov, R. R. Du, L. N. Pfeiffer, and K. W. West, "Evidence for a new dissipationless effect in 2D electronic transport," *Phys. Rev. Lett.*, vol. 90, p. 046807, Jan 2003.

[10] M. G. Vavilov, I. A. Dmitriev, I. L. Aleiner, A. D. Mirlin, and D. G. Polyakov, "Compressibility of a two-dimensional electron gas under microwave radiation," *Phys. Rev. B*, vol. 70, p. 161306, Oct 2004.

[11] H. L. Stormer, R. Dingle, A. C. Gossard, and W. Wiegmann *Inst. Conf. Ser. London*, vol. 43, p. 557, 1978.

[12] R. Dingle, H. L. Störmer, A. C. Gossard, and W. Wiegmann, "Electron mobilities in modulation-doped semiconductor heterojunction superlattices," *Appl. Phys. Lett.*, vol. 33, no. 7, pp. 665–667, 1978.

[13] V. Umansky, M. Heiblum, Y. Levinson, J. Smet, J. N"ubler, and M. Dolev, "MBE growth of ultra-low disorder 2DEG with mobility exceeding $35 \times 10^6 \mathrm{cm}^2/\mathrm{Vs}$," *Journal of Crystal Growth*, vol. 311, no. 7, pp. 1658 – 1661, 2009.

[14] J. H. Davies, *The physics of low-dimensional semiconductors: An introduction*. Cambridge University Press, 1997.

[15] P. M. Mooney, "Deep donor levels (DX centers) in III-V semiconductors," *Journal of Applied Physics*, vol. 67, pp. R1 –R26, feb. 1990.

[16] G. Gamez and Muraki, "$\nu = 5/2$ fractional quantum Hall state in low-mobility electron systems: different roles of disorder," *arXiv:1101.5856v1*, 2011.

[17] T. Baba, T. Mizutani, and M. Ogawa, "Elimination of persistent photoconductivity and improvement in Si activation coefficient by Al spatial separation from Ga and Si in Al–Ga–As:Si Solid System – a novel short period AlAs/n-GaAs superlattice," *Japanese Journal of Applied Physics*, vol. 22, no. Part 2, No. 10, pp. L627–L629, 1983.

[18] K.-J. Friedland, R. Hey, H. Kostial, R. Klann, and K. Ploog, "New concept for the reduction of impurity scattering in remotely doped GaAs quantum wells," *Phys. Rev. Lett.*, vol. 77, pp. 4616–4619, Nov 1996.

[19] V. Umansky, R. de Picciotto, and M. Heiblum, "Extremely high-mobility two dimensional electron gas: Evaluation of scattering mechanisms," *Applied Physics Letters*, vol. 71, no. 5, pp. 683 –685, 1997.

[20] J. Shabani, Y. Liu, and M. Shayegan, "Fractional quantum Hall effect at high fillings in a two-subband electron system," *Phys. Rev. Lett.*, vol. 105, p. 246805, Dec 2010.

[21] S. Das Sarma and F. Stern, "Single-particle relaxation time versus scattering time in an impure electron gas," *Phys. Rev. B*, vol. 32, pp. 8442–8444, Dec 1985.

[22] S. J. MacLeod, K. Chan, T. P. Martin, A. R. Hamilton, A. See, A. P. Micolich, M. Aagesen, and P. E. Lindelof, "Role of background impurities in the single-particle relaxation lifetime of a two-dimensional electron gas," *Phys. Rev. B*, vol. 80, p. 035310, Jul 2009.

[23] E. H. Hwang and S. Das Sarma, "Limit to two-dimensional mobility in modulation-doped GaAs quantum structures: How to achieve a mobility of 100 million," *Phys. Rev. B*, vol. 77, p. 235437, Jun 2008.

[24] A. Gold, "Mobility of the two-dimensional electron gas in AlGaAs/GaAs heterostructures at low electron densities," *Applied Physics Letters*, vol. 54, no. 21, pp. 2100–2102, 1989.

[25] A. Gold, "Transport theory for quantum wells with an electric field across the well: a new concept for a transistor," *Z. Phys. B*, vol. 71, p. 295, 1987.

[26] K. Lee, M. S. Shur, T. J. Drummond, and H. Morkoç, "Low field mobility of 2D electron gas in modulation doped $Al_xGa_{1-x}As$/GaAs layers," *Journal of Applied Physics*, vol. 54, no. 11, pp. 6432–6438, 1983.

[27] M. Shayegan, V. J. Goldman, C. Jiang, T. Sajoto, and M. Santos, "Growth of low-density two-dimensional electron system with very high mobility by molecular beam epitaxy," *Applied Physics Letters*, vol. 52, no. 13, pp. 1086–1088, 1988.

[28] P. T. Coleridge, "Small-angle scattering in two-dimensional electron gases," *Phys. Rev. B*, vol. 44, pp. 3793–3801, Aug 1991.

[29] P. T. Coleridge, R. Stoner, and R. Fletcher, "Low-field transport coefficients in GaAs/$Ga_{1-x}Al_xAs$ heterostructures," *Phys. Rev. B*, vol. 39, pp. 1120–1124, Jan 1989.

[30] T.-M. Chen, C. T. Liang, M. Y. Simmons, G.-H. Kim, and D. A. Ritchie, "Transport and quantum lifetime dependence on electron density in gated GaAs/AlGaAs heterostructures," *Physica E: Low-dimensional Systems and Nanostructures*, vol. 22, pp. 312 – 315, 2004.

[31] T. Heinzel, *Mesoscopic Electronics in Solid State Nanostructures*. Wiley-VCH, 2007.

[32] J. K. Jain, *Composite fermions*. Cambridge University Press, 2007.

[33] R. J. Nicholas, R. J. Haug, K. v. Klitzing, and G. Weimann, "Exchange enhancement of the spin splitting in a GaAs/$Ga_{1-x}Al_x$As heterojunction," *Phys. Rev. B*, vol. 37, pp. 1294–1302, Jan 1988.

[34] J. Weber, *Einzelelektronen-Transistoren auf Spitzen zur Verwendung in der Rastersondenmikroskopie bei tiefen Temperaturen*. PhD thesis, Fakultät für Elektrotechnik und Informationstechnik der Technischen Universität Ilmenau, 2009.

[35] D. B. Chklovskii, B. I. Shklovskii, and L. I. Glazman, "Electrostatics of edge channels," *Phys. Rev. B*, vol. 46, pp. 4026–4034, Aug 1992.

[36] R. G. Klaus von Klitzing and J. Weiss, "25 Jahre Quanten-Hall-Effekt," *Physik Journal*, vol. 4, p. 37, 2005.

[37] A. Siddiki and R. R. Gerhardts, "Incompressible strips in dissipative Hall bars as origin of quantized Hall plateaus," *Phys. Rev. B*, vol. 70, p. 195335, Nov 2004.

[38] E. Ahlswede, *Potential- und Stromverteilung beim Quanten-Hall-Effekt bestimmt mittels Rasterkraftmikroskopie*. PhD thesis, Universität Stuttgart, 2002.

[39] T. Ando, A. B. Fowler, and F. Stern, "Electronic properties of two-dimensional systems," *Rev. Mod. Phys.*, vol. 54, pp. 437–672, Apr 1982.

[40] D. G. Polyakov and B. I. Shklovskii, "Universal prefactor of activated conductivity in the quantum Hall effect," *Phys. Rev. Lett.*, vol. 74, pp. 150–153, Jan 1995.

[41] N. d'Ambrumenil, B. I. Halperin, and R. H. Morf, "Model for dissipative conductance in fractional quantum hall states," *Phys. Rev. Lett.*, vol. 106, p. 126804, Mar 2011.

[42] S. Ilani, J. Martin, E. Teitelbaum, J. H. Smet, D. Mahalu, V. Umansky, and A. Yacoby, "The microscopic nature of localization in the quantum Hall effect," *Nature*, vol. 427, pp. 328–332, Jan. 2004.

[43] F. Dahlem, *Adiabatic transport in the quantum Hall regime: comparison between transport and scanning force microscopy investigations*. PhD thesis, Universität Stuttgart, 2008.

[44] K. Lier and R. R. Gerhardts, "Self-consistent calculations of edge channels in laterally confined two-dimensional electron systems," *Phys. Rev. B*, vol. 50, pp. 7757–7767, Sep 1994.

[45] E. Ahlswede, P. Weitz, J. Weis, K. von Klitzing, and K. Eberl, "Hall potential profiles in the quantum Hall regime measured by a scanning force microscope," *Physica B: Condensed Matter*, vol. 298, pp. 562 – 566, 2001.

[46] E. Ahlswede, J. Weis, K. v. Klitzing, and K. Eberl, "Hall potential distribution in the quantum Hall regime in the vicinity of a potential probe contact," *Physica E: Low-dimensional Systems and Nanostructures*, vol. 12, pp. 165 – 168, 2002.

[47] J. Weis, Y. Y. Wei, and K. v. Klitzing, "Single-electron transistor probes two-dimensional electron system in high magnetic fields," *Physica E: Low-dimensional Systems and Nanostructures*, vol. 3, pp. 23 – 29, 1998.

[48] Y. Y. Wei, J. Weis, K. v. Klitzing, and K. Eberl, "Edge strips in the quantum Hall regime imaged by a single-electron transistor," *Phys. Rev. Lett.*, vol. 81, pp. 1674–1677, Aug 1998.

[49] J. H. Smet, D. Weiss, R. H. Blick, G. Lütjering, K. von Klitzing, R. Fleischmann, R. Ketzmerick, T. Geisel, and G. Weimann, "Magnetic focusing of composite fermions through arrays of cavities," *Phys. Rev. Lett.*, vol. 77, pp. 2272–2275, Sep 1996.

[50] J. H. Smet, D. Weiss, K. von Klitzing, P. T. Coleridge, Z. W. Wasilewski, R. Bergmann, H. Schweizer, and A. Scherer, "Composite fermions in periodic and random antidot lattices," *Phys. Rev. B*, vol. 56, pp. 3598–3601, Aug 1997.

[51] I. Kukushkin, J. Smet, K. von Klitzing, and W. Wegscheider, "Cyclotron resonance of composite fermions," *Nature*, vol. 415, p. 409, 2002.

[52] J. S. Xia, W. Pan, C. L. Vicente, E. D. Adams, N. S. Sullivan, H. L. Stormer, D. C. Tsui, L. N. Pfeiffer, K. W. Baldwin, and K. W. West, "Electron correlation in the second Landau level: a competition between many nearly degenerate quantum phases," *Phys. Rev. Lett.*, vol. 93, p. 176809, Oct 2004.

[53] W. Pan, J. S. Xia, H. L. Stormer, D. C. Tsui, C. Vicente, E. D. Adams, N. S. Sullivan, L. N. Pfeiffer, K. W. Baldwin, and K. W. West, "Experimental studies of the fractional quantum Hall effect in the first excited Landau level," *Phys. Rev. B*, vol. 77, p. 075307, Feb 2008.

[54] A. Kumar, G. A. Csáthy, M. J. Manfra, L. N. Pfeiffer, and K. W. West, "Nonconventional odd-denominator fractional quantum Hall states in the second Landau level," *Phys. Rev. Lett.*, vol. 105, p. 246808, Dec 2010.

[55] M. Greiter, X. G. Wen, and F. Wilczek, "Paired Hall states," *Nuclear Physics B*, vol. 374, p. 657, 1992.

[56] G. Moore and N. Read, "Nonabelions in the fractional quantum Hall effect," *Nuclear Physics B*, vol. 360, pp. 362 – 396, 1991.

[57] M. R. Peterson, T. Jolicoeur, and S. Das Sarma, "Finite-layer thickness stabilizes the Pfaffian state for the 5/2 fractional quantum Hall effect: wave function overlap and topological degeneracy," *Phys. Rev. Lett.*, vol. 101, p. 016807, Jul 2008.

[58] A. Wójs and J. J. Quinn, "Landau level mixing in the $\nu = 5/2$ fractional quantum Hall state," *Phys. Rev. B*, vol. 74, p. 235319, Dec 2006.

[59] R. H. Morf, N. d'Ambrumenil, and S. Das Sarma, "Excitation gaps in fractional quantum Hall states: An exact diagonalization study," *Phys. Rev. B*, vol. 66, p. 075408, Aug 2002.

[60] R. H. Morf, "Transition from quantum Hall to compressible states in the second Landau level: New light on the $\nu = 5/2$ enigma," *Phys. Rev. Lett.*, vol. 80, pp. 1505–1508, Feb 1998.

[61] M. Storni, R. H. Morf, and S. Das Sarma, "Fractional quantum Hall state at $\nu = \frac{5}{2}$ and the Moore-Read Pfaffian," *Phys. Rev. Lett.*, vol. 104, p. 076803, Feb 2010.

[62] J. Nuebler, V. Umansky, R. Morf, M. Heiblum, K. von Klitzing, and J. Smet, "Density dependence of the $\nu = \frac{5}{2}$ energy gap: Experiment and theory," *Phys. Rev. B*, vol. 81, p. 035316, Jan 2010.

[63] A. E. Feiguin, E. Rezayi, C. Nayak, and S. Das Sarma, "Density matrix renormalization group study of incompressible fractional quantum Hall states," *Phys. Rev. Lett.*, vol. 100, p. 166803, Apr 2008.

[64] S. D. Sarma, M. Friedman, and C. Nayak, "Topological quantum computation," *Physics Today*, p. 32, July 2006.

[65] S. Das Sarma, M. Freedman, and C. Nayak, "Topologically protected qubits from a possible non-Abelian fractional quantum Hall state," *Phys. Rev. Lett.*, vol. 94, p. 166802, Apr 2005.

[66] C. Nayak, S. H. Simon, A. Stern, M. Freedman, and S. Das Sarma, "Non-Abelian anyons and topological quantum computation," *Rev. Mod. Phys.*, vol. 80, pp. 1083–1159, Sep 2008.

[67] G. P. Collins, "Computing with quantum knots," *Scientific American*, p. 41, Apr. 2006.

[68] A. Stern, "Anyons and the quantum Hall effect – A pedagogical review," *Annals of Physics*, vol. 323, pp. 204 – 249, 2008.

[69] N. R. Cooper and A. Stern, "Observable bulk signatures of non-Abelian quantum Hall states," *Phys. Rev. Lett.*, vol. 102, p. 176807, Apr 2009.

[70] K. Yang and B. I. Halperin, "Thermopower as a possible probe of non-Abelian quasiparticle statistics in fractional quantum Hall liquids," *Phys. Rev. B*, vol. 79, p. 115317, Mar 2009.

[71] A. Stern and B. I. Halperin, "Proposed experiments to probe the non-Abelian $\nu = 5/2$ quantum Hall state," *Phys. Rev. Lett.*, vol. 96, p. 016802, Jan 2006.

[72] P. Bonderson, A. Kitaev, and K. Shtengel, "Detecting non-Abelian statistics in the $\nu = 5/2$ fractional quantum Hall state," *Phys. Rev. Lett.*, vol. 96, p. 016803, Jan 2006.

[73] A. Stern, B. Rosenow, R. Ilan, and B. I. Halperin, "Interference, Coulomb blockade, and the identification of non-Abelian quantum Hall states," *Phys. Rev. B*, vol. 82, p. 085321, Aug 2010.

[74] B. Rosenow and B. I. Halperin, "Influence of interactions on flux and back-gate period of quantum Hall interferometers," *Phys. Rev. Lett.*, vol. 98, p. 106801, Mar 2007.

[75] R. L. Willett, L. N. Pfeiffer, and K. W. West, "Alternation and interchange of e/4 and e/2 period interference oscillations consistent with filling factor 5/2 non-Abelian quasiparticles," *Phys. Rev. B*, vol. 82, p. 205301, Nov 2010.

[76] I. P. Radu, J. B. Miller, C. M. Marcus, M. A. Kastner, L. N. Pfeiffer, and K. W. West, "Quasi-particle properties from tunneling in the $\nu = 5/2$ fractional quantum Hall state," *Science*, vol. 320, pp. 899–902, 2008.

[77] J. B. Miller, I. P. Radu, D. M. Zumbuhl, E. M. Levenson-Falk, M. A. Kastner, C. M. Marcus, L. N. Pfeiffer, and K. W. West, "Fractional quantum Hall effect in a quantum point contact at filling fraction 5/2," *Nat. Phys.*, vol. 3, pp. 561–565, Aug. 2007.

[78] V. Venkatachalam, A. Yacoby, L. Pfeiffer, and K. West, "Local charge of the $\nu = 5/2$ fractional quantum Hall state," *Nature*, vol. 469, pp. 185–188, Jan. 2011.

[79] M. Dolev, M. Heiblum, V. Umansky, A. Stern, and D. Mahalu, "Observation of a quarter of an electron charge at the $\nu = 5/2$ quantum Hall state," *Nature*, vol. 452, pp. 829–834, Apr. 2008.

[80] J. Eisenstein, R. Willett, H. Stormer, L. Pfeiffer, and K. West, "Activation energies for the even-denominator fractional quantum Hall effect," *Surface Science*, vol. 229, pp. 31 – 33, 1990.

[81] J. P. Eisenstein, R. Willett, H. L. Stormer, D. C. Tsui, A. C. Gossard, and J. H. English, "Collapse of the even-denominator fractional quantum Hall effect in tilted fields," *Phys. Rev. Lett.*, vol. 61, p. 997, Aug 1988.

[82] F. D. M. Haldane and E. H. Rezayi, "Spin-singlet wave function for the half-integral quantum Hall effect," *Phys. Rev. Lett.*, vol. 60, pp. 956–959, Mar 1988.

[83] A. E. Feiguin, E. Rezayi, K. Yang, C. Nayak, and S. Das Sarma, "Spin polarization of the $\nu = 5/2$ quantum Hall state," *Phys. Rev. B*, vol. 79, p. 115322, Mar 2009.

[84] W. Pan, H. L. Stormer, D. C. Tsui, L. N. Pfeiffer, K. W. Baldwin, and K. W. West, "Experimental evidence for a spin-polarized ground state in the $\nu = 5/2$ fractional quantum Hall effect," *Solid State Communications*, vol. 119, no. 12, pp. 641 – 645, 2001.

[85] C. Zhang, T. Knuuttila, Y. Dai, R. R. Du, L. N. Pfeiffer, and K. W. West, "$\nu = 5/2$ fractional quantum Hall effect at 10 T: Implications for the Pfaffian state," *Phys. Rev. Lett.*, vol. 104, p. 166801, Apr 2010.

[86] M. Stern, P. Plochocka, V. Umansky, D. K. Maude, M. Potemski, and I. Bar-Joseph, "Optical probing of the spin polarization of the $\nu = 5/2$ quantum Hall state," *Phys. Rev. Lett.*, vol. 105, p. 096801, Aug 2010.

[87] C. L. Yang, M. A. Zudov, T. A. Knuuttila, R. R. Du, L. N. Pfeiffer, and K. W. West, "Observation of microwave-induced zero-conductance state in Corbino rings of a two-dimensional electron system," *Phys. Rev. Lett.*, vol. 91, p. 096803, Aug 2003.

[88] R. L. Willett, L. N. Pfeiffer, and K. W. West, "Evidence for current-flow anomalies in the irradiated 2D electron system at small magnetic fields," *Phys. Rev. Lett.*, vol. 93, p. 026804, Jul 2004.

[89] S. A. Studenikin, A. S. Sachrajda, J. A. Gupta, Z. R. Wasilewski, O. M. Fedorych, M. Byszewski, D. K. Maude, M. Potemski, M. Hilke, K. W. West, and L. N. Pfeiffer, "Frequency quenching of microwave-induced resistance oscillations in a high-mobility two-dimensional electron gas," *Phys. Rev. B*, vol. 76, p. 165321, Oct 2007.

[90] J. H. Smet, B. Gorshunov, C. Jiang, L. Pfeiffer, K. West, V. Umansky, M. Dressel, R. Meisels, F. Kuchar, and K. von Klitzing, "Circular-polarization-dependent study of the microwave photoconductivity in a two-dimensional electron system," *Phys. Rev. Lett.*, vol. 95, p. 116804, Sep 2005.

[91] A. Wirthmann, B. D. McCombe, D. Heitmann, S. Holland, K.-J. Friedland, and C.-M. Hu, "Far-infrared-induced magnetoresistance oscillations in GaAs/Al_xGa_{1-x}As based two-dimensional electron systems," *Phys. Rev. B*, vol. 76, p. 195315, 2007.

[92] S. A. Studenikin, M. Potemski, A. Sachrajda, M. Hilke, L. N. Pfeiffer, and K. W. West, "Microwave-induced resistance oscillations on a high-mobility two-dimensional electron gas: Exact waveform, absorption/reflection and temperature damping," *Phys. Rev. B*, vol. 71, p. 245313, Jun 2005.

[93] A. T. Hatke, M. A. Zudov, L. N. Pfeiffer, and K. W. West, "Temperature dependence of microwave photoresistance in 2D electron systems," *Phys. Rev. Lett.*, vol. 102, p. 066804, Feb 2009.

[94] M. A. Zudov, "Period and phase of microwave-induced resistance oscillations and zero-resistance states in two-dimensional electron systems," *Phys. Rev. B*, vol. 69, p. 041304, Jan 2004.

[95] R. G. Mani, "Radiation-induced oscillatory magnetoresistance in a tilted magnetic field in GaAs/$Al_xGa_{1-x}As$ devices," *Phys. Rev. B*, vol. 72, p. 075327, Aug 2005.

[96] C. L. Yang, R. R. Du, L. N. Pfeiffer, and K. W. West, "Influence of a parallel magnetic field on the microwave photoconductivity in a high-mobility two-dimensional electron system," *Phys. Rev. B*, vol. 74, p. 045315, Jul 2006.

[97] S. Wiedmann, N. Mamani, G. Gusev, O. Raichev, A. Bakarov, and J. Portal, "Integer and fractional microwave induced resistance oscillations in a 2D system with moderate mobility," *Physica E: Low-dimensional Systems and Nanostructures*, vol. 42, pp. 1078 – 1080, 2010.

[98] S. I. Dorozhkin, J. H. Smet, V. Umansky, and K. von Klitzing, "Microwave photoresponse in the two-dimensional electron system caused by intra-Landau-level transitions," *Phys. Rev. B*, vol. 71, p. 201306, May 2005.

[99] J. P. Kotthaus, G. Abstreiter, and J. F. Koch, "Subharmonic structure of cyclotron resonance an inversion layer on Si," *Solid State Communications*, vol. 15, pp. 517 – 519, 1974.

[100] O. M. Fedorych, M. Potemski, S. A. Studenikin, J. A. Gupta, Z. R. Wasilewski, and I. A. Dmitriev, "Quantum oscillations in the microwave magnetoabsorption of a two-dimensional electron gas," *Phys. Rev. B*, vol. 81, p. 201302, May 2010.

[101] S. I. Dorozhkin, I. V. Pechenezhskiy, L. N. Pfeiffer, K. W. West, V. Umansky, K. von Klitzing, and J. H. Smet, "Photocurrent and photovoltage oscillations in the two-dimensional electron system: Enhancement and suppression of built-in electric fields," *Phys. Rev. Lett.*, vol. 102, p. 036602, Jan 2009.

[102] I. Dmitriev, S. Dorozhkin, and A. Mirlin, "Photogalvanic effects originating from the violation of the Einstein relation in a 2D electron gas in high Landau levels," *Physica E: Low-dimensional Systems and Nanostructures*, vol. 42, pp. 1159 – 1162, 2010.

[103] C. L. Yang, J. Zhang, R. R. Du, J. A. Simmons, and J. L. Reno, "Zener tunneling between Landau orbits in a high-mobility two-dimensional electron gas," *Phys. Rev. Lett.*, vol. 89, p. 076801, Jul 2002.

[104] W. Zhang, M. A. Zudov, L. N. Pfeiffer, and K. W. West, "Resistance oscillations in two-dimensional electron systems induced by both ac and dc fields," *Phys. Rev. Lett.*, vol. 98, p. 106804, Mar 2007.

[105] W. Zhang, M. Zudov, L. Pfeiffer, and K. West, "Effect of dc excitation on microwave-induced resistance oscillations and zero-resistance states in a two-dimensional electron system," *Physica E: Low-dimensional Systems and Nanostructures*, vol. 40, pp. 982 – 985, 2008.

[106] A. T. Hatke, H.-S. Chiang, M. A. Zudov, L. N. Pfeiffer, and K. W. West, "Nonlinear magnetotransport in microwave-illuminated two-dimensional electron systems," *Phys. Rev. B*, vol. 77, p. 201304, May 2008.

[107] A. C. Durst, S. Sachdev, N. Read, and S. M. Girvin, "Radiation-Induced magnetoresistance oscillations in a 2D electron gas," *Phys. Rev. Lett.*, vol. 91, p. 086803, Aug 2003.

[108] X. L. Lei and S. Y. Liu, "Radiation-induced magnetoresistance oscillation in a two-dimensional electron gas in Faraday geometry," *Phys. Rev. Lett.*, vol. 91, p. 226805, Nov 2003.

[109] V. Ryzhii and R. Suris, "Nonlinear effects in microwave photoconductivity of two-dimensional electron systems," *Journal of Physics: Condensed Matter*, vol. 15, no. 40, p. 6855, 2003.

[110] M. G. Vavilov and I. L. Aleiner, "Magnetotransport in a two-dimensional electron gas at large filling factors," *Phys. Rev. B*, vol. 69, p. 035303, Jan 2004.

[111] I. A. Dmitriev, A. D. Mirlin, and D. G. Polyakov, "Cyclotron-resonance harmonics in the ac response of a 2D electron gas with smooth disorder," *Phys. Rev. Lett.*, vol. 91, p. 226802, Nov 2003.

[112] S. Dorozhkin, "Giant magnetoresistance oscillations caused by cyclotron resonance harmonics," *JETP Letters*, vol. 77, pp. 577–581, 2003.

[113] I. A. Dmitriev, M. G. Vavilov, I. L. Aleiner, A. D. Mirlin, and D. G. Polyakov, "Theory of microwave-induced oscillations in the magnetoconductivity of a two-dimensional electron gas," *Phys. Rev. B*, vol. 71, p. 115316, Mar 2005.

[114] I. A. Dmitriev, M. Khodas, A. D. Mirlin, D. G. Polyakov, and M. G. Vavilov, "Mechanisms of the microwave photoconductivity in two-dimensional

electron systems with mixed disorder," *Phys. Rev. B*, vol. 80, p. 165327, Oct 2009.

[115] I. A. Dmitriev, S. I. Dorozhkin, and A. D. Mirlin, "Theory of microwave-induced photocurrent and photovoltage magneto-oscillations in a spatially nonuniform two-dimensional electron gas," *Phys. Rev. B*, vol. 80, p. 125418, Sep 2009.

[116] V. Ryzhii and V. Vyurkov, "Absolute negative conductivity in two-dimensional electron systems associated with acoustic scattering stimulated by microwave radiation," *Phys. Rev. B*, vol. 68, p. 165406, Oct 2003.

[117] V. Ryzhii, "Microwave photoconductivity in two-dimensional electron systems due to photon-assisted interaction of electrons with leaky interface phonons," *Phys. Rev. B*, vol. 68, p. 193402, Nov 2003.

[118] O. E. Raichev, "Microwave-induced magnetoresistance of two-dimensional electrons interacting with acoustic phonons," *Phys. Rev. B*, vol. 81, p. 165319, Apr 2010.

[119] A. A. Koulakov and M. E. Raikh, "Classical model for the negative dc conductivity of ac-driven two-dimensional electrons near the cyclotron resonance," *Phys. Rev. B*, vol. 68, p. 115324, Sep 2003.

[120] J. Iñarrea and G. Platero, "Theoretical approach to microwave-radiation-induced zero-resistance states in 2D electron systems," *Phys. Rev. Lett.*, vol. 94, p. 016806, Jan 2005.

[121] A. D. Chepelianskii and D. L. Shepelyansky, "Microwave stabilization of edge transport and zero-resistance states," *Phys. Rev. B*, vol. 80, p. 241308, Dec 2009.

[122] A. D. Chepelianskii, A. S. Pikovsky, and D. L. Shepelyansky, "Synchronization, zero-resistance states and rotating Wigner crystal.," *European Physical Journal B – Condensed Matter*, vol. 60, no. 2, pp. 225 – 229, 2007.

[123] R. G. Mani, C. Gerl, S. Schmult, W. Wegscheider, and V. Umansky, "Nonlinear growth in the amplitude of radiation-induced magnetoresistance oscillations," *Phys. Rev. B*, vol. 81, p. 125320, Mar 2010.

[124] A. V. Andreev, I. L. Aleiner, and A. J. Millis, "Dynamical symmetry breaking as the origin of the zero-dc-resistance state in an ac-driven system," *Phys. Rev. Lett.*, vol. 91, p. 056803, Aug 2003.

[125] A. Auerbach, I. Finkler, B. I. Halperin, and A. Yacoby, "Steady states of a microwave-irradiated quantum-Hall gas," *Phys. Rev. Lett.*, vol. 94, p. 196801, May 2005.

[126] I. G. Finkler and B. I. Halperin, "Microwave-induced zero-resistance states are not necessarily static," *Phys. Rev. B*, vol. 79, p. 085315, Feb 2009.

[127] S. I. Dorozhkin, L. Pfeiffer, K. West, K. von Klitzing, and J. H. Smet, "Random telegraph photosignals in a microwave-exposed two-dimensional electron system," *Nat. Phys.*, vol. 7, pp. 336–341, Apr. 2011.

[128] A. Bykov, A. Bakarov, D. Islamov, and A. Toropov, "Giant magnetoresistance oscillations induced by microwave radiation and a zero-resistance state in a 2D electron system with a moderate mobility," *JETP Letters*, vol. 84, pp. 391–394, 2006.

[129] M. O. Goerbig, P. Lederer, and C. M. Smith, "Competition between quantum-liquid and electron-solid phases in intermediate Landau levels," *Phys. Rev. B*, vol. 69, p. 115327, Mar 2004.

[130] H. C. Choi, W. Kang, S. Das Sarma, L. N. Pfeiffer, and K. W. West, "Activation gaps of fractional quantum Hall effect in the second Landau level," *Phys. Rev. B*, vol. 77, p. 081301, Feb 2008.

[131] C. R. Dean, B. A. Piot, P. Hayden, S. Das Sarma, G. Gervais, L. N. Pfeiffer, and K. W. West, "Intrinsic gap of the $\nu = 5/2$ fractional quantum Hall state," *Phys. Rev. Lett.*, vol. 100, p. 146803, Apr 2008.

[132] U. Meirav and E. B. Foxman, "Single-electron phenomena in semiconductors," *Semiconductor Science and Technology*, vol. 11, no. 3, p. 255, 1996.

[133] J. Weis, *Single electron devices and quantum dots.* unpublished, 2006.

[134] B. Buonomo, M. G. Castellano, R. Leoni, F. Mattioli, G. Torrioli, P. Carelli, F. Chiarello, and C. Cosmelli, "Aluminum single-electron transistors studied at 0.3 K in different transport regimes," *Journal of Applied Physics*, vol. 89, no. 11, pp. 6545–6547, 2001.

[135] T. Yamamoto, Y. Nakamura, Y. A. Pashkin, O. Astafiev, and J. S. Tsai, "Parity effect in superconducting aluminum single electron transistors with spatial gap profile controlled by film thickness," *Applied Physics Letters*, vol. 88, no. 21, p. 212509, 2006.

[136] J. P. Eisenstein, L. N. Pfeiffer, and K. W. West, "Compressibility of the two-dimensional electron gas: Measurements of the zero-field exchange energy and fractional quantum Hall gap," *Phys. Rev. B*, vol. 50, pp. 1760–1778, Jul 1994.

[137] S. Ilani, A. Yacoby, D. Mahalu, and H. Shtrikman, "Unexpected behavior of the local compressibility near the $B = 0$ metal-insulator transition," *Phys. Rev. Lett.*, vol. 84, pp. 3133–3136, Apr 2000.

[138] J. P. Eisenstein, L. N. Pfeiffer, and K. W. West, "Negative compressibility of interacting two-dimensional electron and quasiparticle gases," *Phys. Rev. Lett.*, vol. 68, pp. 674–677, Feb 1992.

[139] T. N. Theis, "Plasmons in inversion layers," *Surface Science*, vol. 98, no. 1-3, pp. 515 – 532, 1980.

[140] D. Heitmann, "Two-dimensional plasmons in homogeneous and laterally microstructured space charge layers," *Surface Science*, vol. 170, no. 1-2, pp. 332 – 345, 1986.

[141] O. Kirichek, ed., *Edge excitations of low-dimensional charged systems*, vol. 236. Nova science publischers, Inc, 2001.

[142] S. A. Mikhailov, "Microwave-induced magnetotransport phenomena in two-dimensional electron systems: Importance of electrodynamic effects," *Phys. Rev. B*, vol. 70, p. 165311, Oct 2004.

Acknowledgments

- Prof. Dr. Klaus von Klitzing for the possibility to work in his group. The combination of an excellent scientific working atmosphere (and equipment) and large freedom in the daily work is stimulating and rewarding.

- Dr. Jurgen Smet for the best supervision in the world. His expertise, and willingness to share it, from how to connect a cable to the subtleties of the quantum Hall effect, is immense. I learned a lot more than physics.

- Prof. Dr. David Wharam (Universität Tübingen) for inspiring lectures when I was a student in Tübingen, which brought me to mesoscopic physics in the first place, and for supervising this thesis.

- Prof. Dr. Amir Yacoby and his team (Harvard University, USA), especially Vivek Venkatachalam, Jonah Waissman and Jens Martin for fabrication of single electron transistors. And for welcoming me in their group during two most inspiring and enjoyable stays at Harvard University.

- Dr. Vladimir Umansky (Weizmann Institute of Science, Israel) for providing all the excellent wafers, a most important ingredient for this work.

- Prof. Dr. Rudolf Morf (Paul Scherrer Institut, Switzerland) for numerical calculation of energy gaps with the special parameters of our specific experiments and for generously answering an experimentalists questions about theoretical aspects of the fractional quantum Hall effect.

- Prof. Dr. Alexander Mirlin and Dr. Ivan Dimitriev (Universität Karlsruhe) for discussions about microwave induced effects in 2D electron systems.

- Our technical staff, Manfred Schmid, Ingo Hagel and Steffen Wahl, for their invaluable support with cryostats, sample holders and helium filling.

- The cleanroom team for excellent facilities and much support in wafer processing.

- All colleagues in our group for a great working atmosphere.
- Christine − for your love, patience and sharing the fascination for liquid helium and these tiny electrons (especially the red ones).
- Friends and family for both support of − and distraction from work.
- Special thanks to Stefan Nandzik, Christoph Zürn and Marc-Oliver Pahl for help with the concept and implementation of databases, also related to work at the MPI.